VOLUME 3
December 25, 1997

ADDENDA TO DOE/ID-10503, -10504

T. G. Theofanous, et al.

Advanced
Reactor
Severe
Accident
Program

Department of Energy

9801260085 980120
PDR ADOCK 05200003
A PDR

VOLUME 3
December 25, 1997

ADDENDA TO DOE/ID-10503, -10504

T.G. Theofanous et al.

Center for Risk Studies and Safety
Departments of Chemical and Mechanical Engineering
University of California, Santa Barbara
Santa Barbara, CA 93106

Prepared for the
U. S. Department of Energy
Idaho Operations Office
Under ANL Subcontract No. 23572401

CONTENTS

[[ADDENDUM 2 TO SECTION 2.2.3 of DOE/ID-10504]]

QUEOS HOT TEST SIMULATIONS WITH PM-ALPHA.L

In Addendum 1 we presented comparisons with selected QUEOS cold runs, and a limited comparison (only the qualitative features of the mixing zone) for a hot run (Q10). Meanwhile, additional hot QUEOS tests became available (Meyer 1997[1]), while, as became clear in the recent CSNI FCI meeting in Japan, no other serious attempts at interpretation of these tests exists. For this effort, therefore, we chose, to begin with, one of the runs analyzed in our original report (Q17), and one of the newly available runs (Q34). In what became a much deeper analysis now, we came to appreciate many subtleties regarding the role of the 5-m long vent pipe in the experiment as well as in the calculations. Also, we found major differences between the quoted values of losses in this pipe and what is apparent during the actual experiments (see Figure 1). Having learned of these effects, and some additional significant experimental issues (as discussed below), we decided that comparison with just these two runs is quite adequate for our present purposes. Moreover, these two runs span quite well the QUEOS conditions; that is, (see Table 1) particle cloud dimensions, particle diameter, material/density, and magnitude of the interactions as characterized by the peak pressurization. In Q17, the resulting steaming was rather intense (as far as QUEOS experiments go) and of short duration, while Q34 produced a much milder and longer duration steam puff.

Table 1. Conditions of QUEOS Tests Q17 and Q34

Run #	Mater.	d_p [mm]	ρ [kg/ℓ]	T_{max} [°C]	Mass [kg]	θ_f [%]	Cloud ($\phi \times L$) [cmxcm]	ΔP [bar]
Q17	Mo	4.2	10	1850	10	19.6	~20 x 20	0.3
Q34	ZrO_2	10	6	1650	14	23.8	10 x 125	0.1

The computations were carried out with the 2D, PM-ALPHA.L code, on a 5 x 5 cm cylindrical grid that preserves the QUEOS test vessel cross-sectional area. The vent opening, rather than at the side, was put on the top of the test section. The modelling of the vent line itself, and the interpretation (timing relative to pressure in the vessel) of the

---

[1] L. Meyer, "QUEOS, a Simulation-Experiment of the Premixing Phase of a Steam Explosion with Hot Spheres in Water. Results of the second test series,"Forschungszentrum Karlsruhe, Technik und Umwelt, Interner Bericht 32.31.02, July, 1997.

flow measurement in it (2.5 m from the inlet) took a rather non-trivial effort, as described in the following four steps.

Step 1. *Determine and understand the roles of the freeboard volume, and vent line loss factor, under constant steam production rate and gain experience with PM-ALPHA in representing these.*

Neglecting temperature changes we have an exact solution for the pressure history, given by

$$0.5\frac{t}{\tau} = -\sqrt{\frac{P-P_o}{\frac{\xi\rho_e}{2}(v_i\frac{A_i}{A_e})^2}} - \ell n\left(1-\sqrt{\frac{P-P_o}{\frac{\xi\rho_e}{2}(v_i\frac{A_i}{A_e})^2}}\right) \tag{1}$$

where the time constant τ is given by

$$\tau = \frac{\xi}{2}\frac{\rho_e V Q_i}{P_e A_e^2} \tag{2}$$

and Q_i is the inlet flow rate, V is the freeboard volume, P_e and ρ_e are pressure and density at the exit (atmospheric), A_e is the exit flow area, and ξ is the total pipe loss factor. From these we can obtain the flow rate transient by

$$Q_e = A_e\sqrt{\frac{2(P-P_e)}{\rho_0\xi}} \tag{3}$$

Results for a loss factor of 10 (see below for this choice), and two inlet flow rates, 0.5 and 1 m^3/s, corresponding to the peak flows in the two tests considered here, are shown in Figure 2. These figures also show PM-ALPHA.L results, with a vent pipe of 50 cm, and the loss factor distributed over three computational cells within the pipe. In Figure 3, we can see the effect of the pipe length in introducing a time delay in the flow transient measured, as in the QUEOS tests, 2.5 m away from the inlet.

Step 2. *Understand the loss factor behavior in the experiments.*

The measured pressure-flow trajectories in the two experiments considered here are shown in Figure 4. In the experiment, the major losses were upstream of the flow meter, and the frictional losses of the pipe itself were negligible, so the $\Delta P - \dot{Q}_e$ data pairs shown in Figure 4 should be consistent (save for some time delay to be discussed shortly) to an overall loss factor representation such that

$$\Delta P = \frac{1}{2}\xi\rho_e\frac{\dot{Q}_e^2}{A_e^2} \tag{4}$$

where subscript e signifies exit (atmospheric) conditions. Constant ξ lines of this equation are also shown in Figure 4, and indicate that the portions of the experimental trajectories that correspond to the rising flow rate portions of the transients are characterized by loss factors between 8 and 10. These are significantly higher than the 4.54 value quoted by the experimenters (obtained from separate, steady, air-blow experiments). More importantly, the decaying portions show still higher and non-reproducible values, with Q17 reaching $\xi \sim 20$!

We can imagine two potential reasons for this apparent increase in pipe losses during the experiments: water entrainment and carryover into the pipe, and condensation on pipe walls and flow straightener, upstream of the flow meter. Water entrainment is certainly evident within the field of view of the video frames (the upper region of the freeboard space and entrance to the vent pipe are not shown), and is consistent with the much greater buildup of losses in Q17 that had considerably more intense interaction. Condensation is possibly a significant cause also, because even if initially at saturation temperature, pipe walls and internals would become subcooled as pressure increased through the transient. In fact, there are indications (i.e., thermocouple reading inside vent pipe) that there might have been subcooling even to begin with. Precise estimates must account for mixing with the air initially present (unknown quantity) and its effect in impeding condensation. Recognizing that these details are quite peripheral to our subject, and that with the limited information available on them further elaboration would quickly be met by limited returns, further consideration of the QUEOS experiments requires us to

(a) assume that condensation did not play an important role, and

(b) deduce an empirical representation of the pipe loss factor variation with time, and use it as a boundary condition in our PM-ALPHA.L simulations.

In fact, even item (b) is not as straightforward as one might first imagine as discussed next.

Step 3. *Extract, empirically, the loss factors in the experiments.*

As noted in Step 1, due to the large (2.5 m) distance of the flow meter from the interaction vessel, the pressure and flow readings are not "physically synchronous," as required in the definition of an overall loss factor. This would not create a problem if we were to simulate, in PM-ALPHA.L, the whole vent line, and take the flow predicted at the position of the flow meter for comparison. However, given the "problems" with the loss factor variation with time noted above this would be unnecessarily cumbersome. Rather, we introduce a constant delay, t^*, in the flow measurement to extract the loss factor, by

$$\xi = \frac{2(P(t) - P_e)A_e^2}{\rho_e \dot{Q}_e^2(t + t^*)} \tag{5}$$

Plotted in this fashion, for different values of t^*, the experiment $\Delta P - \dot{Q}_e$ data for Q17 and Q34 are shown in Figures 5 and 6 respectively. As expected, we find that a delay of ~6 to 15 ms is necessary to obtain a reasonable behavior in the loss factor in the early portion of the transient. This is consistent with the entrainment explanation—it would be expected to build with time, leaving a nearly constant value of the loss factor initially, and with a value closer to the 4.54 value measured with air under steady conditions. Note that this does not include the entrance losses (from the vessel to the pipe) present in the experiment. Also note that at the very start of the transient (the first ~20 ms) both flows and pressures are very low, so that measurement errors propagate to a rather large uncertainty in the loss factor. Some small amounts of condensation may further add to this early uncertainty, but both effects would be expected to diminish (in relative terms) with time as flow and pressure build up, leaving entrainment the dominant factor. The appropriateness of time delay so deduced is also confirmed by the illustration in Figure 7. As a conclusion of this analysis we will use the time-wise variation of the pipe loss factors, for these two runs, as shown in Figure 8.

Step 4. *Demonstrate the consistent reproduction of the experimental pressure and flow rate transients with PM- ALPHA.L and determine the* inlet *flow transients needed to produce these behaviors.*

The needed flow rate transients are obtained by the simple model, that led to Eqs. (1)–(3), applied in differential time increments together with the loss factors shown in Figure 8. The results are shown in Figures 9 and 10. Remarkable is the vapor generation "pulse" needed to produce the measured flow and pressure transients in Q17. For the milder Q34, the difference between input and measured flows is much less, but still significant. Finally, using these input flow transients in PM-ALPHA.L, together with the loss factors in Figure 8, we could reproduce, consistently, the measured pressure and flow transients, as shown in Figures 11 and 12 respectively. It should be noted that the slightly smaller (10 cm vs 10.8 cm) pipe diameter in PM-ALPHA.L, imposed by the 5 cm node size selected for discretization, was taken into account; scaling by a factor of 0.735 is needed.

We are now prepared to address the interactions themselves, but several additional experimental issues require prior attention.

(a) **Initial, spurious, flow.** As shown in Figure 12, there is a nearly steady steam flow of ~100 ℓ/s prior to the contact of particles with water, occuring at ~0.5 s. This flow appears to initiate rather suddenly, ~100 ms earlier (these first 100 ms not shown in the figure), and it can be seen that it is very reproducible. Simple estimates of the heating and expansion of the steam/air mixture in the freeboard volume, or the radiative boiling at the pool surface (actually seen in the videos), indicate that neither is of sufficient magnitude to provide an explanation. Another possibility is that this flow is due to the highly superheated steam and Argon, trapped in the intermediate vessel, and vented together with the cloud. Unfortunately, this cannot be evaluated, because the pressure was apparently vented prior to opening the doors, but the data are not shown to a sufficient resolution for this special purpose. The experimenters did not discuss this flow, and most importantly, we cannot know whether it persists during the interaction itself. Thus, we cannot do much about this now, except to keep in mind this "additional" flow as we look at the comparison of PM-ALPHA predictions with the experimental data (especially for Q34).

(b) **Initial particle temperature.** For Q34, the value quoted is 1527, while the pyrometer trace shows 1650 °C. We have used the latter value.

(c) **Time origin.** For Q34, time origin is shifted back by 20 ms from the quoted 500 ms. This is suggested by the video images and the pyrometer reading, and is explained by the higher particle exit velocity due to the gravitational head of the longer (than in Q17) bed in the intermediate vessel. This shift applies to both the pressure and flow traces and is distinct from the 20 ms delay of the flow trace relative to the pressure discussed above. For Q17, on the other hand, we take the time zero shifted by +15 ms. This is based on the pyrometer trace where the first particles (at 1200 °C) reach the water at 0.475 s (forerunners from the video images), whereas the 1850 °C bulk reaches the surface at 0.53 s, or 30 ms after the time 0.5 s taken as zero in the experimental traces. Since the whole cloud enters the water within ~50 ms, such corrections are essential.

(d) **Undefined surface conditions of the Mo particles.** The Molybdenum particles were coated with Rhenium, which appears to have reacted (black smoke was seen in Q17) and came off the particles, which, in turn, could oxidize. Thus the emissivity could be time-dependent, starting from low values and building up to ~1. We have taken a value of 0.7 throughout. For Q34, using ZrO_2 particles, the emissivity is more reliably expected to be ~1, and this value was used in the calculations.

The principal phenomenological uncertainty in computing such interactions (low but non-negligible subcooling) is in determining the partition of the thermal energy transferred from the fuel into vaporization and sensible heat absorbed in the liquid. For this we use the option of the code that evaluates the liquid-side convective heat transfer on the basis of a turbulence model, as given by Eq. (3.60) of Appendix A in DOE/ID-10504. The assumptions that have gone into this model are that the characteristic velocity scale is equal to the turbulence intensity, and that the characteristic (or integral) length scale is the particle diameter. This model appeared to work quite well for single spheres in subcooled film boiling (Liu and Theofanous, 1994) with the "universal" value of the coefficient 0.25 showing in Eq. (3.60). Here as a measure of turbulence intensity we take the particle-fluid relative velocity,[2] and this is taken to persist following the departure of all particles from a fluid volume (i.e., behind the particle cloud). Any variations in turbulence properties, compared to those assumed in the present highly complex particle cloud situation, (most likely overestimated here) would affect the value of this coefficient, hence as a first attempt we will attempt to capture any such variability by applying parametric variations to it (it is called "C" in the figures). As the upper limit we use the 0.25 value, and as the lower one we use zero. Note that this coefficient also controls condensation, and a zero value would completely eliminate this process. Consistent with this treatment the film boiling and radiative heat flows are deposited at the interface (note that below 2000 °C the absorption length in water is less than 1 mm), and partitioned among vapor production and liquid heatup according to Eq. (3.28) of Appendix A in DOE/ID-10504.

Finally, we need to specify the initial or inlet particle cloud dimensions and volume fractions. There are some uncertainties here, too. For Q17, the total volume of the cloud was estimated as 5.11 ℓ and the total mass was 10 kg, which with a material density of 10 kg/ℓ indicates a particle volume fraction (assumed uniform) of 19.6%. The pointed front shape (due to the finite door opening time) seen in the video may not be negligible in such a short (20 cm) cloud, so it was approximated by a leading, 5 cm long by 10 cm in diameter cloud, followed by the main one, 15 cm long and 20 cm in diameter. In Q34, the cloud was much longer (125 cm) and with half the diameter (10 cm) thus this front shape effect was neglected. The total volume of the cloud was 9.8 ℓ with a mass of 14 kg, which with a material density of 6 kg/ℓ yield a uniform volume fraction of 23.8%. These values of the particle volume fractions put both of these runs deeply within the inertia regime (see Addendum 1 to Appendix B). The assumption of uniformity, especially in these long

---

[2] T.G. Theofanous and J. Sullivan, "Turbulence in Two-Phase Dispersed Flows," *J. Fluid Mechanics*, **116**, 1982, 343-362

pours, represents another uncertainty in the specified initial conditions in the experiment, and should be checked, by X-rays for example as was done in MAGICO-2000.

The results of the simulations are shown together with the visual images from the experiments in Figures 13 and 14, for Q17 and Q34 respectively. Projected views (constructed from the computations) allow interesting perspectives, and these are shown together with the cross-sectional views in Figures 15 and 16 respectively. There is excellent agreement with all key features of the two interactions, the computations reflecting very well the important differences between the two runs. In particular, notice that the particle cloud shapes and dimensions are well predicted throughout the interaction (this was also observed in the Q10 results supplied earlier—Addendum 1).

In Q17, the experiment exhibits a front "breakup," and a faster penetration, similar to what had been seen already in MAGICO (Appendix B and Addendum 3 to it). These "instabilities" appear to be peculiar to short, dense clouds, and occur even under cold conditions (Appendix B). While interesting on fundamental grounds, we expect them to play a very limited role in assessing the premixing of steam explosions.

The quantitative comparison of the advancing fronts of the interaction zones for these two runs are shown in Figures 17 and 18. The agreement for Q34 is typical of cases where the front remains coherent. The disagreement observed in Q17 is also typical of cases that develop instabilities, such as short, compact clouds.

The flow and pressure transients are shown in Figures 19 and 20. The full parametrics are shown in Figures 21 and 22. The interpretation of Q17 is quite satisfying. As expected, the turbulence properties appear to have been somewhat overestimated, but both qualitative and quantitative behavior appear to be well captured quite independently of this factor. The interpretation of Q34 is not as good, but this has to be tempered by the question of the spurious flow raised above. Moreover, as such interactions become milder and milder, the scales magnify greatly as in Q34, and they become subject to slight extraneous effects as well as sensitivities. As we remarked in the original report, care must be exercised if such experiments are not to detract from the verification effort. This is not meant as a criticism of the experiment nor the experimenters, after all, they designed and ran the experiments without the help of an interactive analytical effort. Rather, it is only a caution in identifying the pertinent tests, and in interpreting comparisons with predictions.

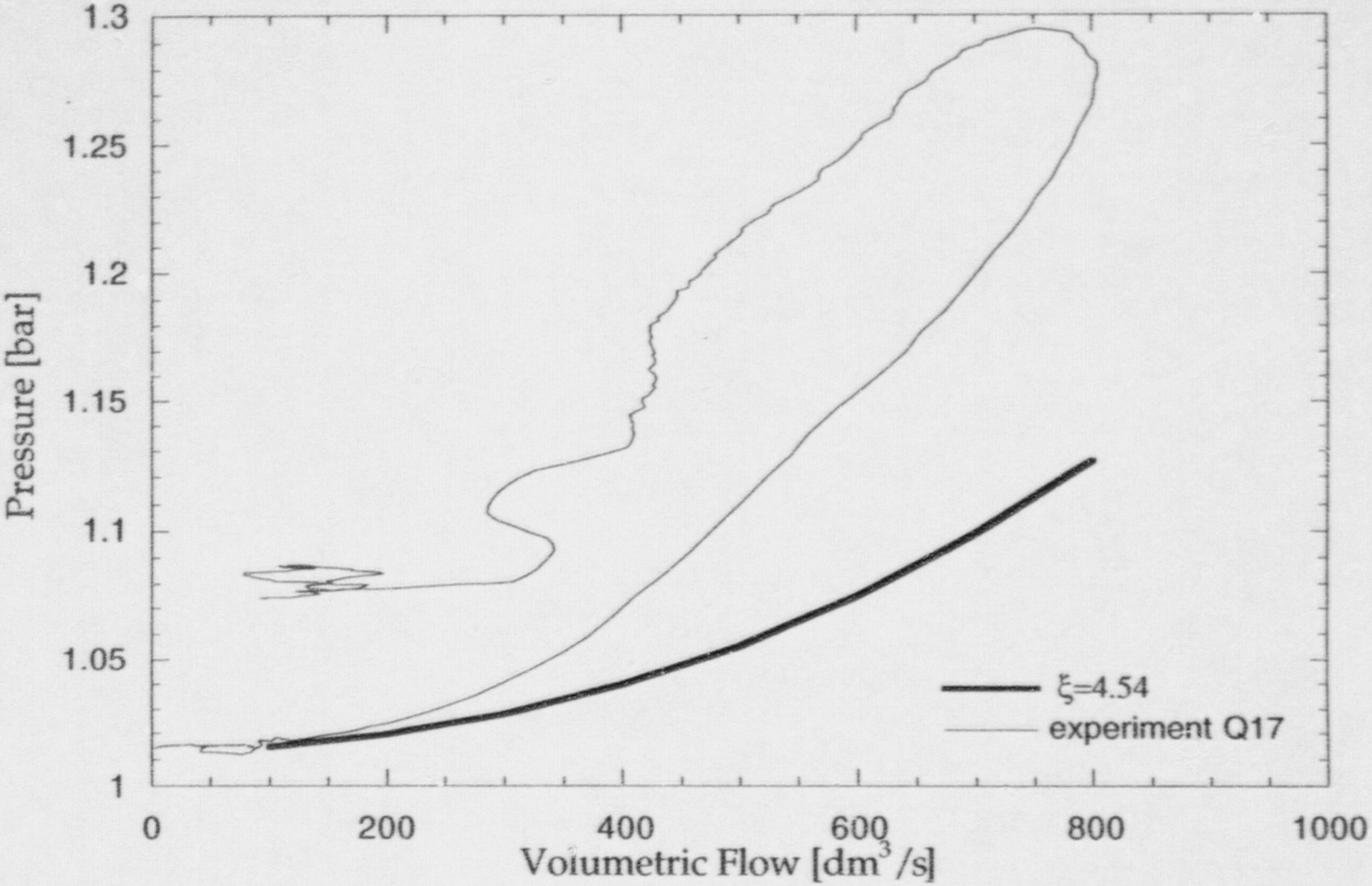

Figure 1. Trajectories of measured flow rates and pressure drops in the QUEOS vent line for run Q17. Also shown is a calculated trajectory based on the loss factor quoted in the QUEOS test report — it was measured in independent experiments using a steady flow of air.

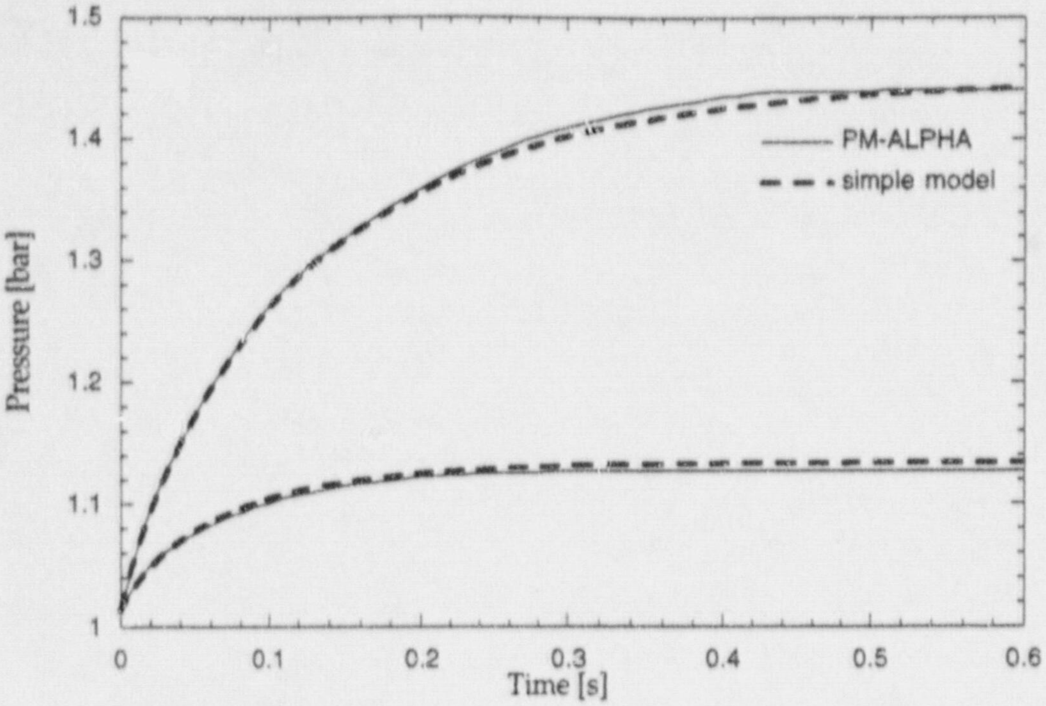

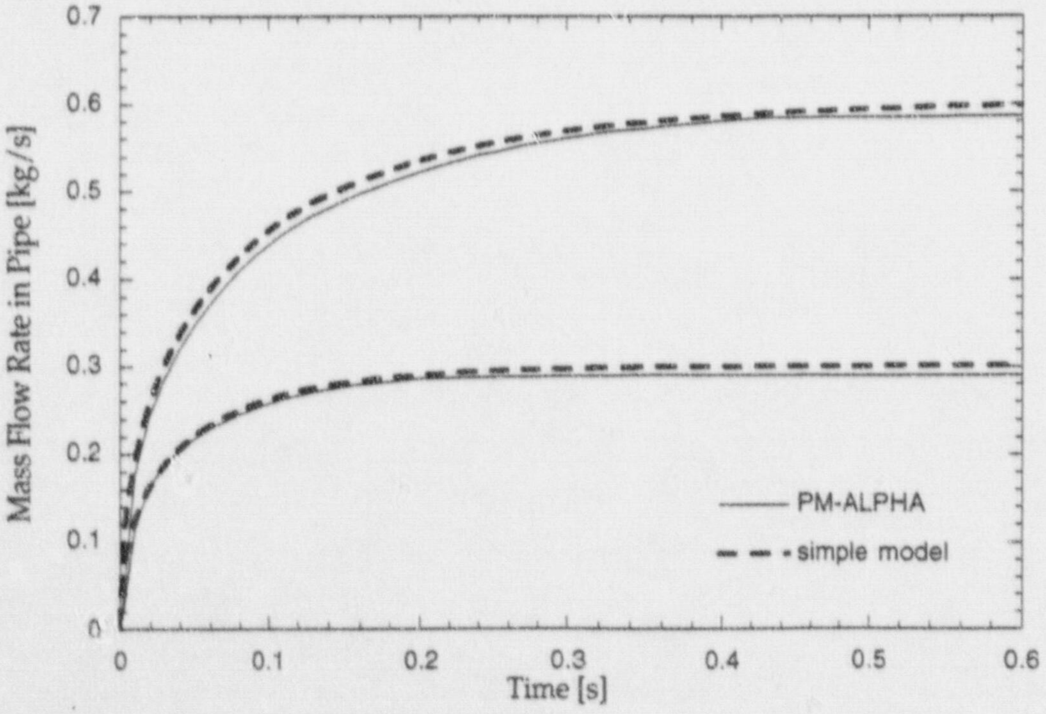

Figure 2. The transient response of the QUEOS vessel-vent line system under a steady steam flow supply of 0.5 and 1 m^3/s.

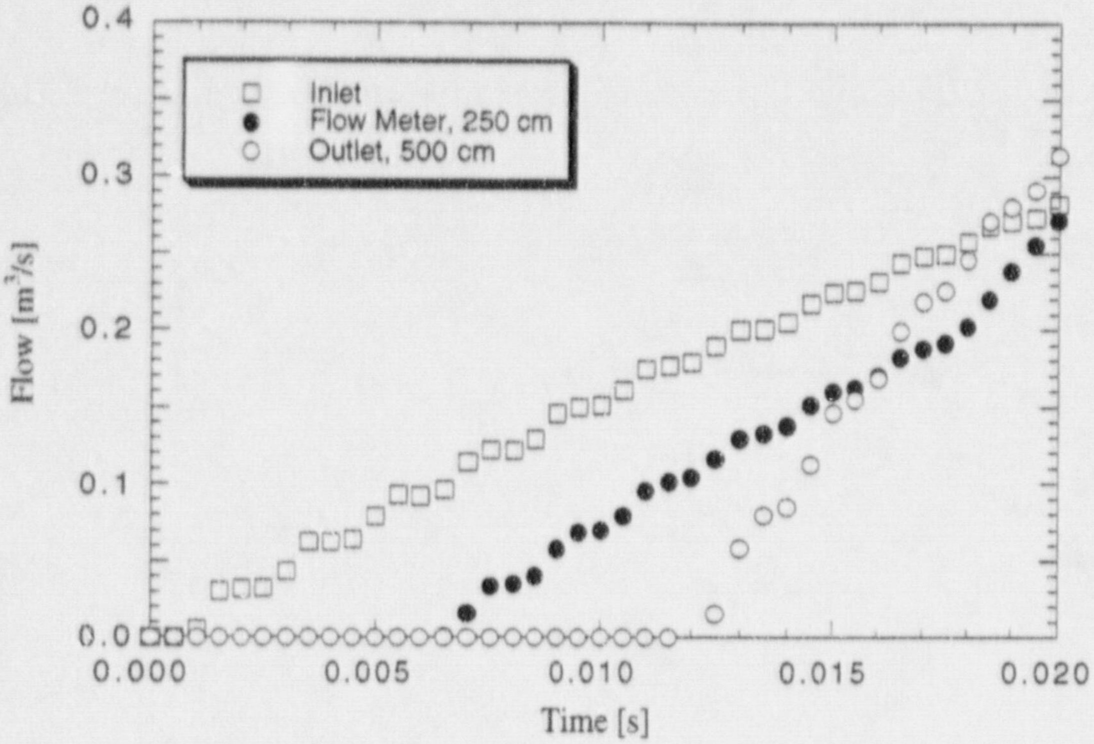

Figure 3. Illustration of the delay time in the pressure-flow signals due to the length of the vent line and location of the flow meter in it.

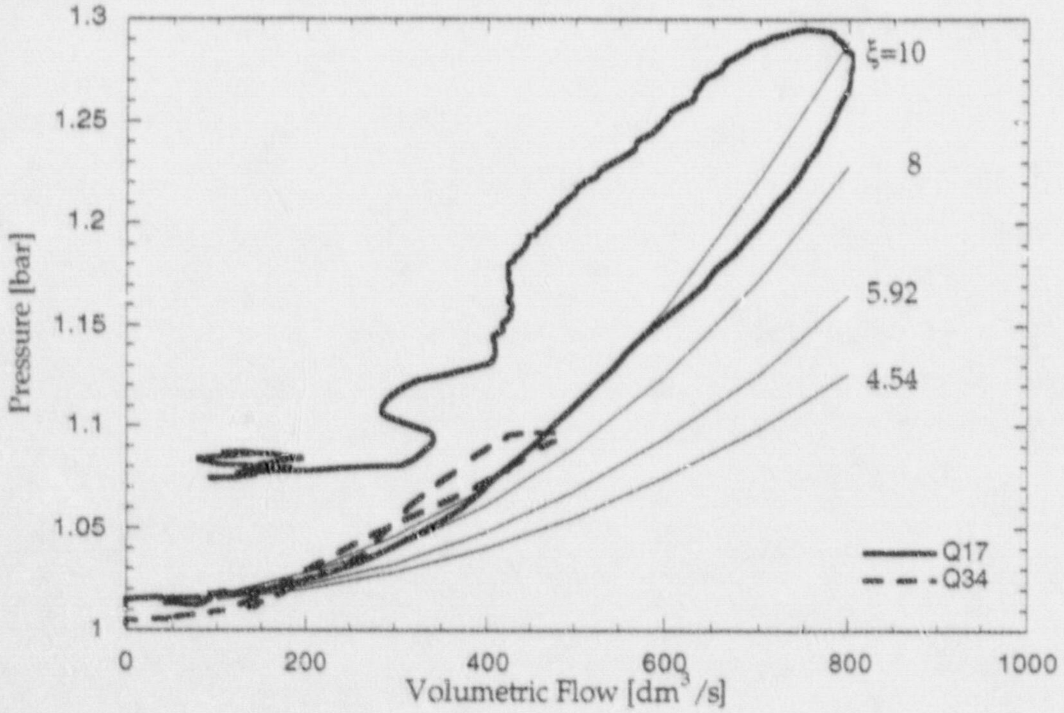

Figure 4. The loss factor behavior of the QUEOS vent line for the two tests considered.

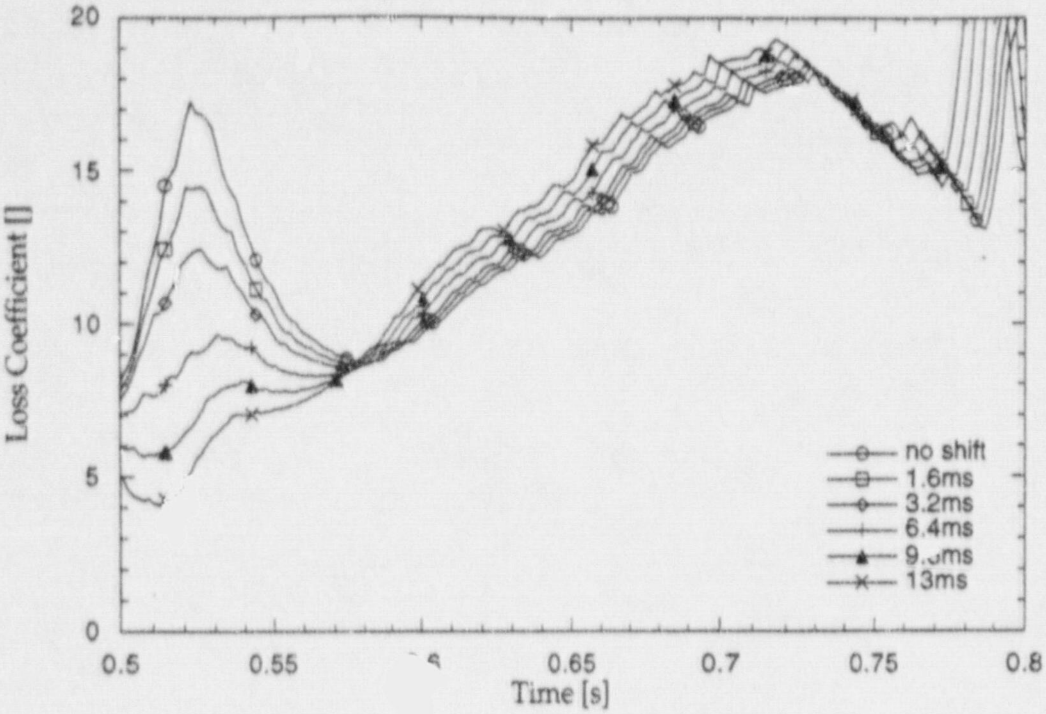

Figure 5. The loss factor behavior in Q17, extracted according to Eq. (5), with the delay time, t^*, as a parameter.

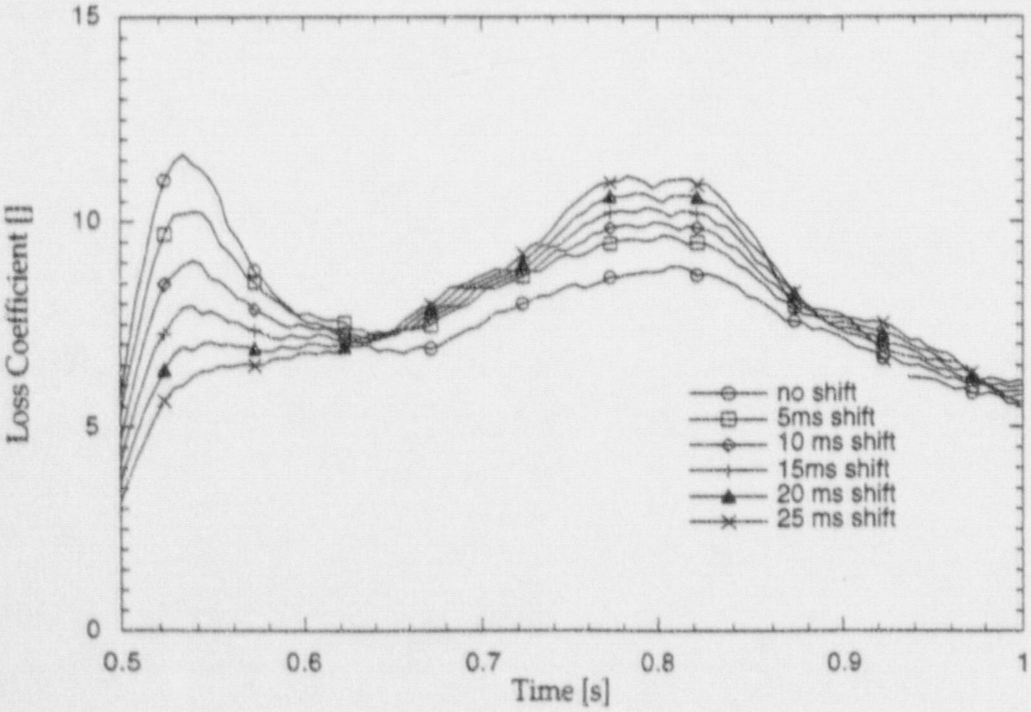

Figure 6. The loss factor behavior in Q34, extracted according to Eq. (5), with the delay time, t^*, as a parameter.

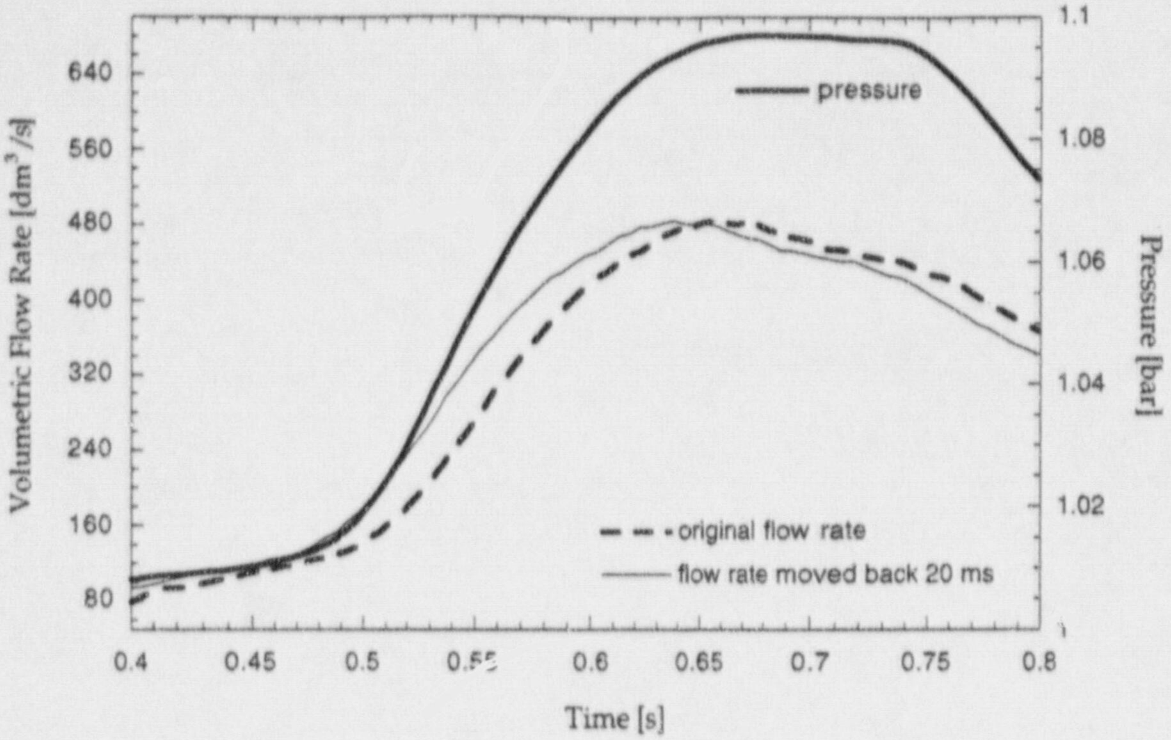

Figure 7. Illustration of the time shift required for "sychronization" of the pressure-flow data in Q34.

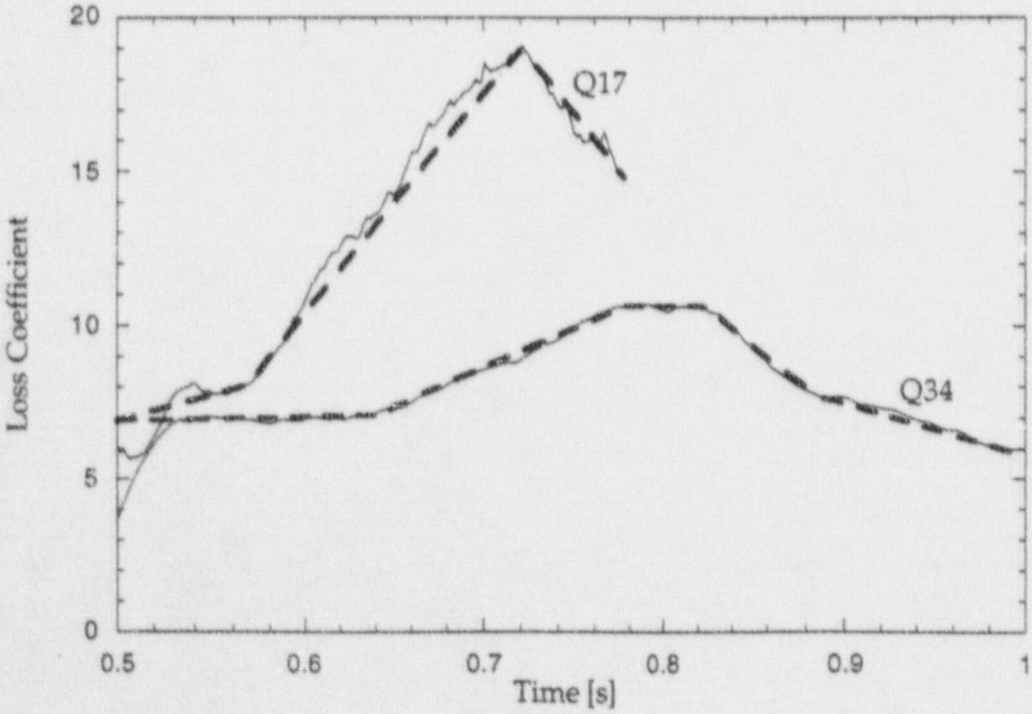

Figure 8. Deduced loss factors (transient behavior) from runs Q17 and Q34.

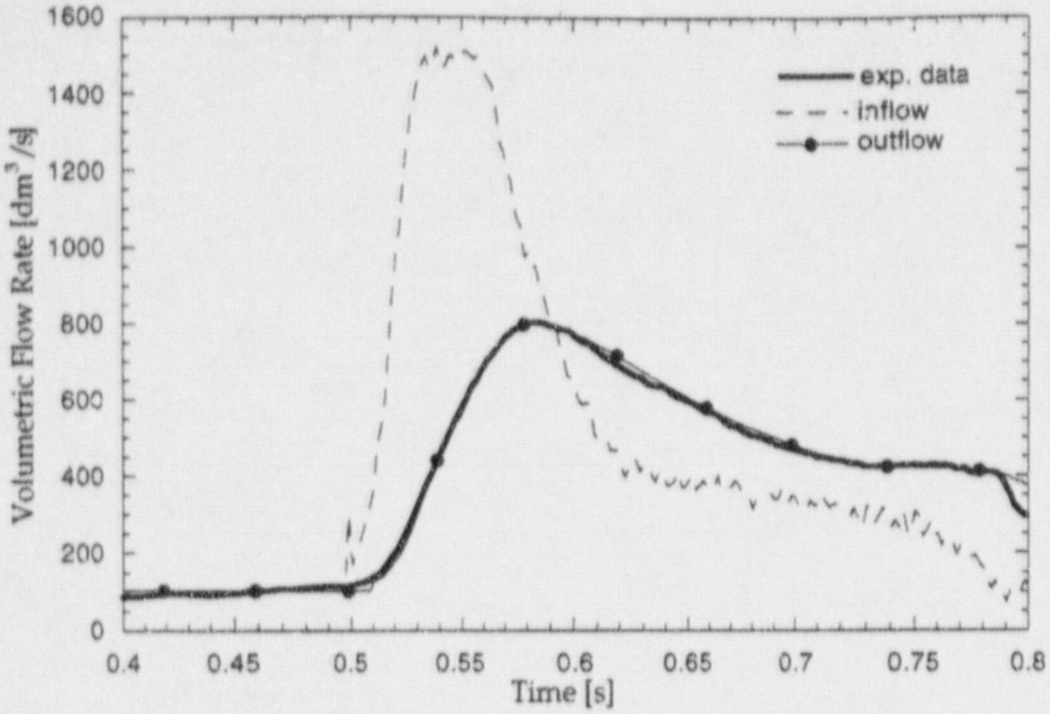

Figure 9. The inlet flow required to produce the measured flow (in the vent line) in Q17.

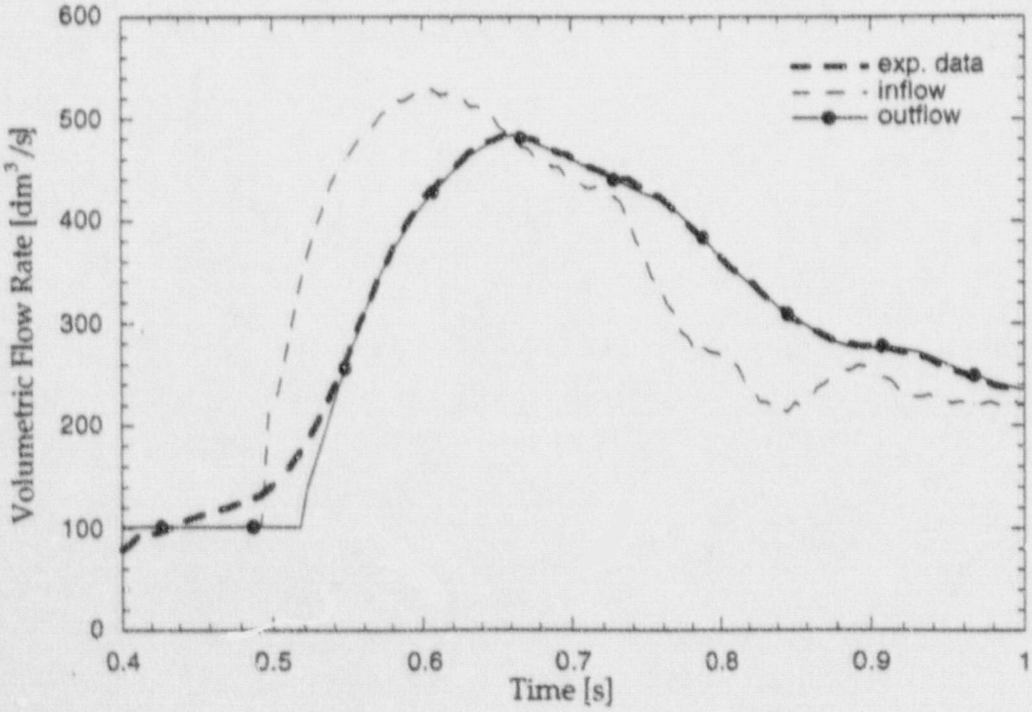

Figure 10. The inlet flow required to produce the measured flow (in the vent line) in Q34.

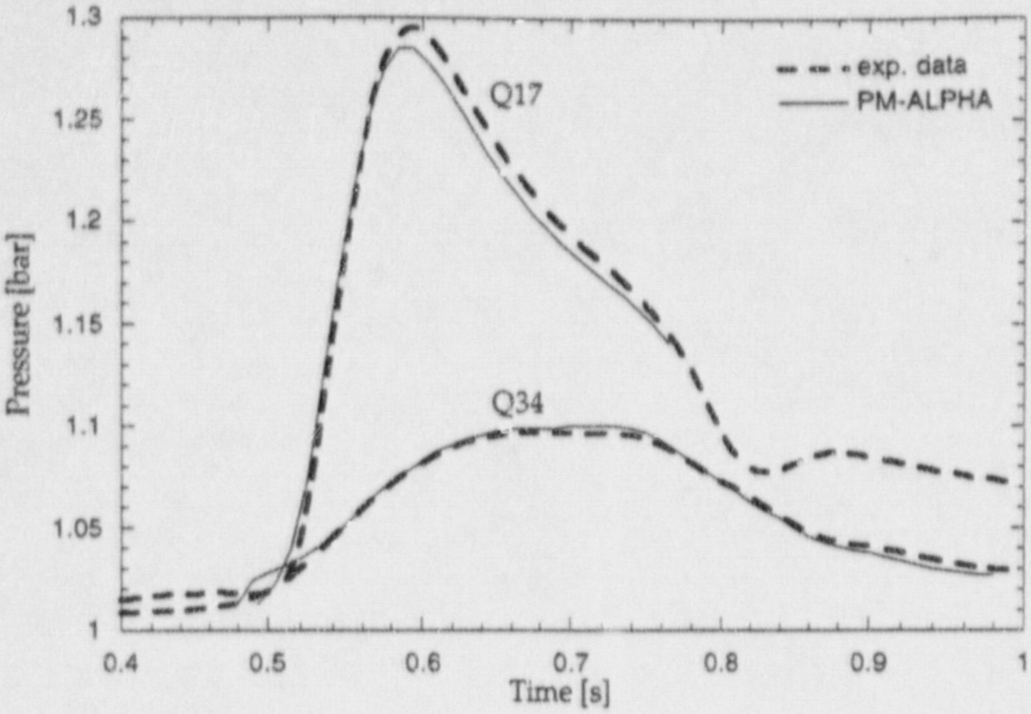

Figure 11. Illustration of the consistent interpretation of measured pressure transients in Q17 and Q34. The code was driven by the inlet flow in Figures 9 and 10, respectively, and the loss factors in Figure 8.

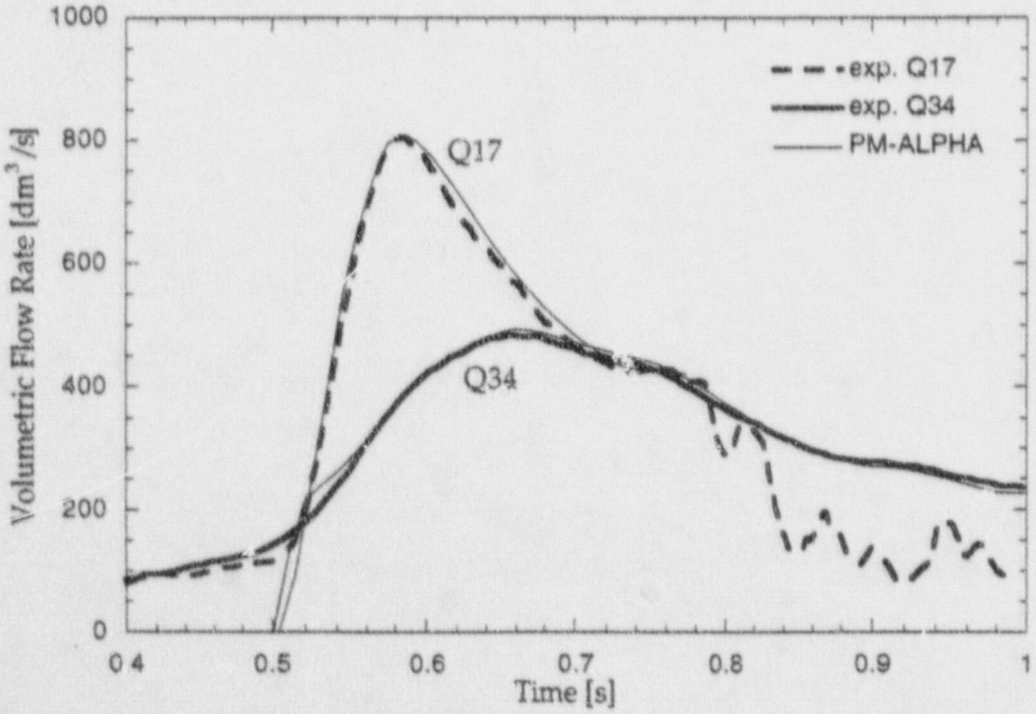

Figure 12. Illustration of the consistent interpretation of measured flow transients in Q17 and Q34. The code was driven by the inlet flow in Figures 9 and 10, respectively and the loss factors in Figure 8.

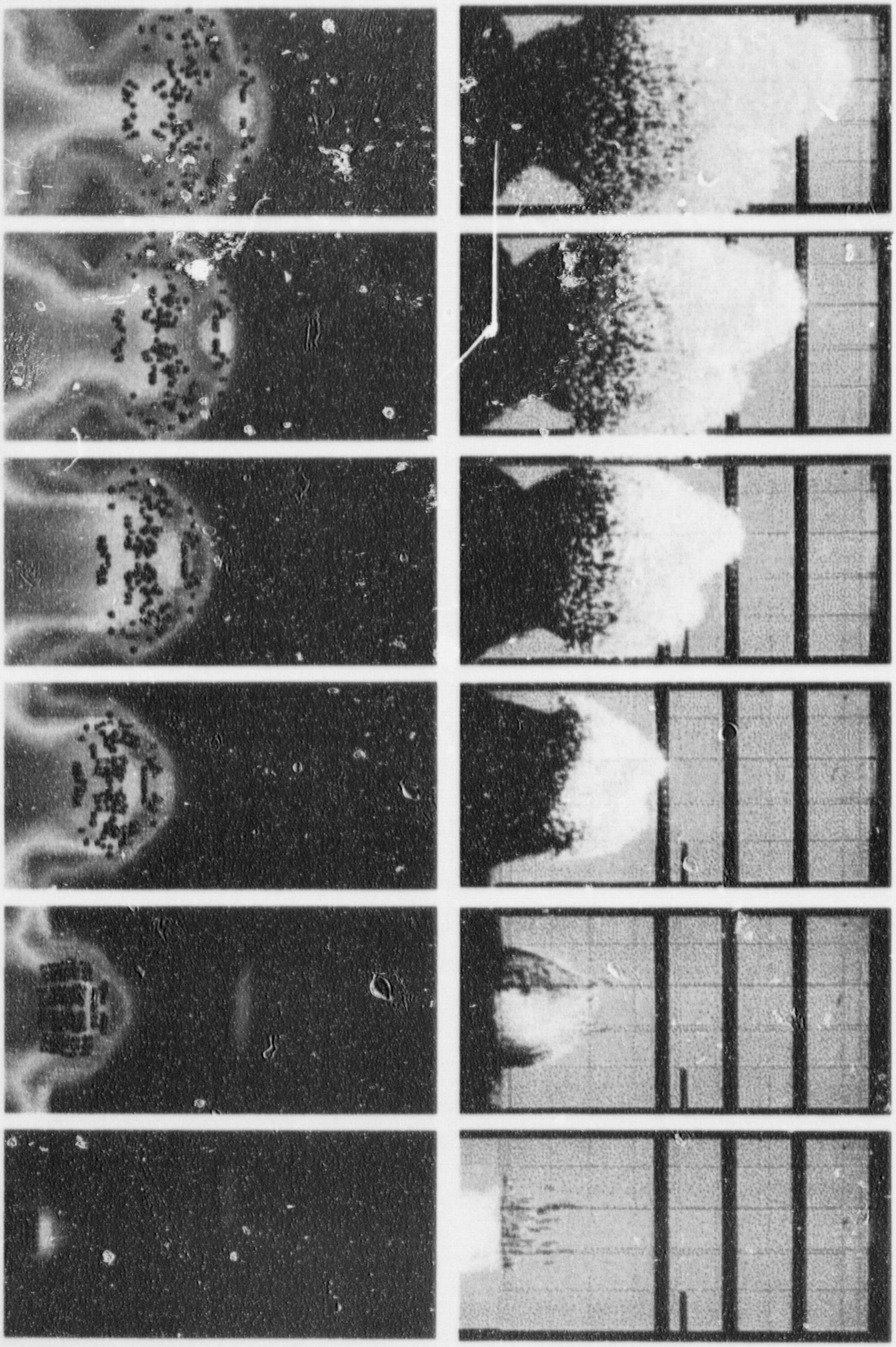

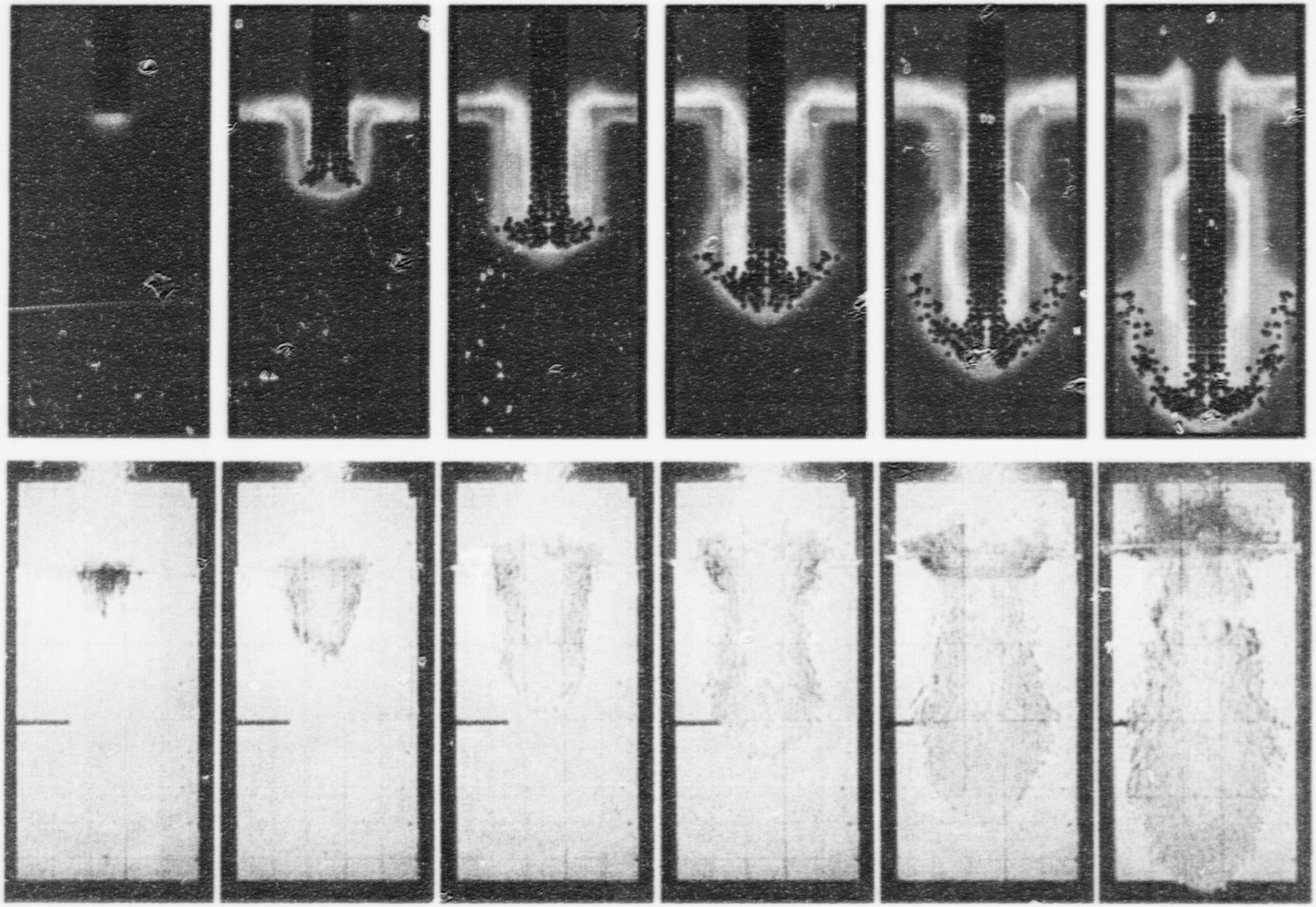

Figure 14. Visual comparison of the PM-ALPHA.L simulation with QUEOS test Q34. Frames are at 50 ms intervals.

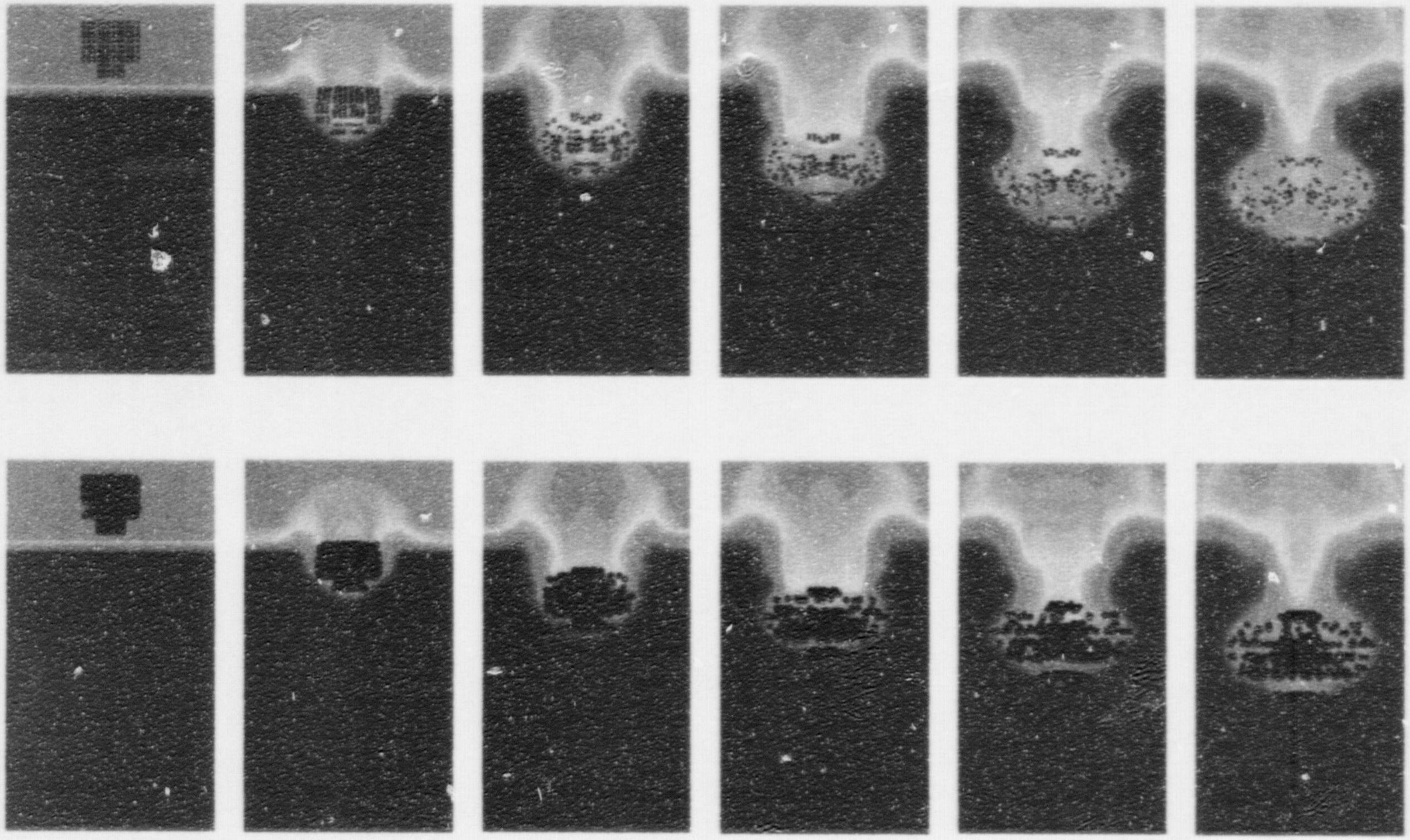

Time = 0.00 s Time = 0.05 s Time = 0.10 s Time = 0.15 s Time = 0.20 s Time = 0.25 s

Figure 15. Projected (as in the movies, particles only) and cross-sectional images from the PM-ALPHA.L simulation of Q17.

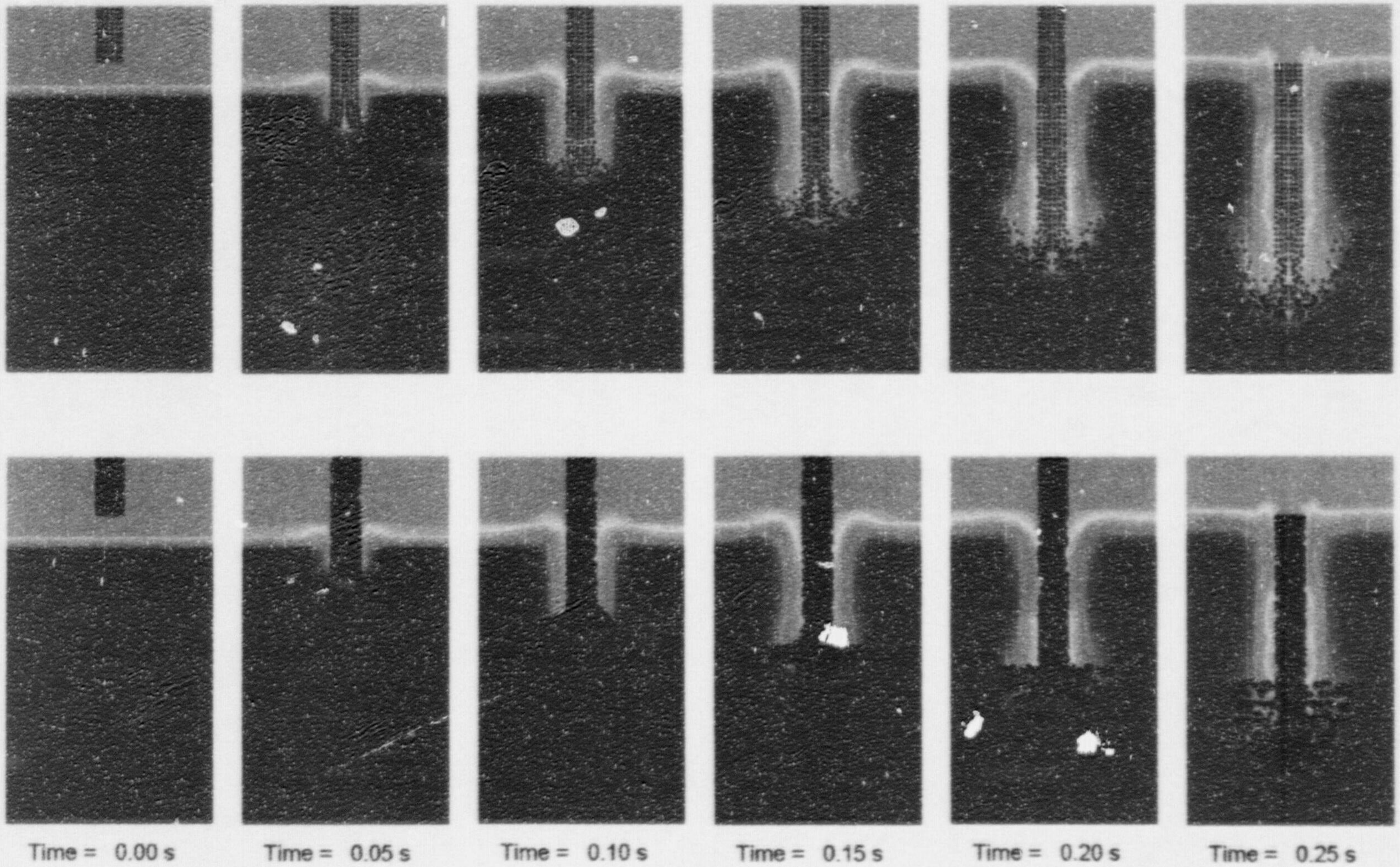

Figure 16. Projected (as in the movies, particles only) and cross-sectional images from the PM-ALPHA.L simulation of Q34.

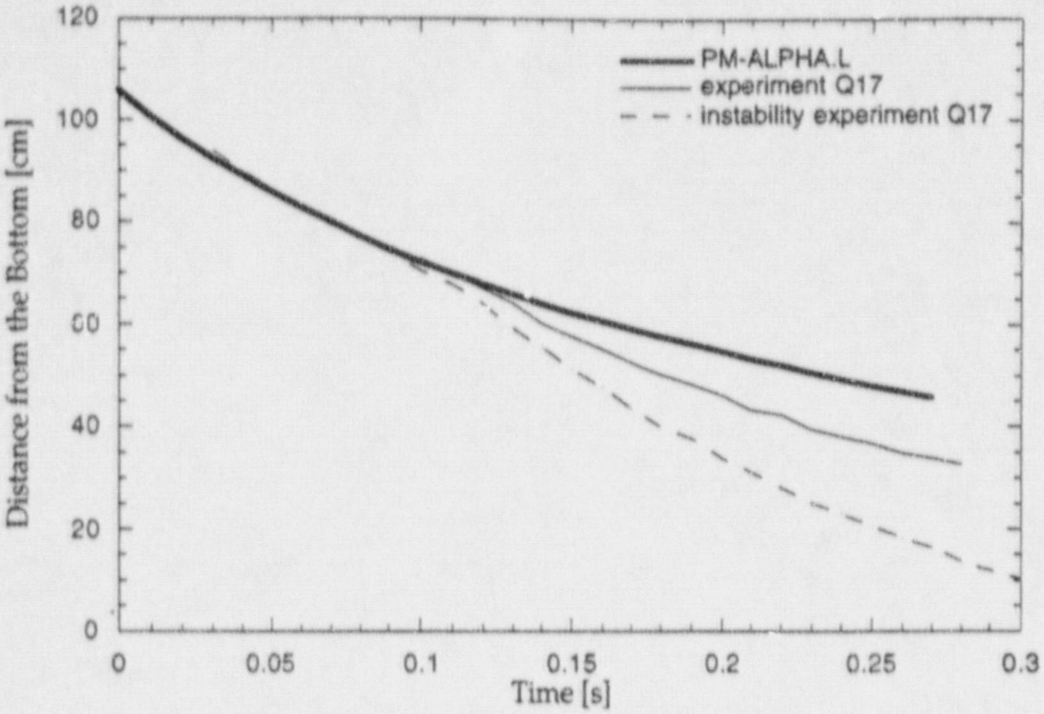

Figure 17. Comparison of the advancing fronts for Q17.

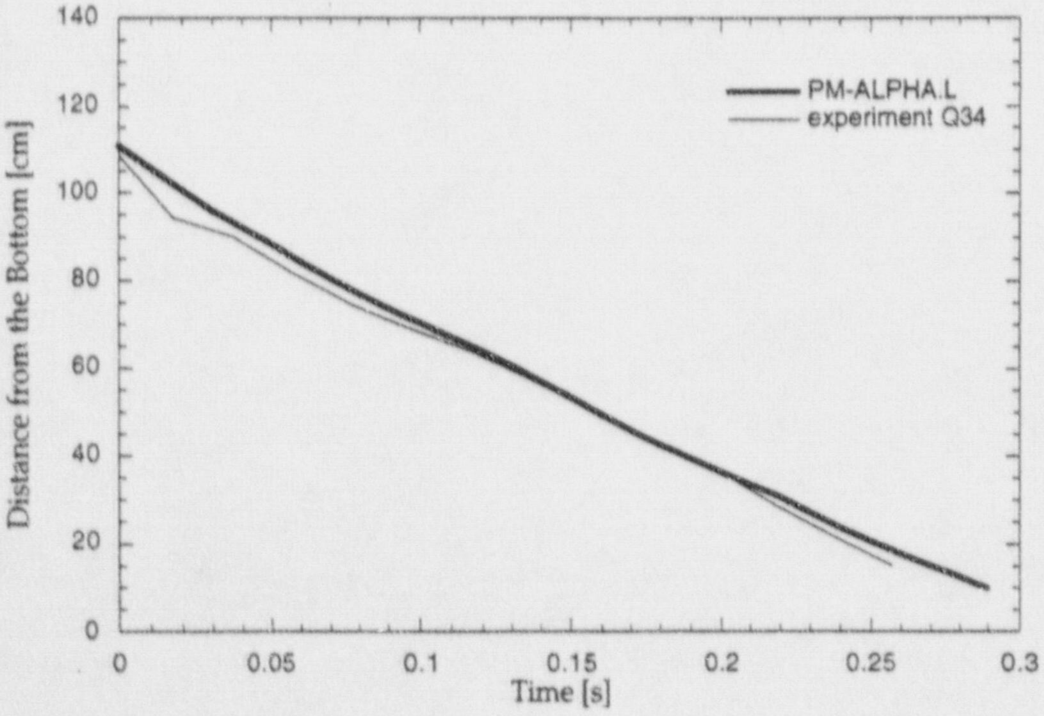

Figure 18. Comparison of the advancing front for Q34.

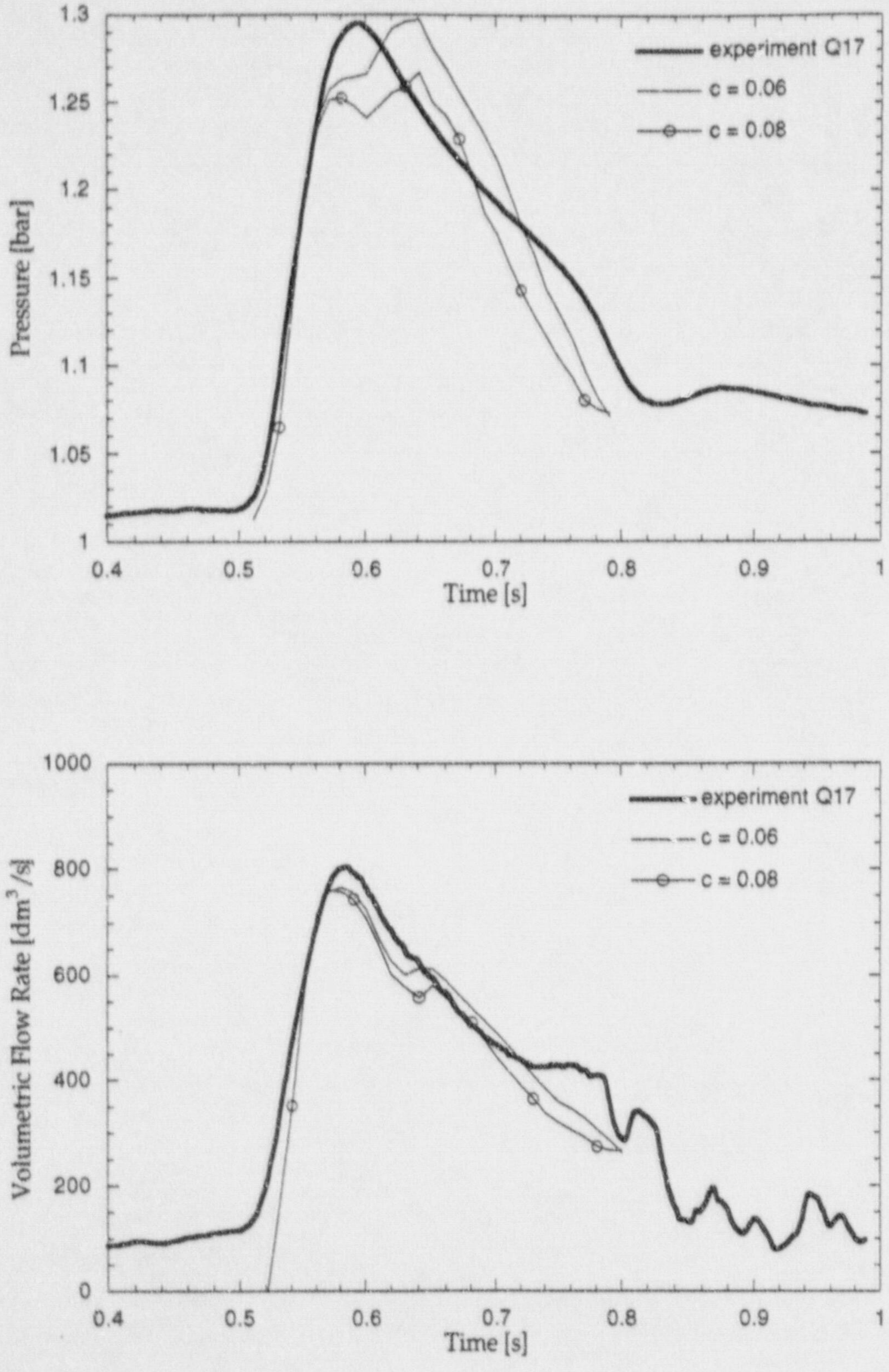

Figure 19. Predicted pressure and flow transients against the experimental data of Q17.

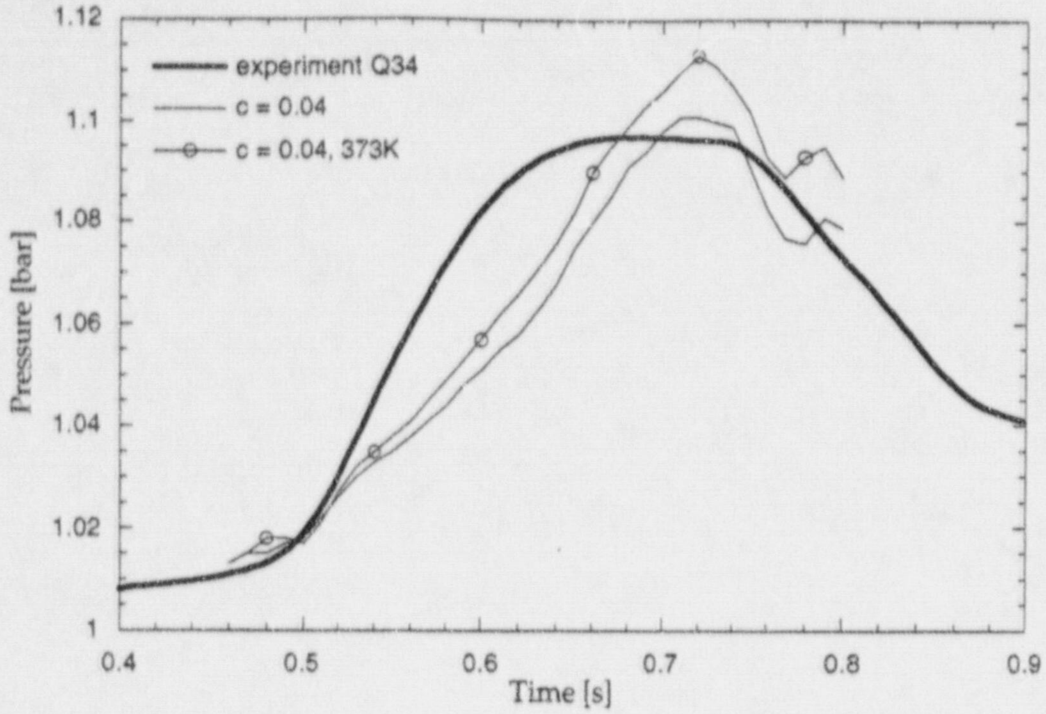

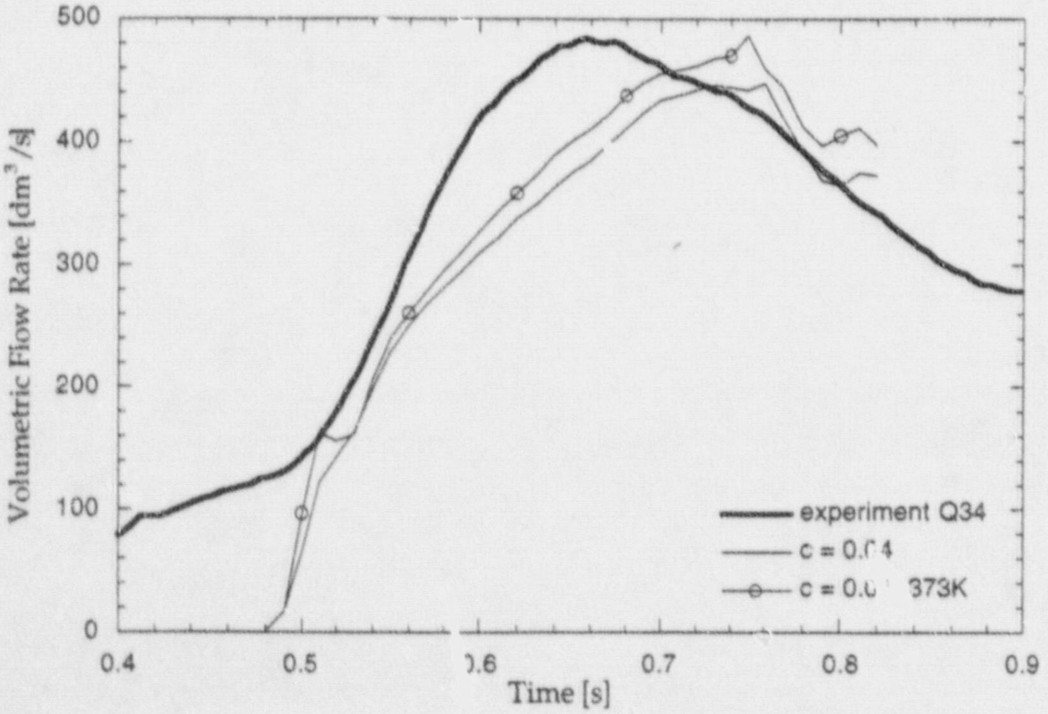

Figure 20. Predicted pressure and flow transients against the experimental data of Q34. In the case marked 373K, the whole pool is set at this temperature rather than the 372.5 quoted for the experiment.

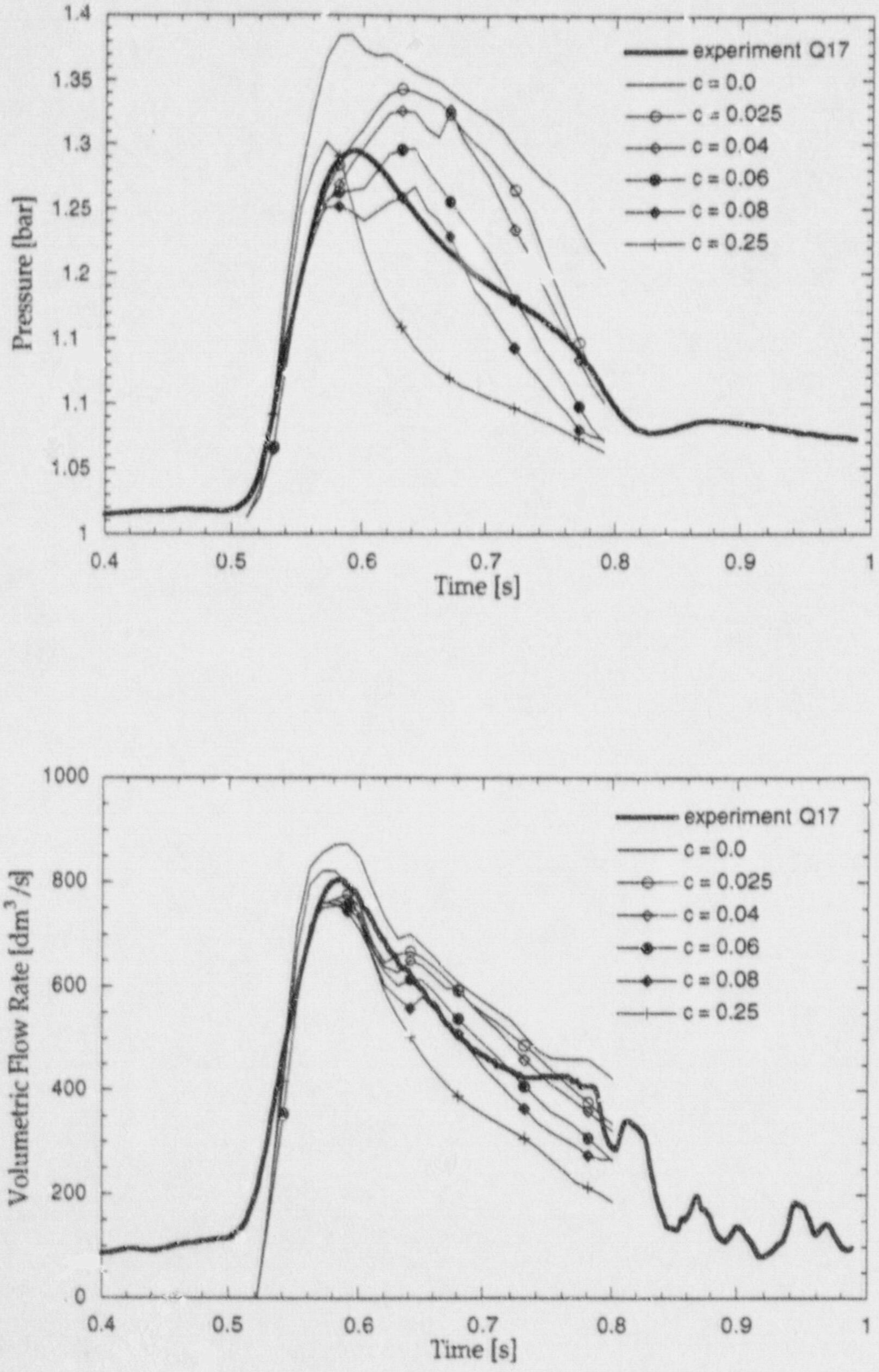

Figure 21. A full parametric on condensation for Q17.

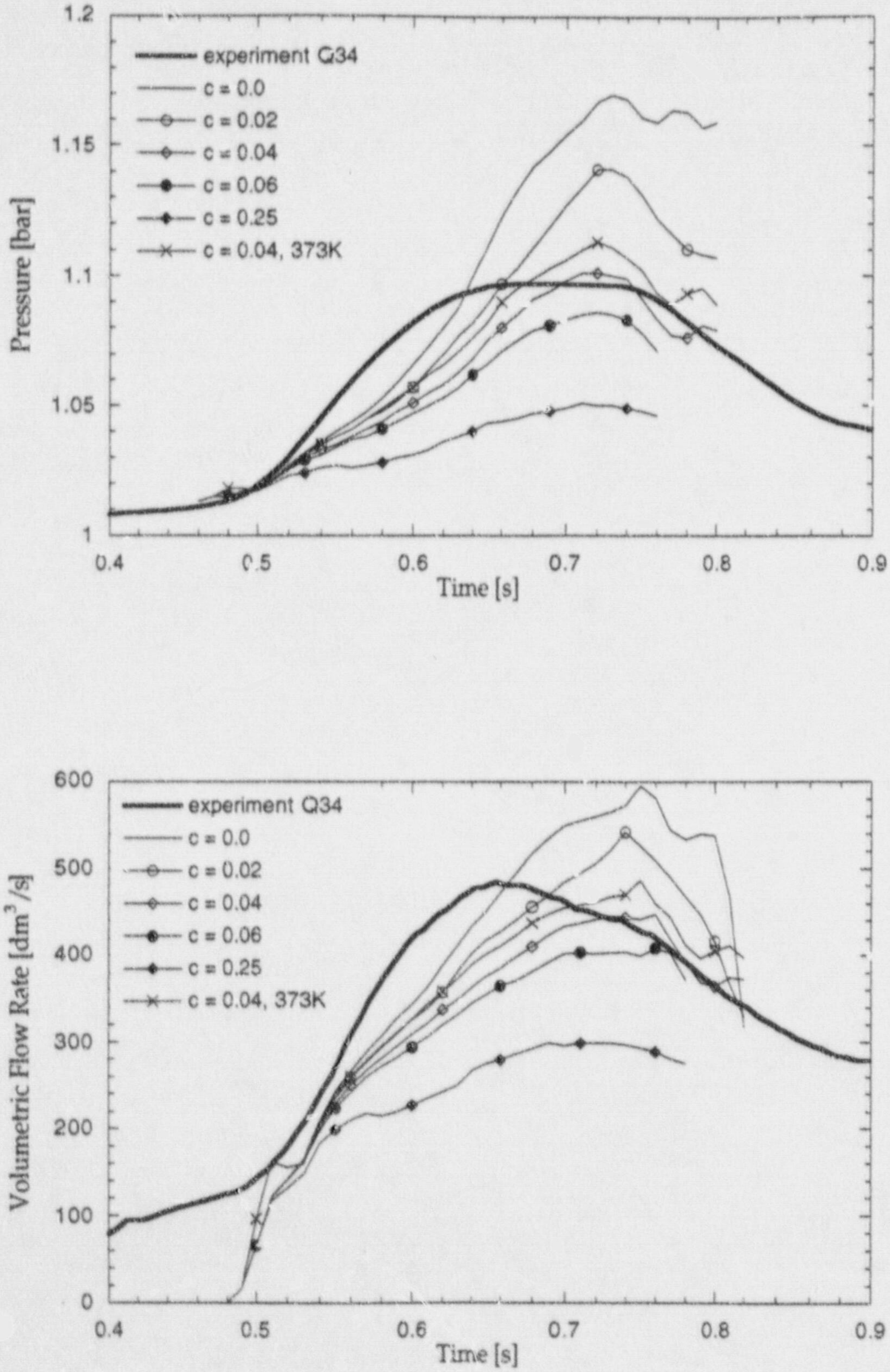

Figure 22. A full parametric on condensation for Q34.

[[ADDENDUM TO SECTION 3.2.2 OF DOE/ID-10504]]

THE FARO EXPERIMENTS

Here we reanalyze the FARO test L-14, with PM-ALPHA.L. Besides the Lagrangian treatment, the other key new ingredients are a shell-freezing model for the melt, and the full turbulence-controlled heat transfer on the liquid side of the interfaces, as described in the addendum to QUEOS.

Other specifications are as used previously, including the flow domain and discretization, shown in Figure 1. Also as previously we found a rather slow breakup (we use a value of $\beta = 40$ here), which is consistent with the relatively short free-fall distance in this test (~1 m). The melt emissivity was taken as 0.8. A sensitivity case was also run, with an emissivity of 0.75 and a breakup parameter of 45.

The calculated melt front trajectory is shown in Figure 2. This figure also contains the experimental front as indicated by thermocouples located along the vessel centerline. We find a systematic delay (relative to the calculation) of these thermocouple signals of ~200 ms. This indicates that the melt-coolant interaction is computed correctly (the velocities agree remarkably well). On the other hand, it is hard to explain the discrepancy in the free-fall time. Two possibilities exist. One, some inherent delay between the melt particle arriving at a location and actually "hitting" the thermocouple sufficiently for it to see the melt. Two, that there is some hesitation (~200 ms) for the melt to start the main pour, after the doors opened, and after perhaps a small melt quantity escaped at that instant. If the former is an accurate explanation, all is well in this calculation. If the latter is the explanation, or if still a third one more appropriate exists, the inlet melt specification may have to be revised. We could not find any discussion on potential delays in thermocouple indications of melt arrival. It is interesting that such delays can be seen in KROTOS test K38, albeit in only a few of the thermocouples.

The calculated void fraction and particle maps are shown in Figure 3. This visualization allows the identification of key events in the interaction, and will be referred to in the discussion of quantitative comparisons to the data that follow.

The pressure and pressurization rate transients are shown in Figure 4. Both in the experiment and calculations we can identify two regions, one with a strongly escalating pressure rate, followed by a more mildly decaying one. On the whole the trend is captured very well, and the quantitative agreement is very satisfying. With reference to Figure 3, we can see that the vapor "chimney" remains active up to ~1.3 s, and this is what seems to be feeding the pressurization. Soon after, the chimney is lost, the pressure rate turns into its decaying portion, to essentially disappear at ~2 s, when most particles have settled to the bottom. The sensitivity case shows a small effect only in the tail-end of the transient.

Interestingly enough, the pressure continues to increase, even after the cutoff of this vapor chimney (both in the experiment and in the calculation) — i.e., the period between ~1.3 and ~2.2 s. This is mainly because of compression of the freeboard volume (rather than vapor supply directly to it), by the piston-like pool motion, propelled from below (i.e., vapor generation at the pool bottom region). The calculated motion of this piston, i.e., level rise, agrees quantitatively with the experimental data, as illustrated in Figure 5. The upwards propelling of the pool is sustained by a balance between vaporization and condensation in the lower strata, which in turn is influenced by melt breakup and freezing rates, and by the overall circulation that, as seen in Figure 3, tends to propel subcooled liquid flow downward, in the central region, and a two-phase mixture upwards along the pool periphery. In addition, the pressurization rate is influenced by the condensation rates at the upper strata of the pool, itself in turn being influenced by the state of breakup (interfacial area), and the level of turbulence in the liquid. We made no attempt to look at these influences in more detail (mainly due to time limitations) nor to make any adjustments for them, relative to a more detailed local modeling effort. Nor have we made any effort in the local modelling of mixing in parallel flow, such as at the vapor or liquid columns seen to develop in the early and late portions of the interaction, respectively. The flow patterns seen in Figure 3 suggest more detailed local measurements that could provide the basis for such modelling enhancements, and could also improve the characterization of the experiment for code verification purposes.

The fuel energy disposition, in the course of the transient, is shown in Figure 6. We can see that a major portion of the energy loss from the fuel goes to steam production (and compression). More specifically, up to 0.8 s essentially all energy goes to vapor. After 0.8 s, as subcooling develops, a significant fraction of this energy, especially after ~2 s, goes to liquid. A small amount only (~13 MJ at the end of the calculation) is radiated through to the vessel walls. Clearly, both energy transfer to liquid in subcooled boiling, and non-local radiative transport, play very important roles.

The calculated temperature transients (see Figure 1 for position identification) are shown together with the data in Figures 7 and 8. The data exhibit significant asymmetries, and these are only indicative of the difficulty in detailed quantitative comparisons. Still, some overall trends can be discerned. For example, the inner column of thermocouples show liquid temperature rises that for the most part are similar to those calculated. The outer column shows delayed and gradual rises, a trend which again for the most part is reflected in the calculations. To some degree this supports the circulating nature of the flow, and the upward two-phase flow along the outer regions of the vessel seen in the calculation. The timing of these rises, however, is somewhat delayed in the calculation, especially in the upper portions.

The interpretation of the temperatures measured in the freeboard volume requires some care. First, we see the vapor to superheat, by the fuel passage in the early times. As the water swelled past the particular location (as indicated by the 0.5 and 0.9 arrows in the figures), the thermocouple was first exposed to a two-phase medium and then to the liquid medium. The measured temperatures, then, transited, correspondingly, to the saturation temperature and then to the liquid temperature (subcooled). This is especially clear in the lower thermocouples positioned 40 cm above the initial water pool. In the upper thermocouple, positioned at 80 cm above the initial water level, we see an even earlier "quenching" by the spray, and following of the saturation line, and a longer, therefore, duration of this trend. Once significant liquid fraction reached that location, however (marked according to the calculation by the 50% void arrow) we see the experimental trace to depart from saturation. At the top location we probably underestimate condensation (predicting lower temperature), but at the lower location we see a better quantitative agreement. The rise in liquid temperature at ~2.2 s is due to the condenssation of an increasing amount of steam which is seen to penetrate upwards, as discussed above (see Figure 3).

The evolution of the debris particle size distribution is shown in Figure 9. Note that at 1 s the melt supply has ended, and the debris mass with the initial particle dimension begins to deplete. Also, at 1.7 s the cutoff criteria for melt breakup appear to have been met (more than 50% solid fraction, local void fraction in excess of 70%, or droplet size no more than 2 mm), and the spectrum has ceased to change. As we see in Figure 3, this is the time where all fuel has reached the bottom of the vessel. In Figure 10, we show the generation of debris, defined to consist of particles more than 50% frozen. In the same figure, we also show debris defined by the same 50% frozen criterion, but in addition limited to include only particles of sizes less than 1.3 cm. Note that debris with diameters greater than this size (the difference between the two curves) were all generated after 1.7 s when the breakup was finished. If we assume that the freezing of these "large" molten debris are likely candidates to fuse at the bottom to form a "cake," we can see that according to the calculation this would amount to ~20 kg, as found in the experiment. The remainder is shown as a particle size distribution, together with the debris analysis from the experiment in Figure 11. The agreement is quite satisfactory. This is one more indication of the internal consistency in the calculation, and its relevance to the experiment.

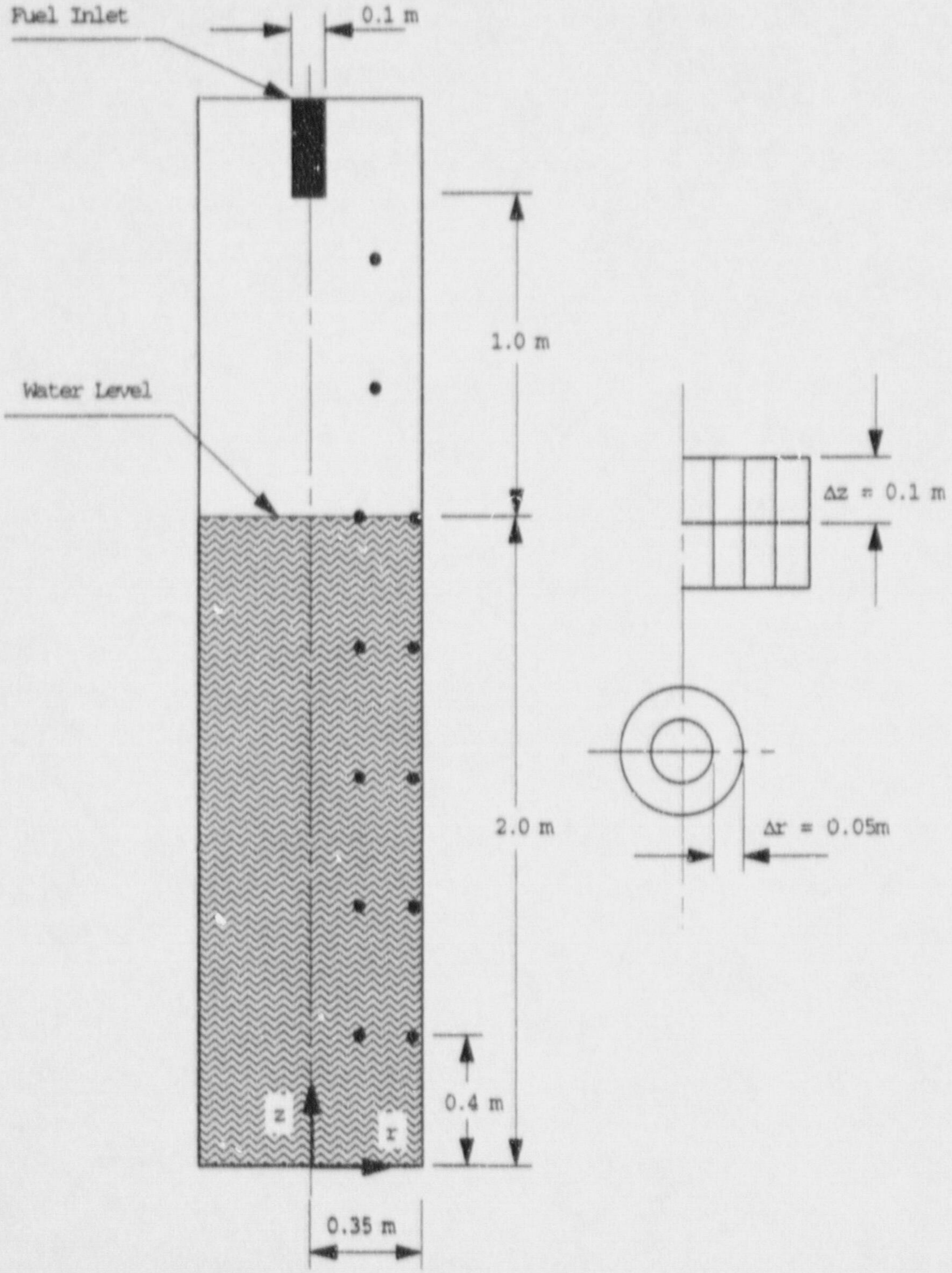

Figure 1. The computational domain and discretization used in PM-ALPHA (axisymmetric, 2D) to simulate FARO test L-14. Also shown are the thermocouple positions at which comparisons with data are made.

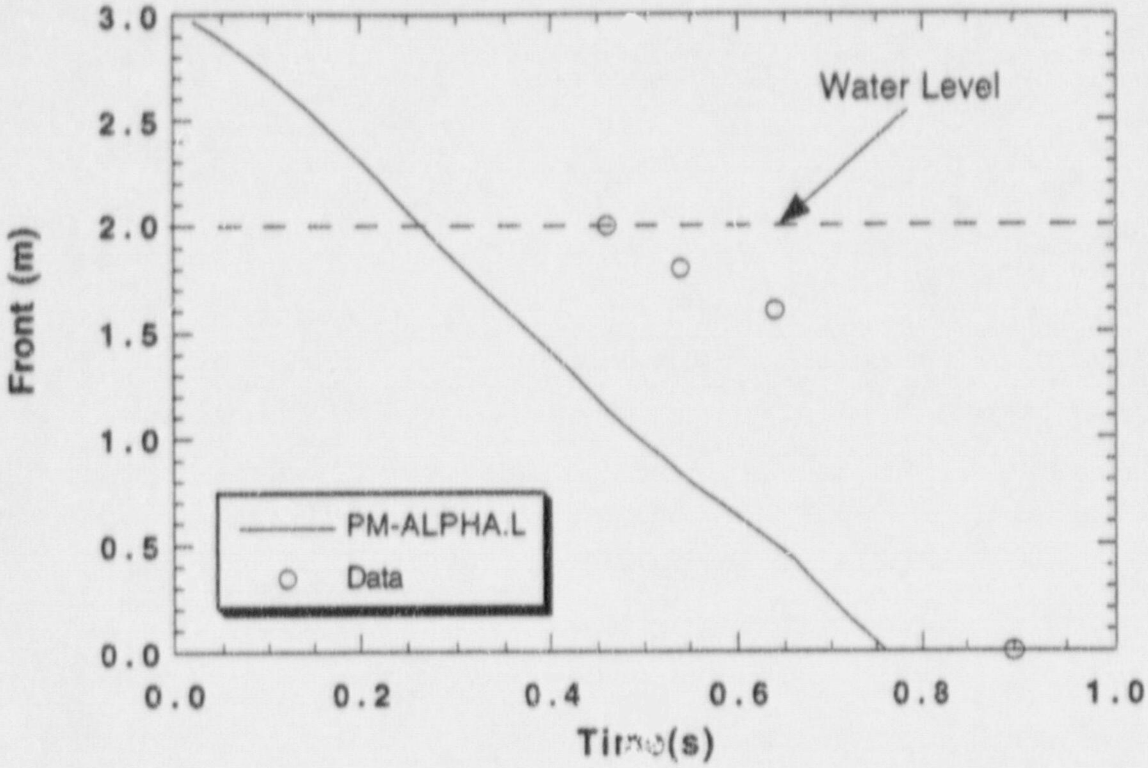

Figure 2. Predicted melt front advancement against the "indications" obtained from the centerline thermocouples in the experiment.

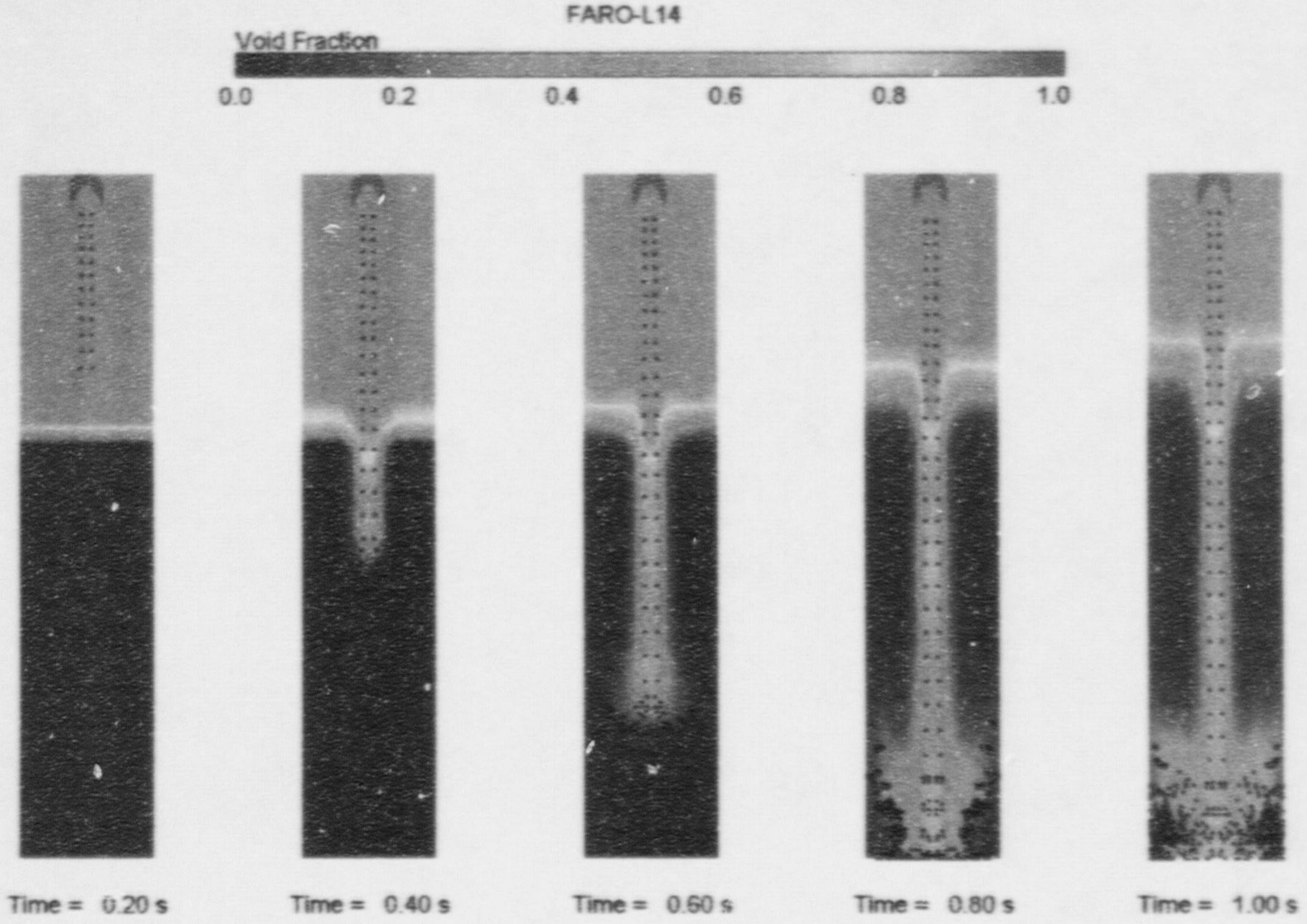

Figure 3. Cross-sectional void fraction maps computed by PM-ALPHA.L for test L-14. Only the flow domain below the melt inlet nozzle is shown. The "particles" represent ring clusters.

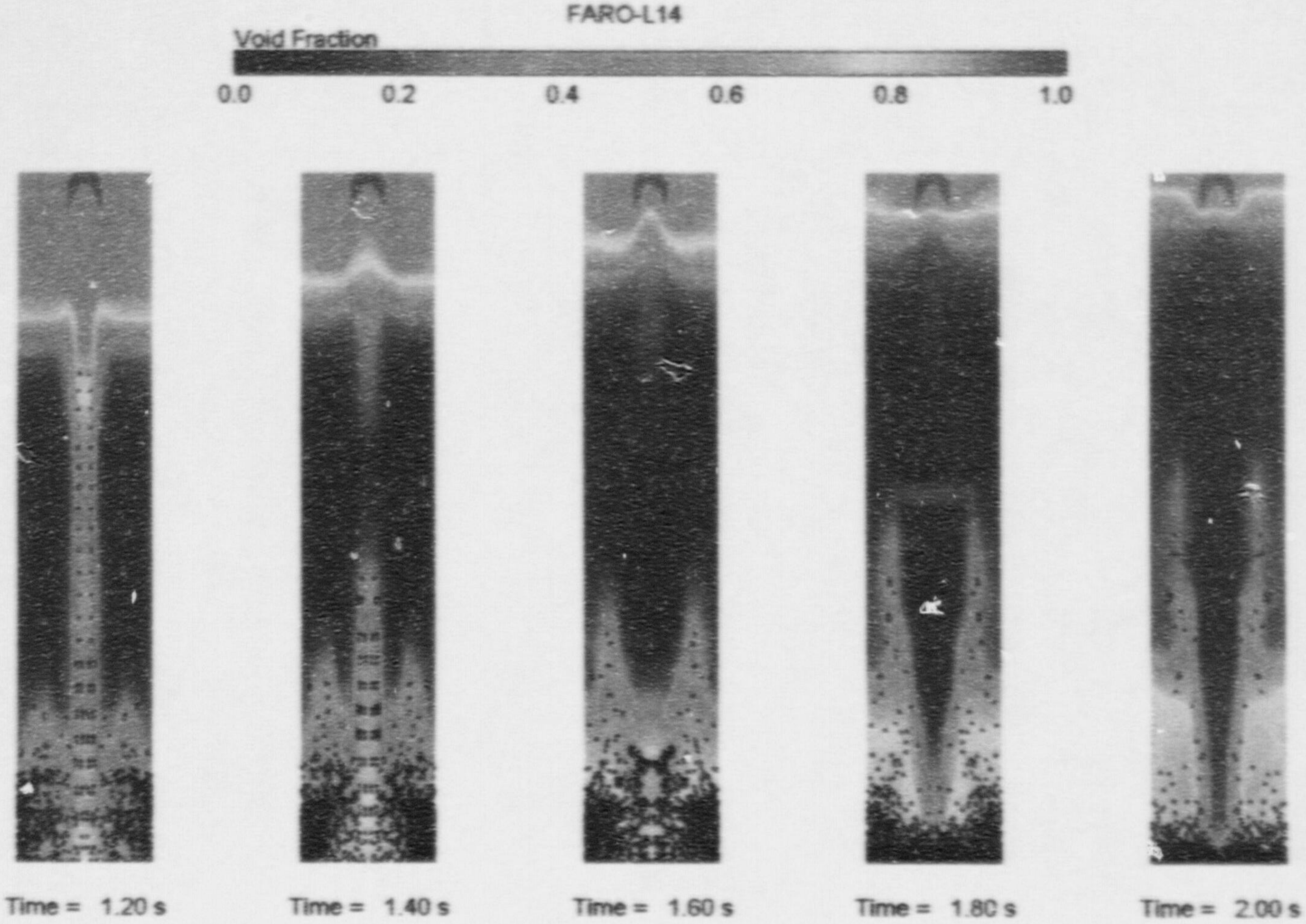

Figure 3. (Continued).

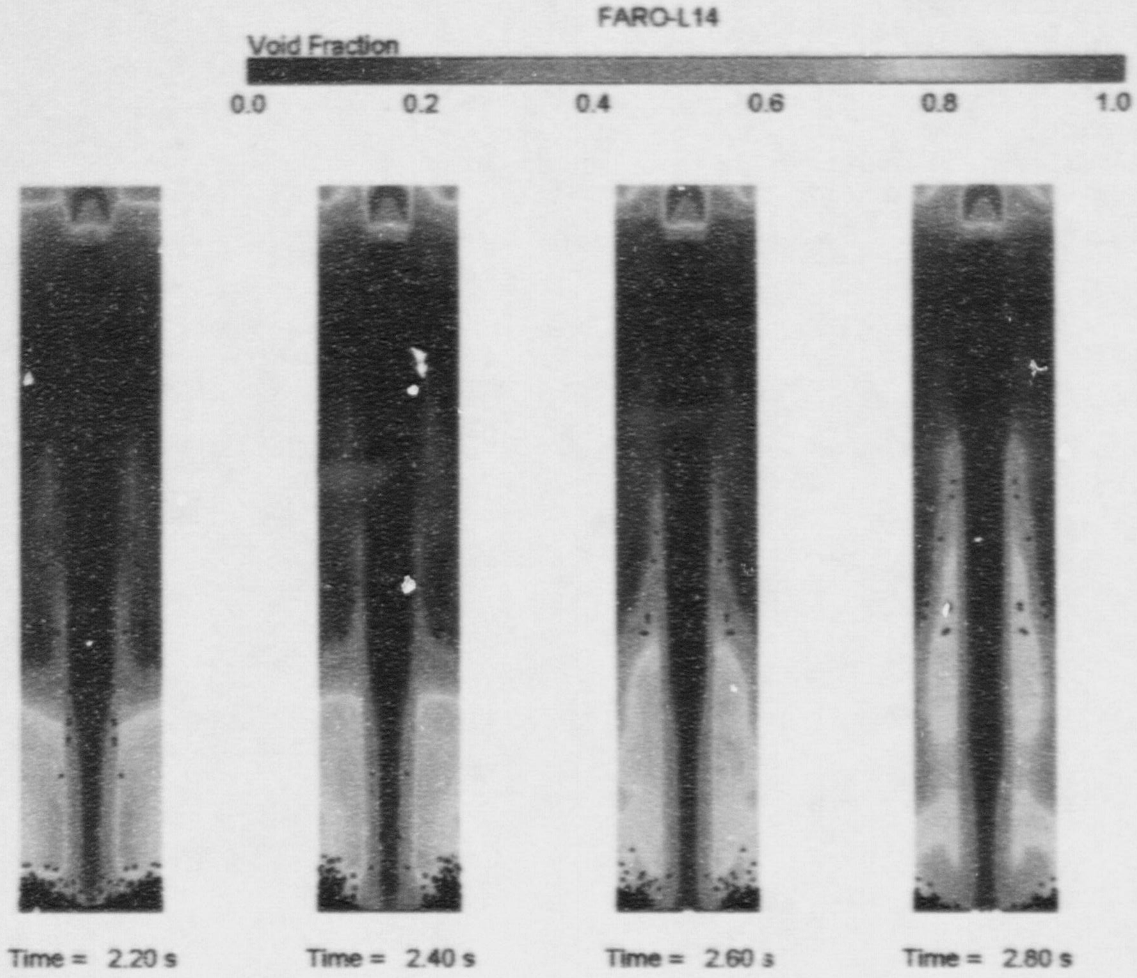

Figure 3. (Continued).

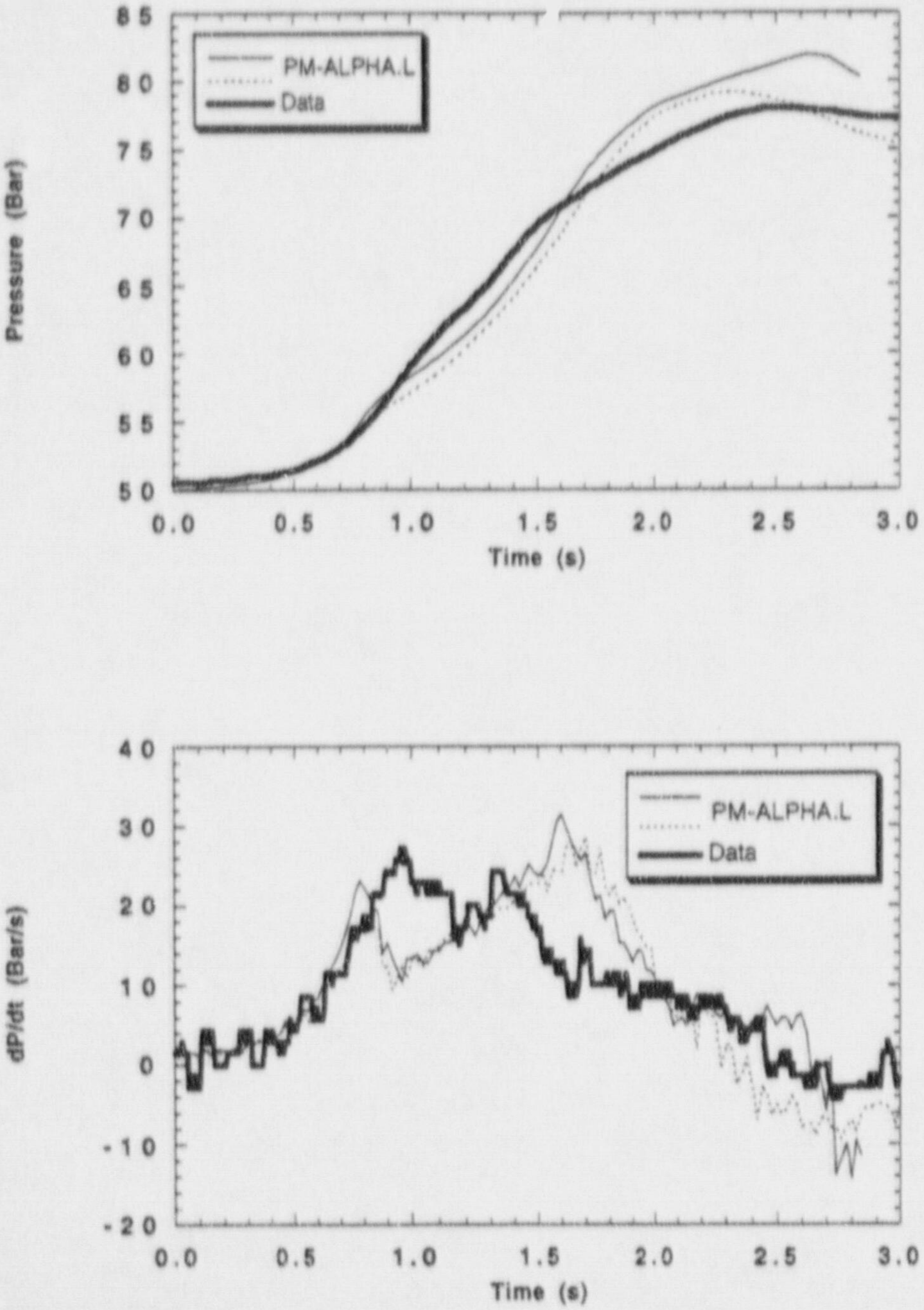

Figure 4. Predicted pressure and pressurization rate transients compared to the data in L-14. (——) emissivity 0.8, breakup parameter 40. (……) emissivity 0.75, breakup parameter 45.

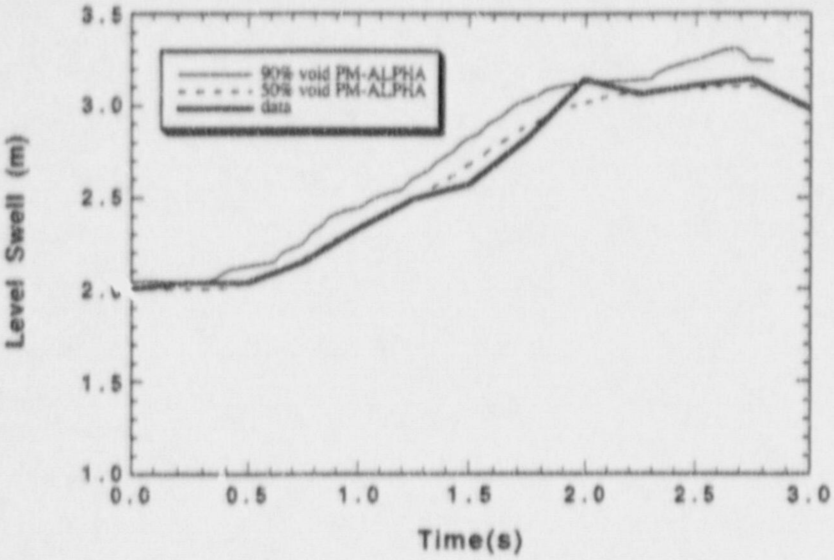

Figure 5. Predicted level swell compared to the data in L-14.

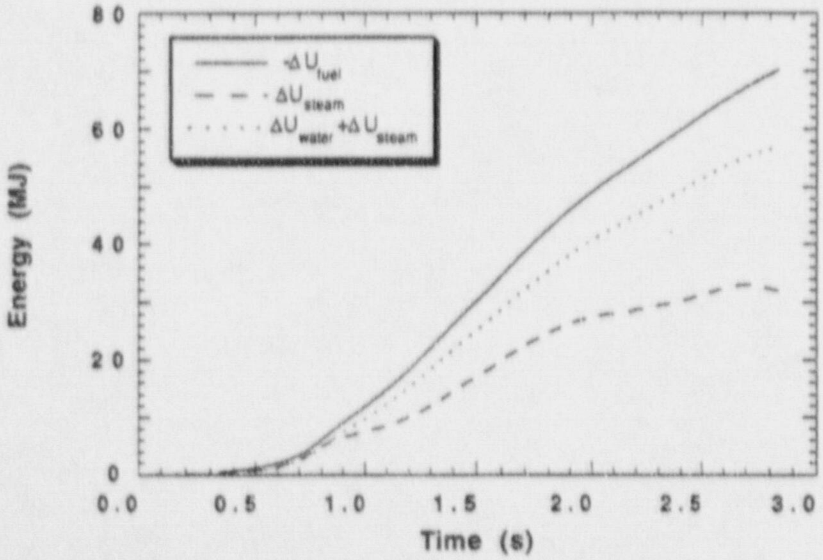

Figure 6. Calculated disposition of energy transferred from fuel to the coolant.

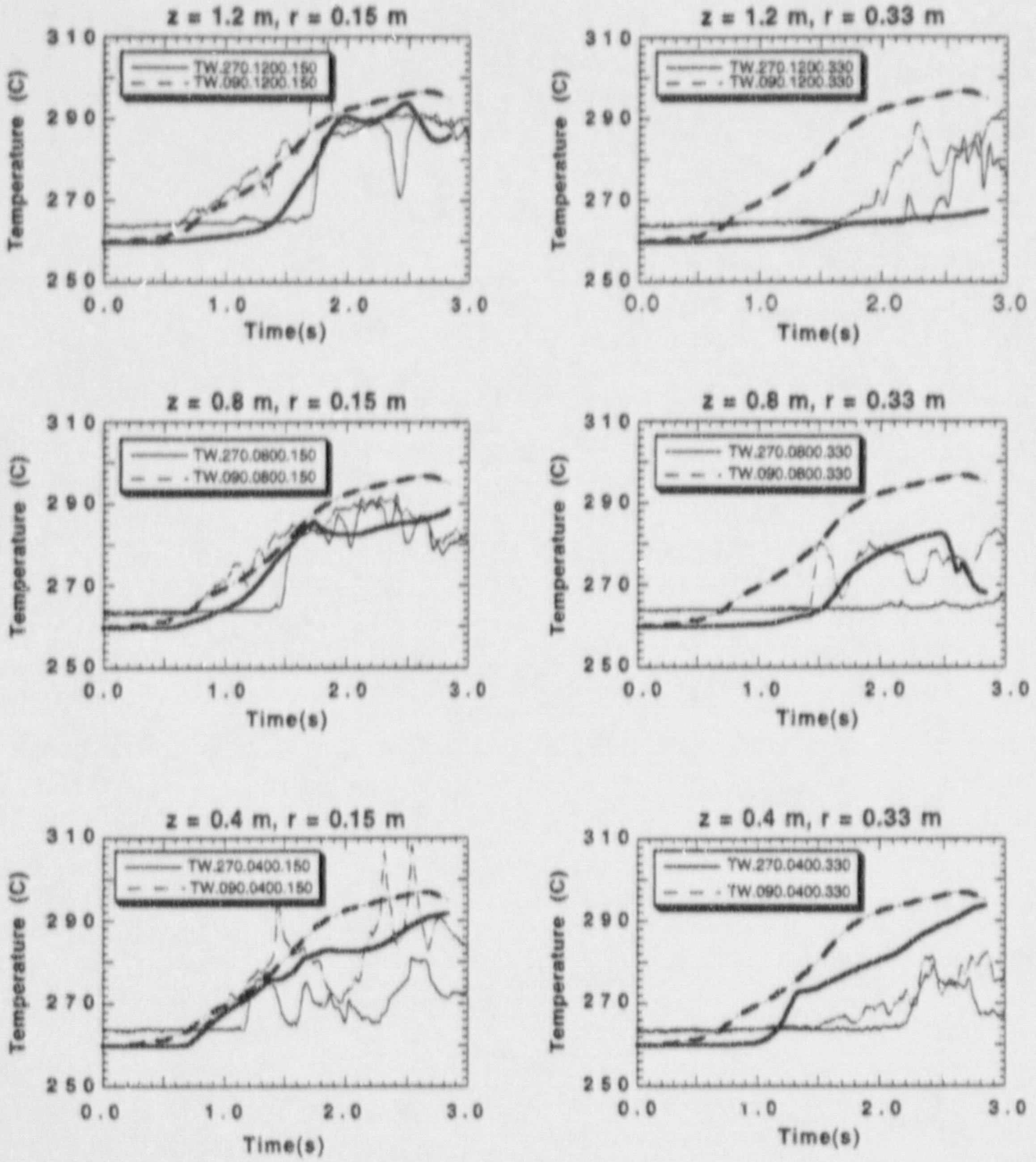

Figure 7. Calculated and measured liquid temperature transients. The dark solid and dashed lines correspond to the calculated liquid and saturation temperatures, respectively.

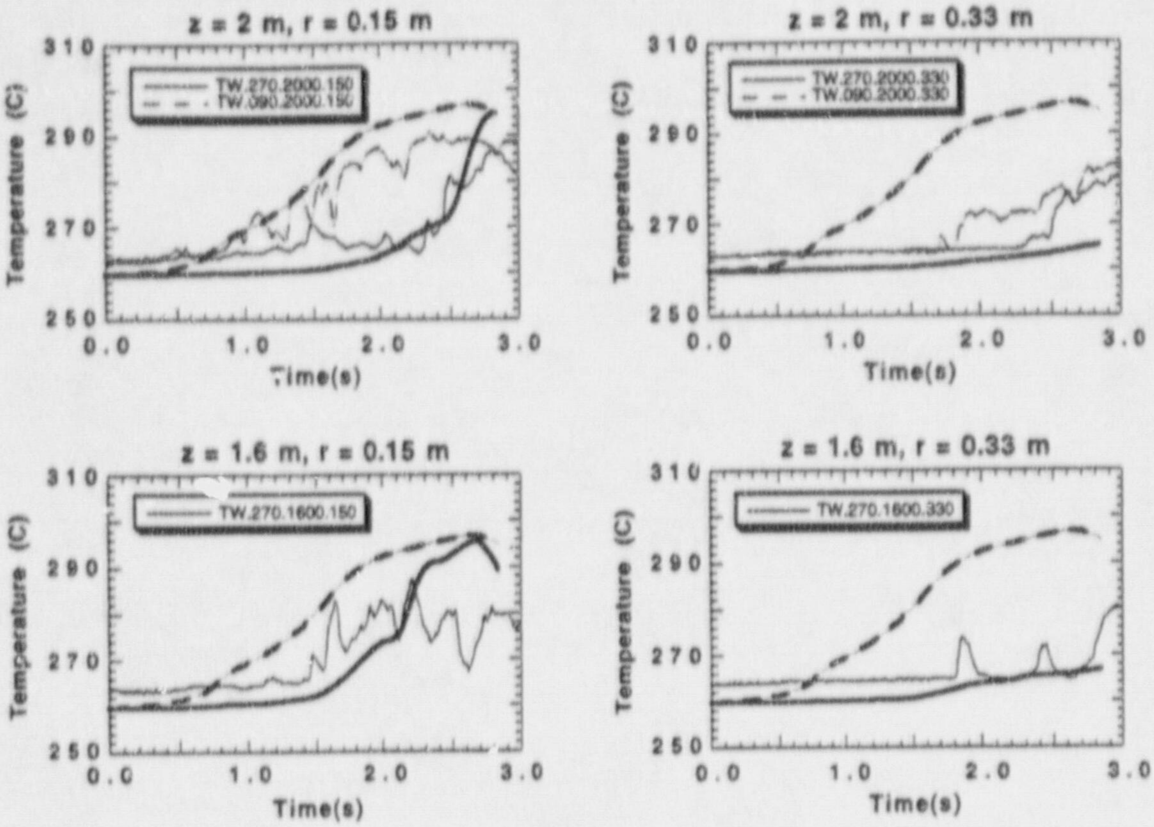

Figure 7. (Continued).

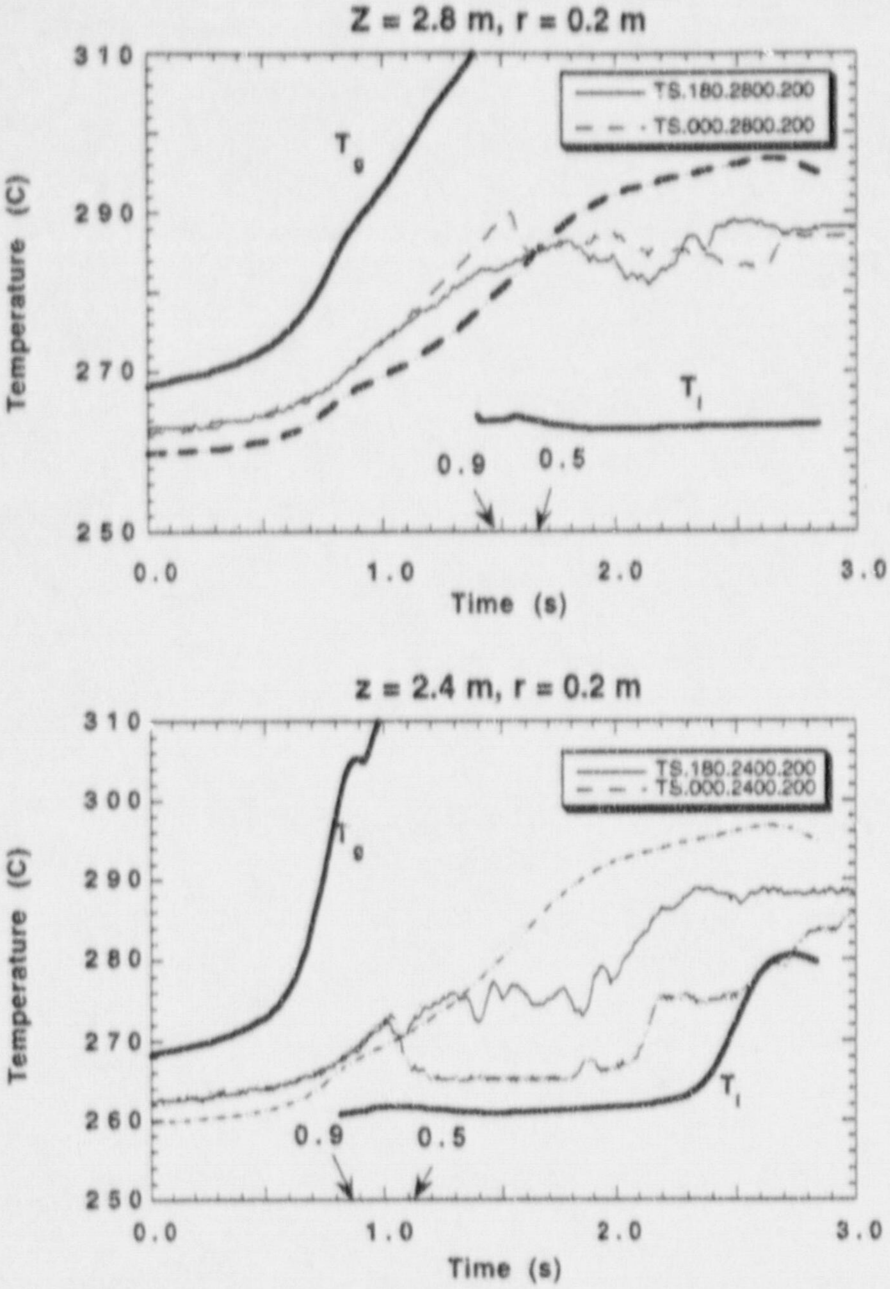

Figure 8. Measured temperatures at two positions in the freeboard volume (40 and 80 cm above the liquid level). Also shown (heavy lines) are the calculated liquid (T_ℓ), vapor (T_g) and saturation temperatures (– · – · –). The arrows show the arrival of 50 and 90% void fraction coolant.

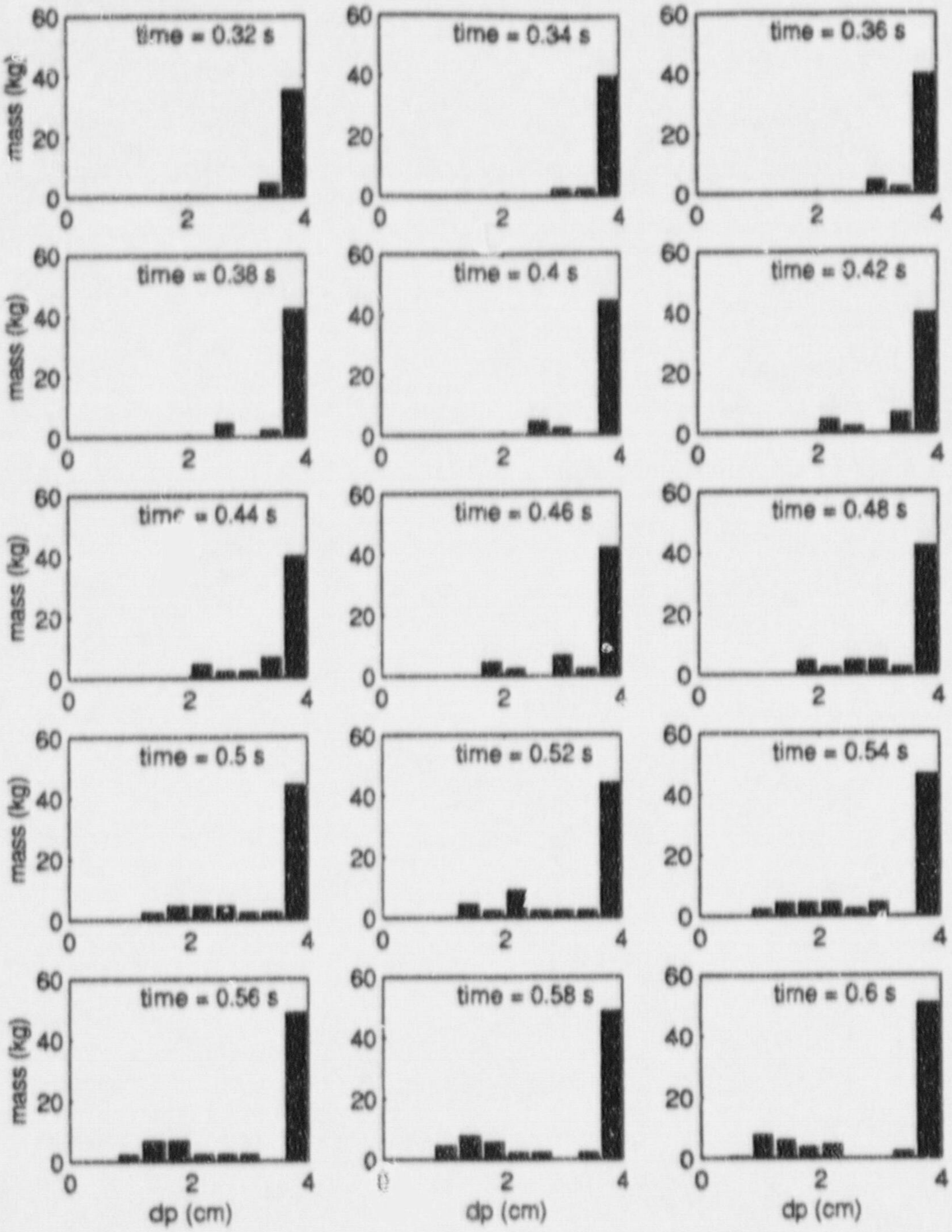

Figure 9. The evolution of melt particle distribution computed in L-14. Note that at 1 s the melt supply is terminated.

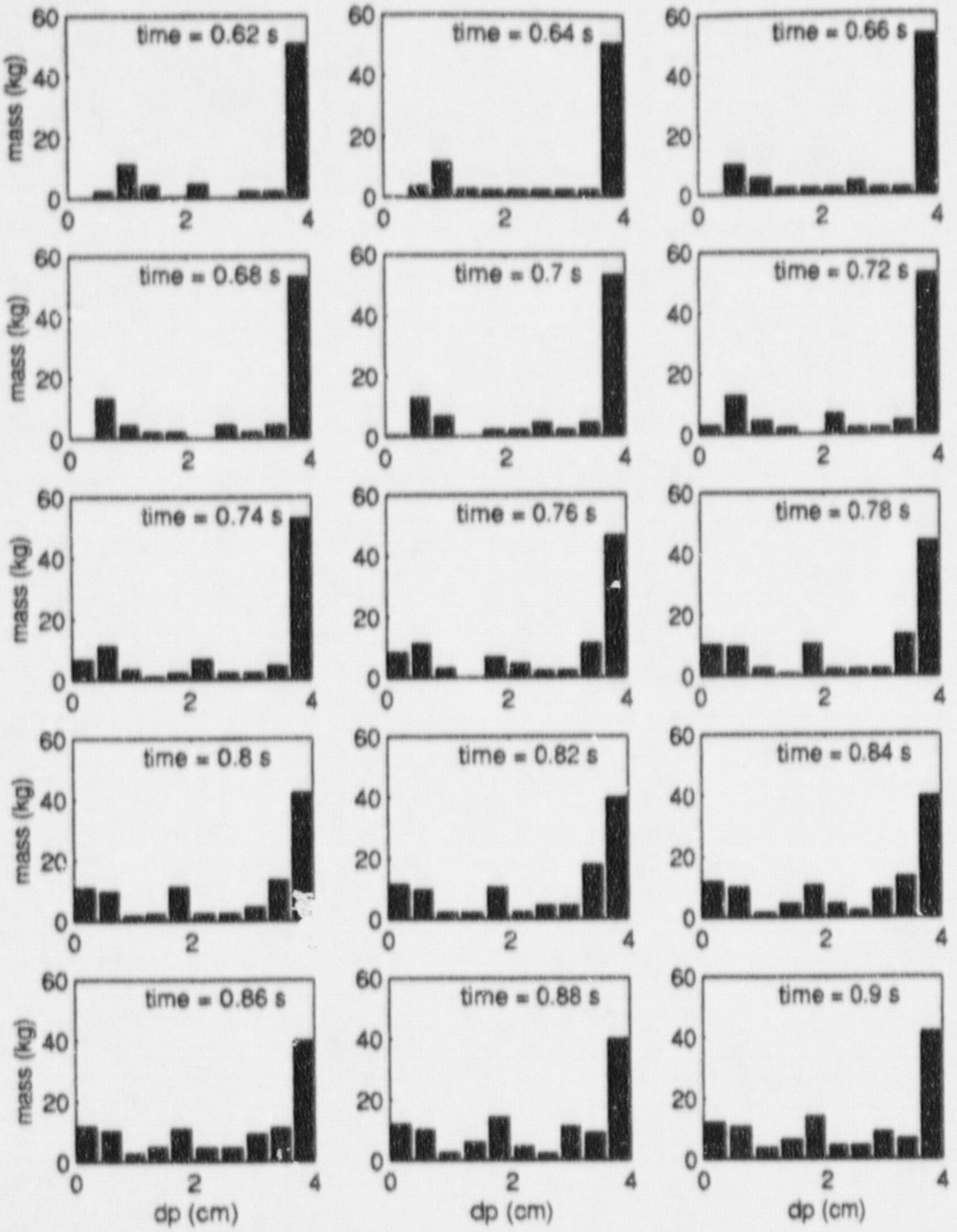

Figure 9. (Continued).

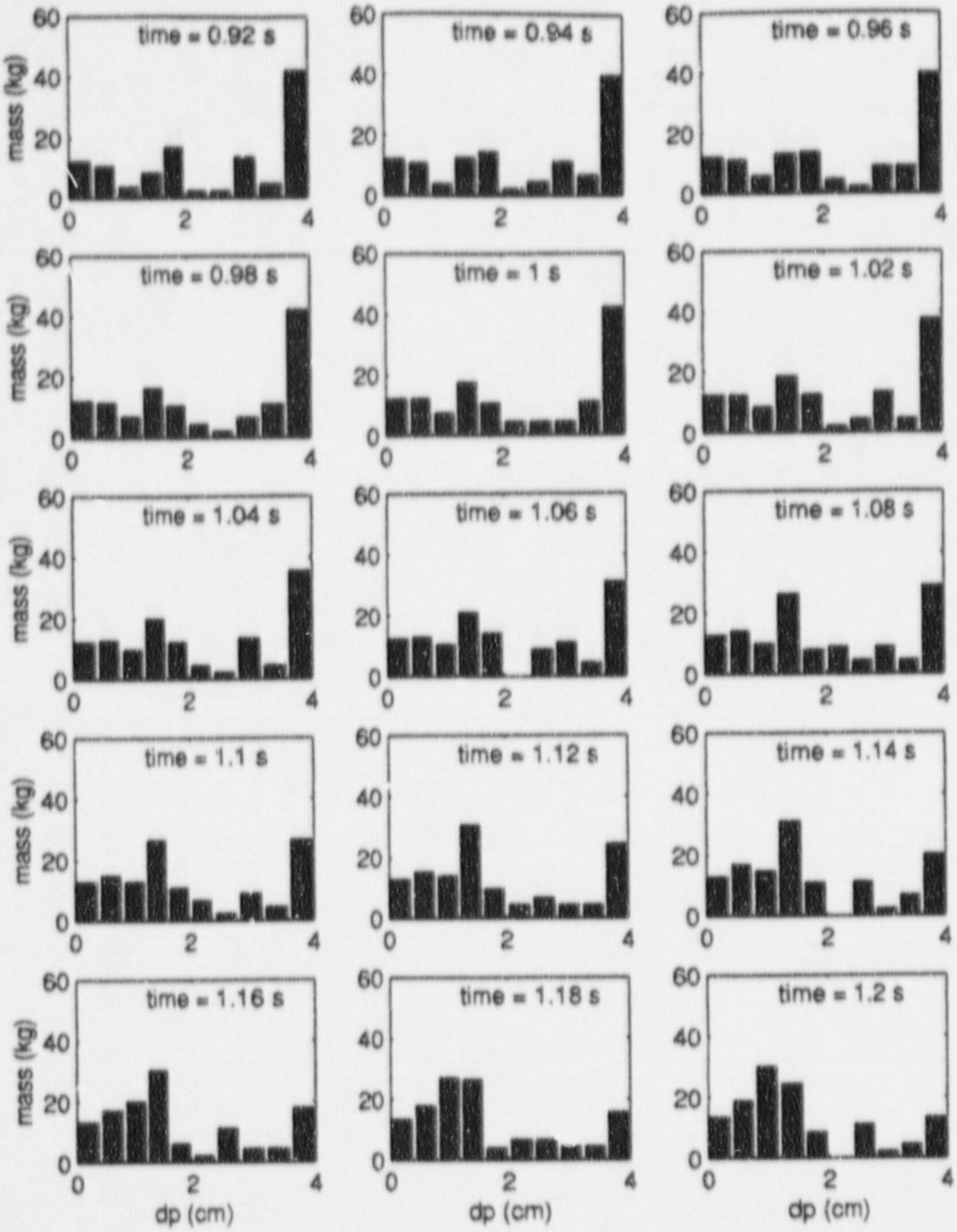

Figure 9. (Continued).

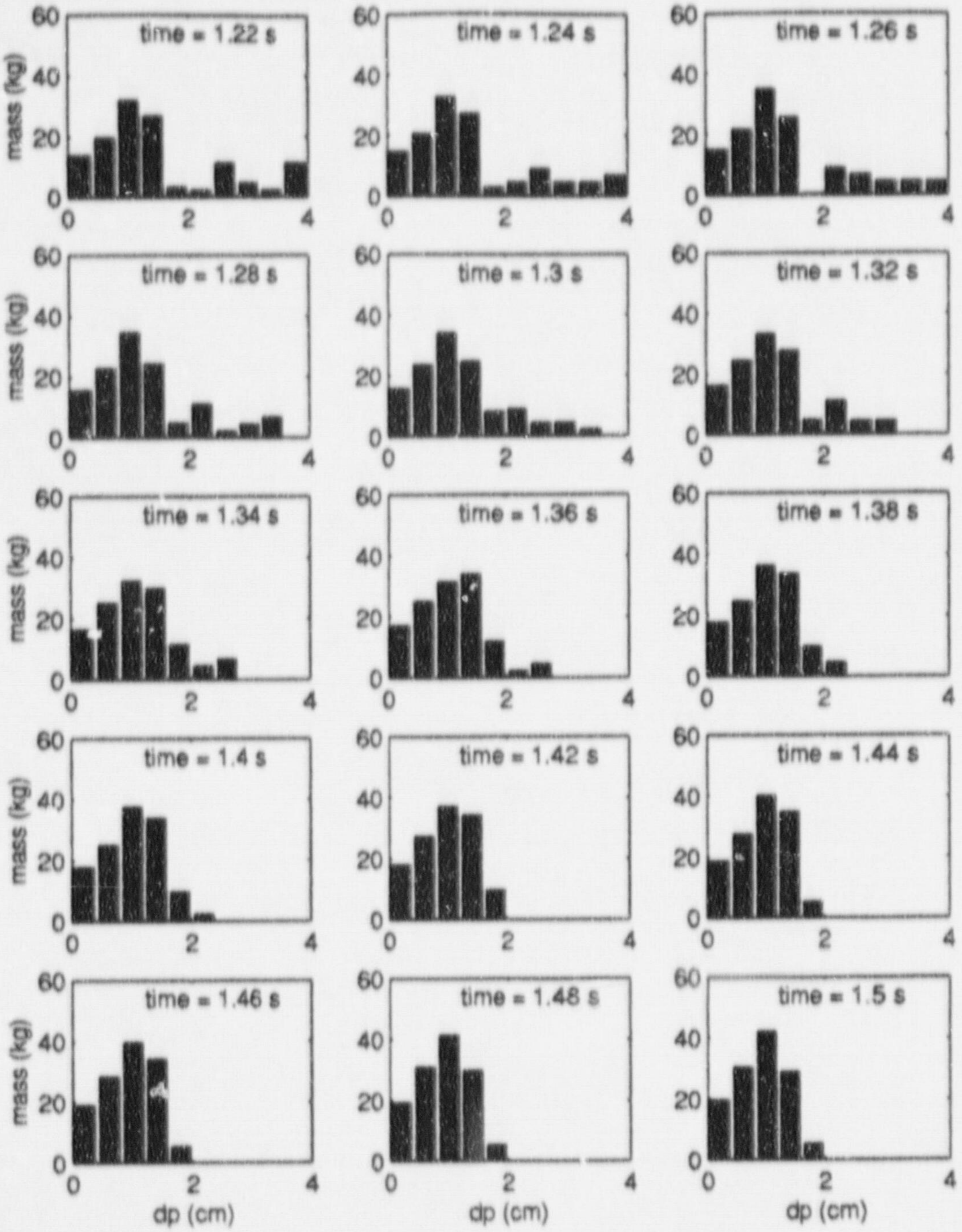

Figure 9. (Continued).

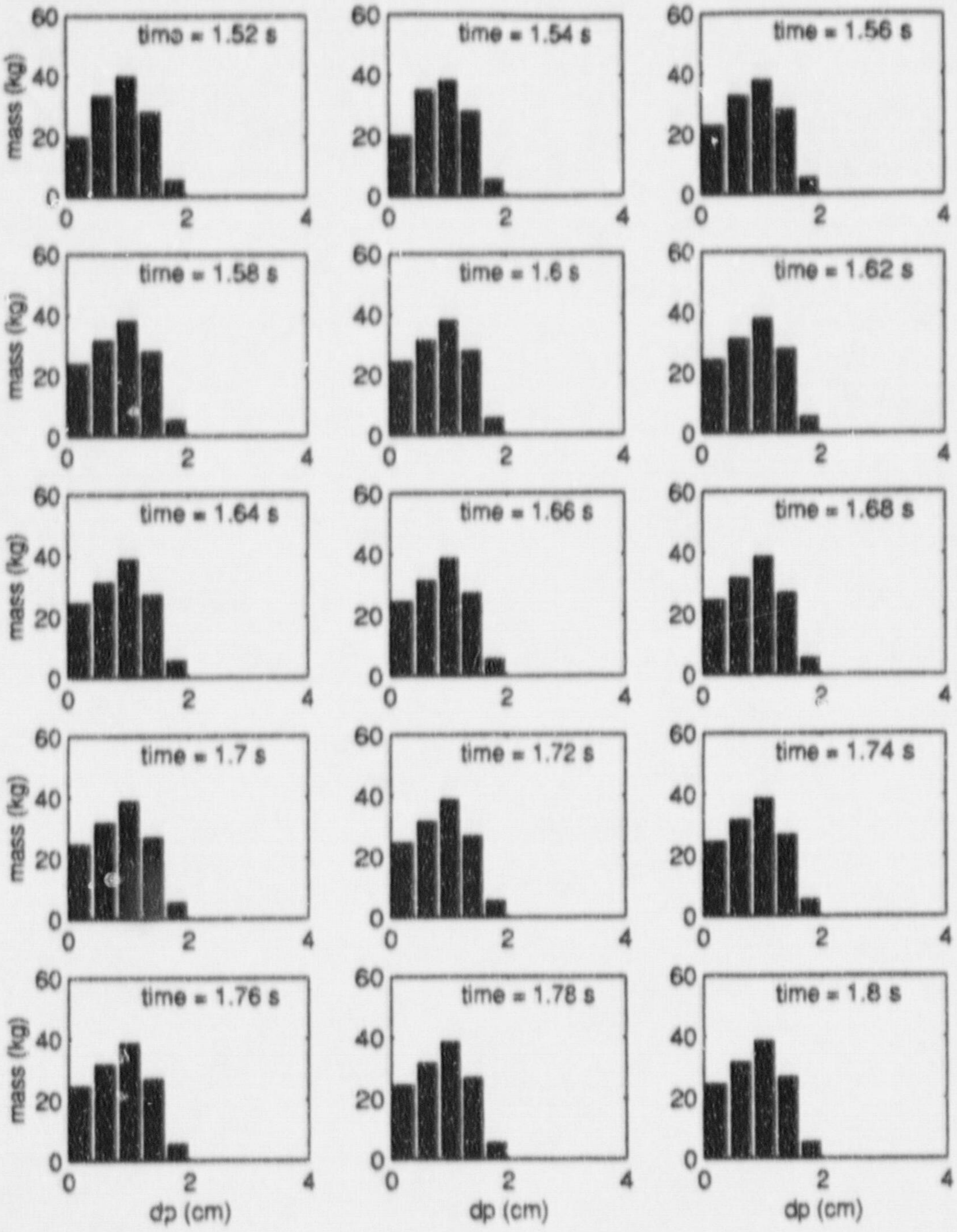

Figure 9. (Continued).

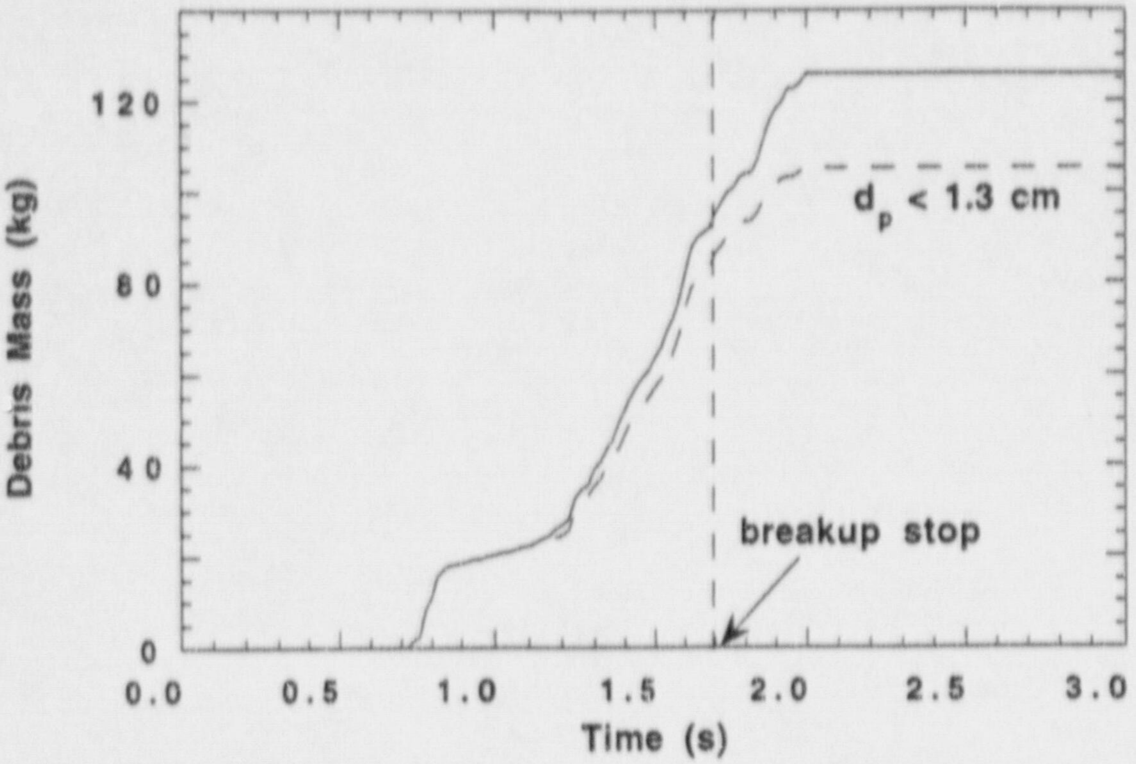

Figure 10. Calculated buildup of the debris mass in the calculation. The solid line represents all debris, while the broken line presents debris with diameters less than 1.3 cm.

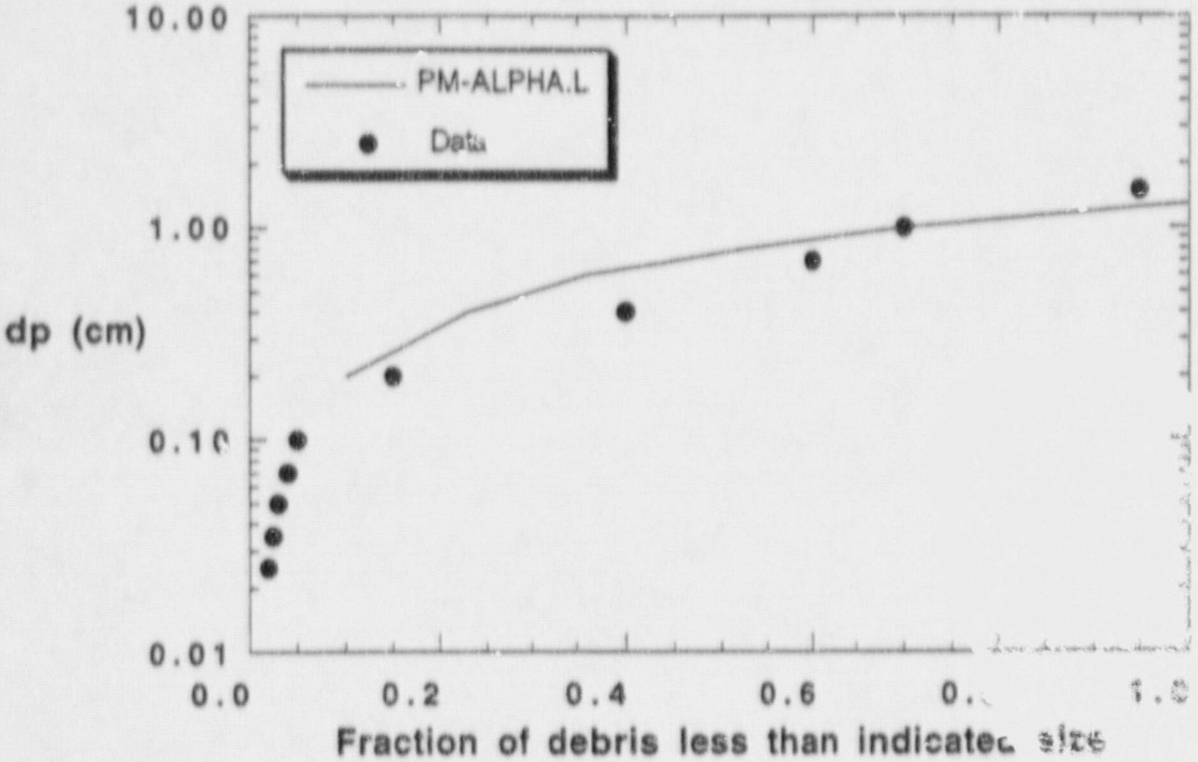

Figure 11. The debris particle size distribution from the calculation compared to that found in test L-14.

[[ADDENDUM 3 TO APPENDIX B of DOE/ID-10504]]

MAGICO-2000 TEST SIMULATIONS WITH PM-ALPHA.L

Here we consider the MAGICO-2000 experiments summarized in Table 2 of Addendum 1 to Appendix B (hereafter to be abbreviated simply as Addendum 1), with the help of PM-ALPHA.L. These experiments cover wide ranges in particle temperature and size, and most importantly in inlet particle volume fractions. As explained in Addendum 1, the high value (~5%) creates what we have called the "inertia regime," while the low value is well within a "thermal regime" of behavior.

All runs were conducted with ZrO_2 particles in a "thick" (20 cm) slab geometry, and open test section. In the 0 °C subcooling runs the water was fully saturated (over the height of the pool), while in the 10 °C subcooling run the water was at a uniform temperature of 90 °C.

The principal data from these experiments is on the structure of the interaction zone, as visualized and quantified by flash X-ray shots. This is the critical and most fundamental aspect of the computations under "trial," and these MAGICO experiments remain unique in this respect. In addition, we have visual records to compare with predicted "external" characteristics and in particular with the propagation of the interaction front. In the presentation that follows, we begin with the external characteristics.

The computations were carried out with the 3D PM-ALPHA.L code, on a 5 x 5 x 5 cm Cartesian grid that exactly simulates the test section (see Addendum 1). Recall that in the Eulerian code calculations presented in Addendum 1, a rather fine, 2.5 x 2.5 cm, grid was used, in order to adequately control numerical diffusion. This is no longer a concern here, thus allowing computational efficiency with a coarser grid.

Representative frames from the video records and the mixing zone front positions advancing with time are shown in Figures 1 and 2 respectively. All of these figures are put in the context of the X-rays, to be presented and discussed below, by showing the locations of the two cassettes that hold the photographic film. Front advancement data are missing for runs Z11 and Z12, because of too intense glare in the former, and power failure (lighting failure) in the latter. For these two runs, therefore, we show only the particle front as read from the X-ray films. For all other runs the front positions were very clearly identifiable, and the uncertainty in this measurement is negligible in the context of comparisons made. In Figure 2, we also show the trailing edge of the clouds if within the field of view of the X-rays. Finally, Figure 2 also contains the results of the numerical simulations.

With the possible exception of Z11 and Z12 (Figures 2(a) and 2(b)), the results of these comparisons is quite satisfying. In these runs, there appears to be a "breakup" of the front, into a faster-propagating "bulge," similar to what has been observed in some of the previous MAGICO runs (see Appendix B). This may be an interesting area for future investigations.

The X-ray images, as well as quantified reproductions, were provided already with Addendum 1. Here, in Figure 3, we provide improved renderings of the latter, having eliminated (whitened) the particles, by manual data processing in runs ZT14, ZT15, and ZT16—this allows the eye to better focus on the coolant void fraction maps. Comparisons with PM-ALPHA.L predictions can be made with reference to Figure 4. Complete evolution of the simulated interactions are shown in Figure 5. These are helpful in providing context for Figure 4, and in addition they allow qualitative comparisons on overall features as found in the experiments (Figure 1).

All of these comparisons are, again, quite satisfying. In particular, we note the quantitative comparison of void fractions, and their distributions. (Note, for example, the liquid boundaries at the edge of the voided zone, in the subcooled run Z12 in Figure 4(b)). Also remarkable is the effect of this subcooling as compared to the saturated run Z11, where the interaction zone can be seen to grow clearly wider and outside of the X-ray film boundaries, in good agreement with the experiment. On the other hand, clear distinctions can also be seen with the "inertia hole" of cold run ZCN (see Addendum 2 to Appendix B) under conditions quite similar to Z11 (except of the particle temperature, of course). Overall the subcooled interaction was quite mild, as compared to the saturated one where both two-phase coolant and resuspended particles were carried out the top of the test section, some 0.7 m above the initial water level. This behavior (Figures 1(a) and (b)) was also well predicted (Figures 5(a) and (b)).

Also, the particle fractions, not shown in the figures, are predicted well. For the more dense cloud (first three runs) this is manifest by the prediction of the cloud length in the mixing zone. For the dilute clouds (last three runs), we obtain from the X-rays a rather uniform particle volume fraction of ~0.4 to 1% which agrees with the prediction. An interesting resuspension phenomenon (leading to local particle volume fraction of ~2%) predicted to occur at the top of the mixing zone at 0.8 s, for run ZT16, is not seen in the X-ray image; however, this is seen clearly in the video record and could have been just missed in the X-ray shot. This is based on Figure 5(f), where the resuspension is seen to develop just about 100 ms prior to the X-ray shot.

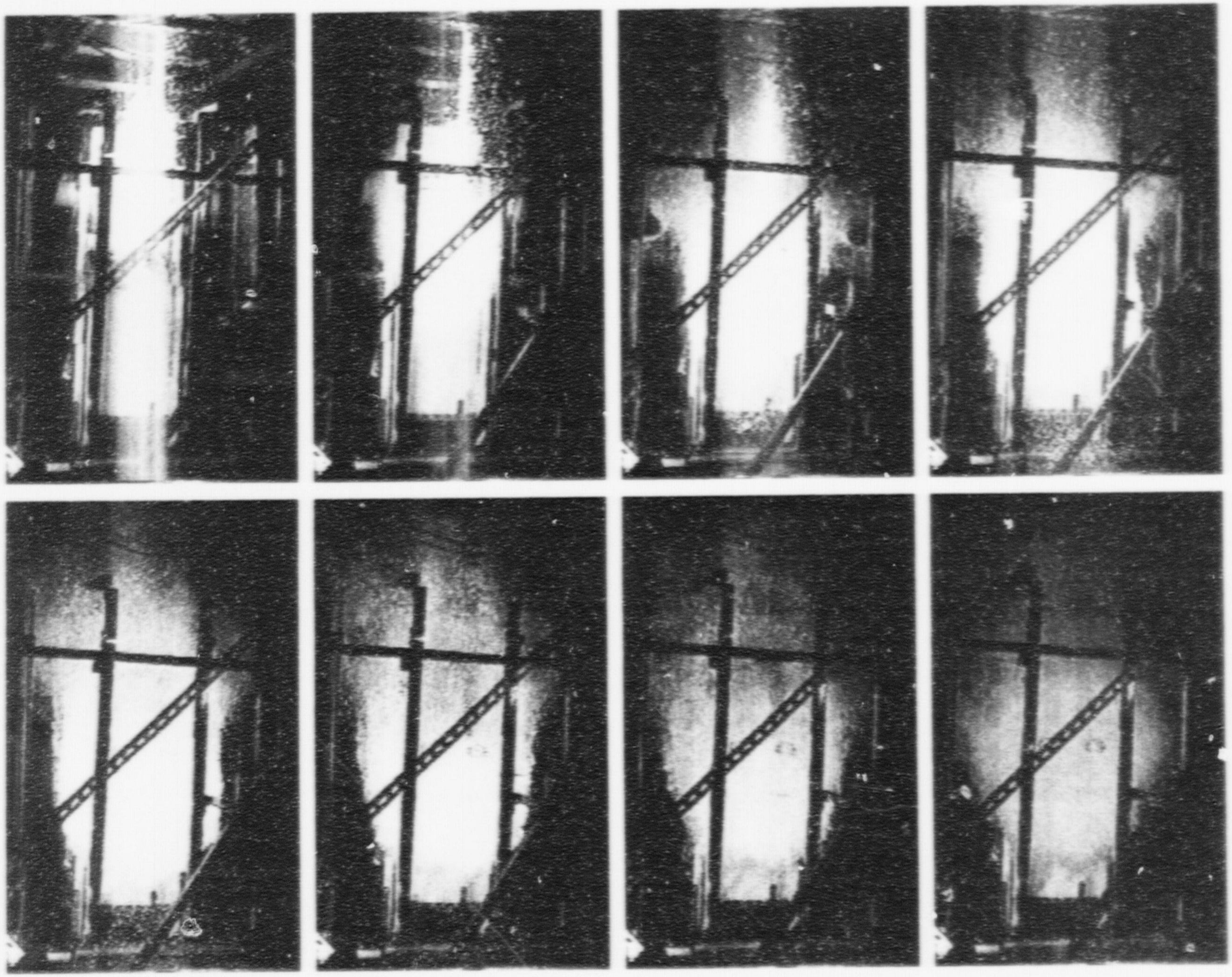

Figure 1(a). Video record of Run Z11. The frames are at 100 ms intervals.

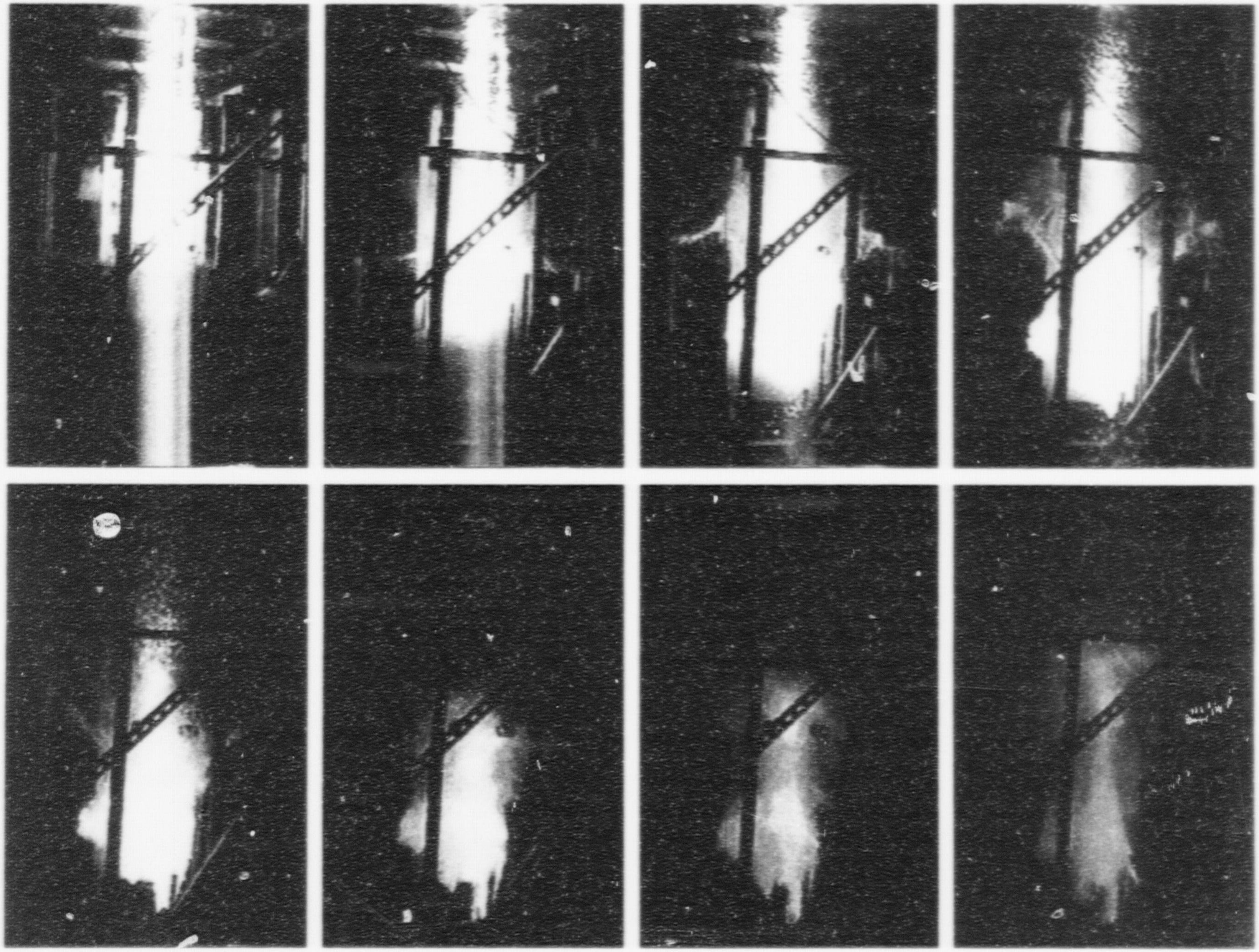

Figure 1(b). Video record of Run Z12. The frames are at 100 ms intervals.

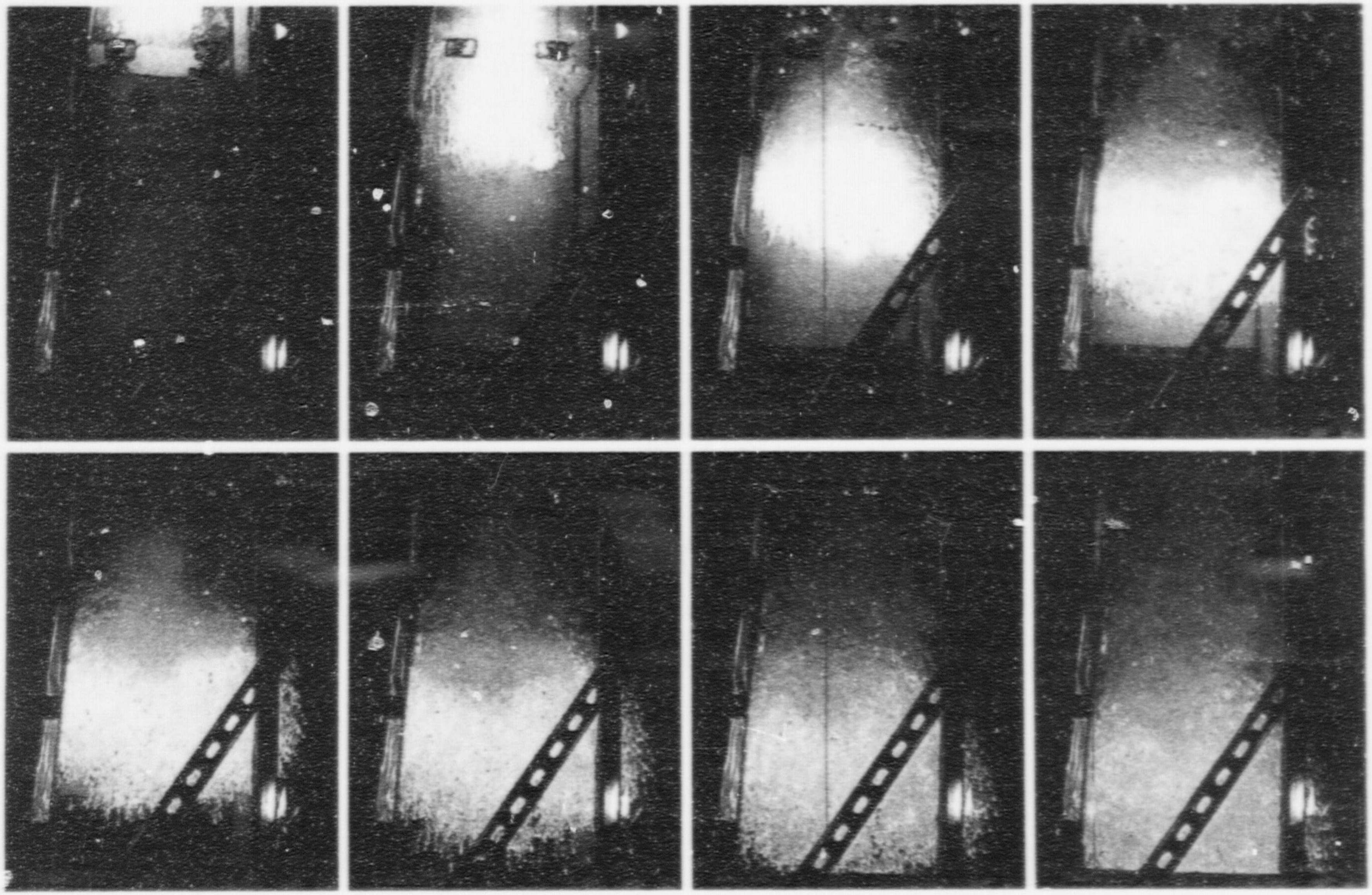

Figure 1(c). Video record of Run Zb13. The frames are at 100 ms intervals.

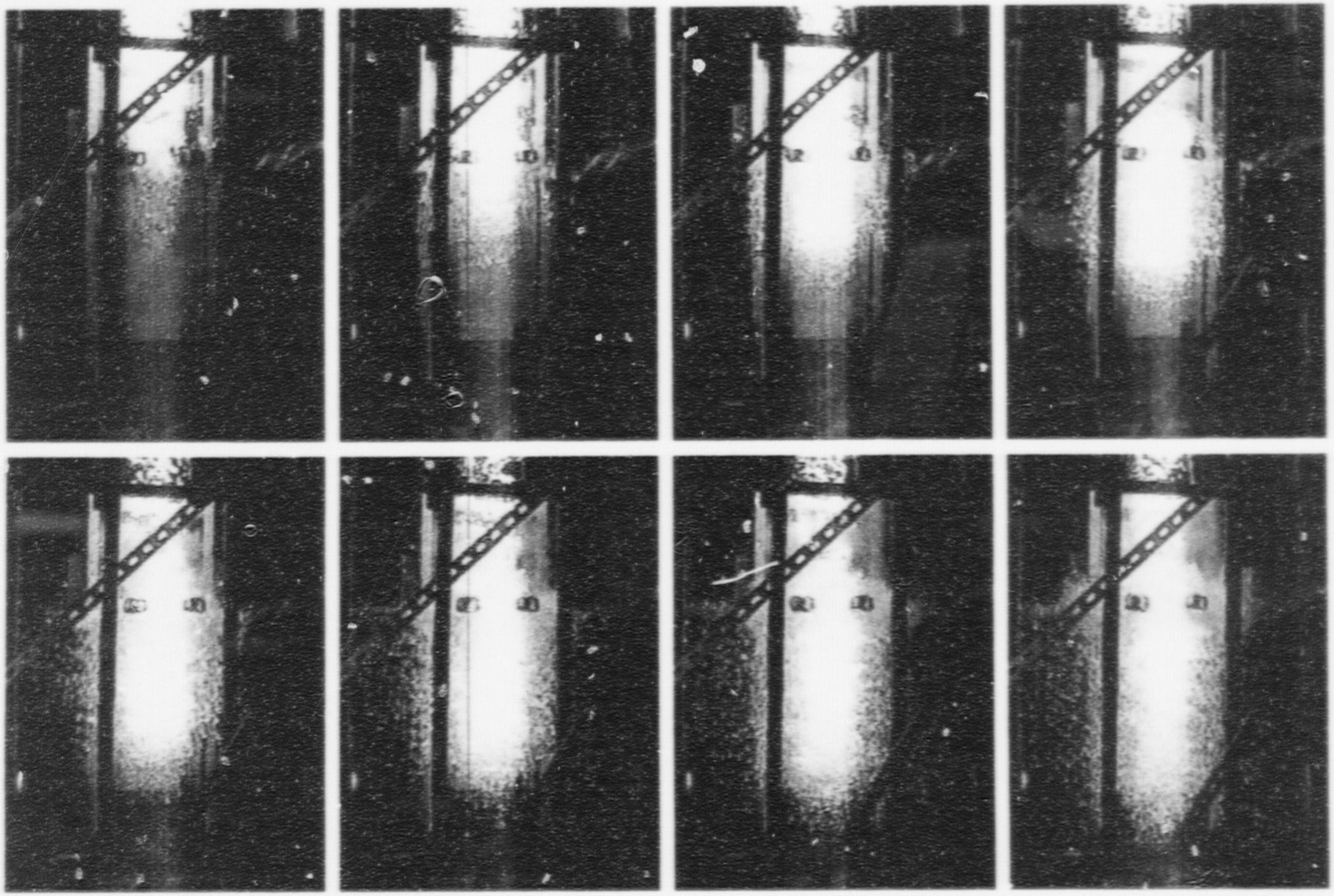

Figure 1(d). Video record of Run ZT14. The frames are at 100 ms intervals.

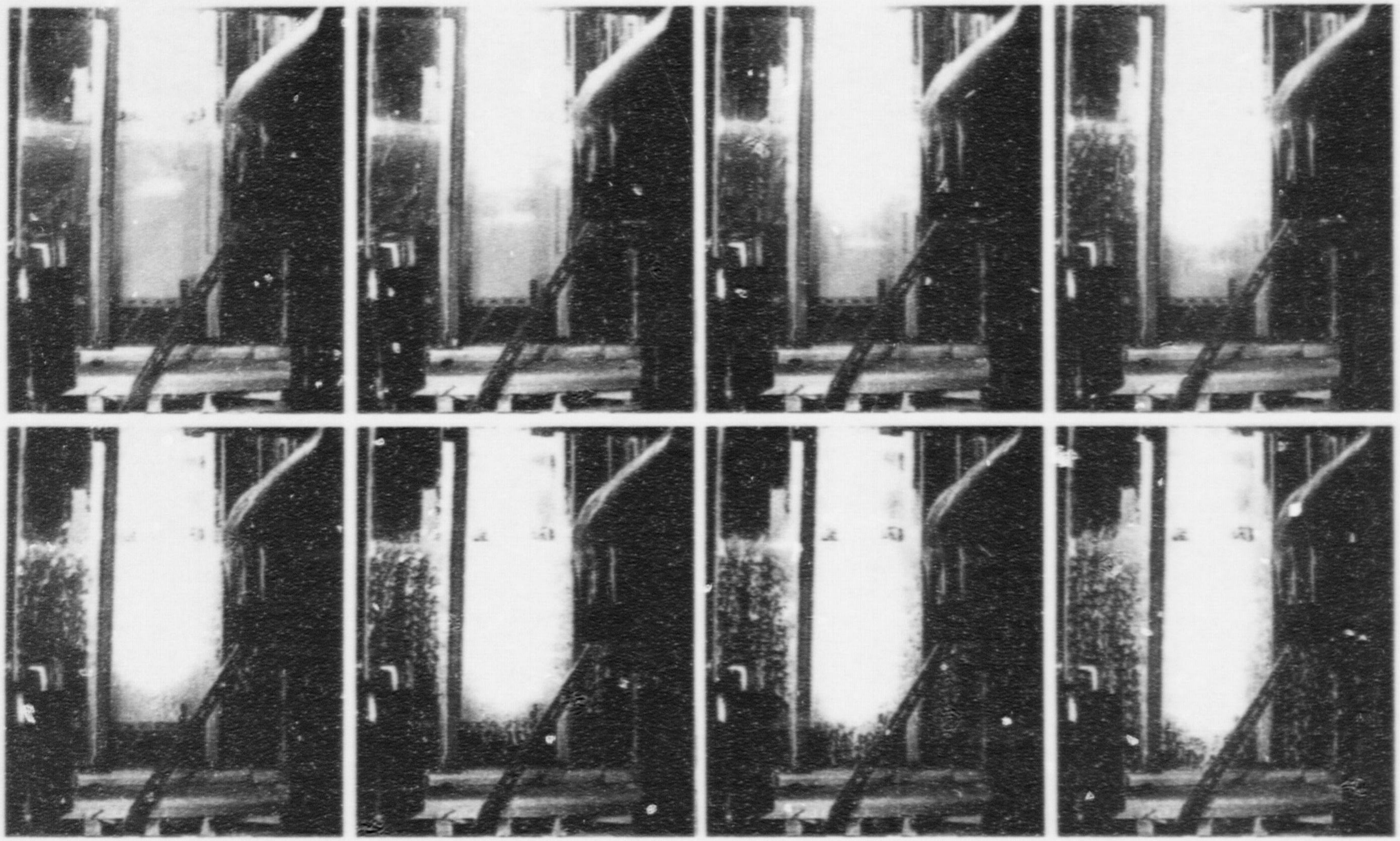

Figure 1(e). Video record of Run ZT15. The frames are at 100 ms intervals.

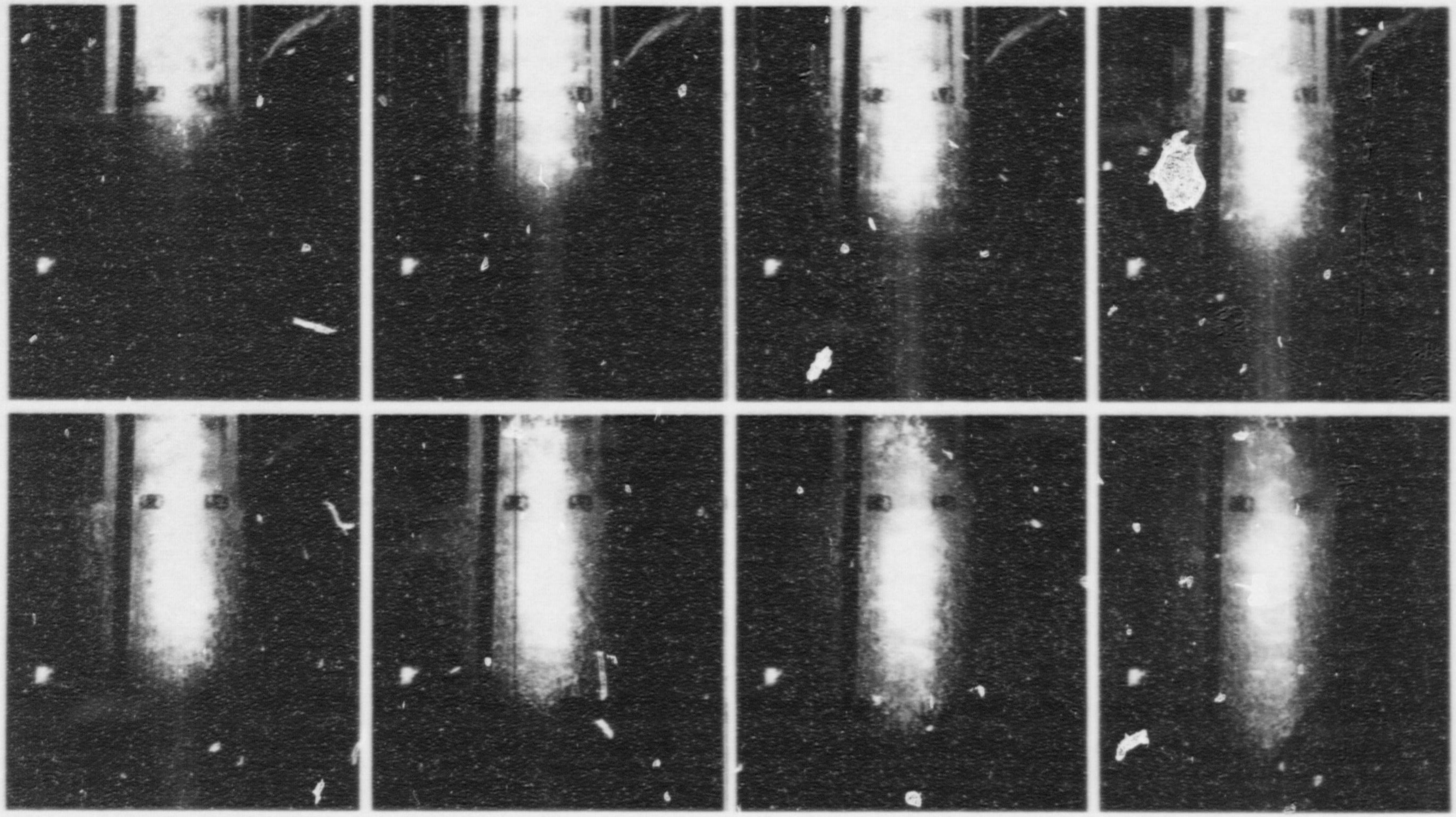

Figure 2(f). Video record of Run ZT16. The frames are at 100 ms intervals.

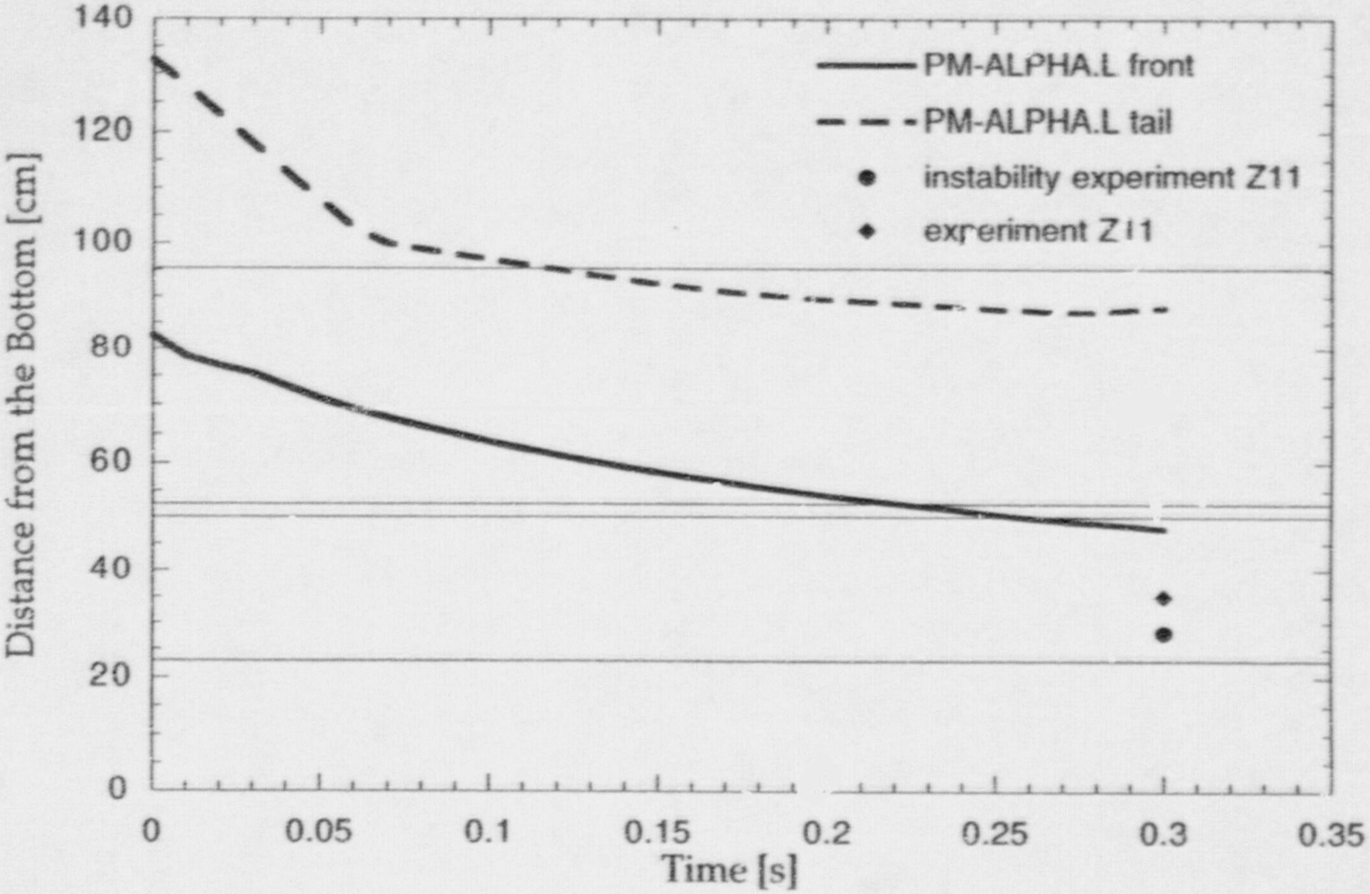

Figure 2(a). PM-ALPHA.L prediction of particle front and tail advancement against the experimental data in exper nt Z11. Also shown for reference to the X-ray shots are the positions of the films.

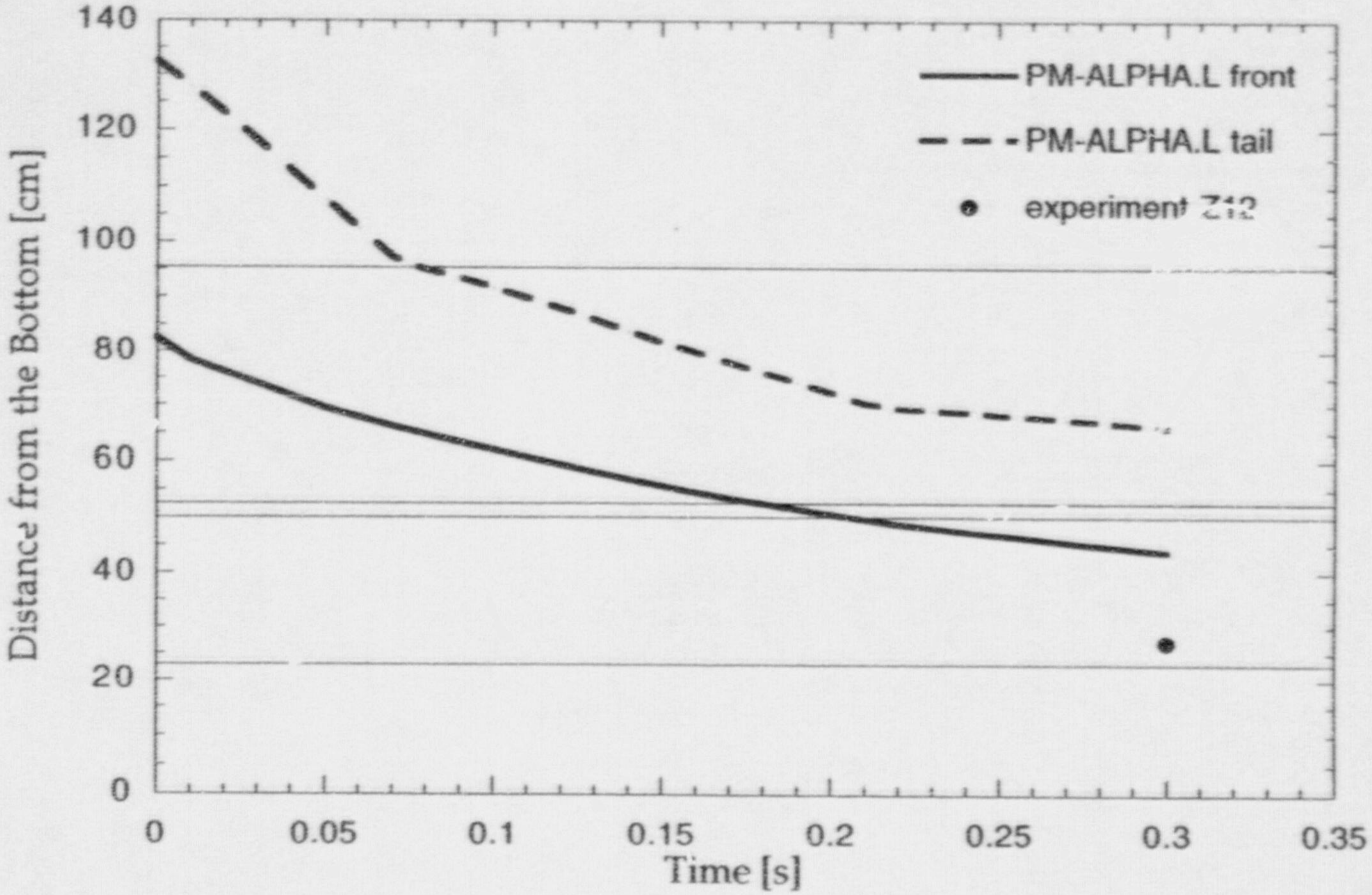

Figure 2(b). PM-ALPHA.L prediction of particle front and tail advancement against the experimental data in experiment Z12. Also shown for reference to the X-ray shots are the positions of the films.

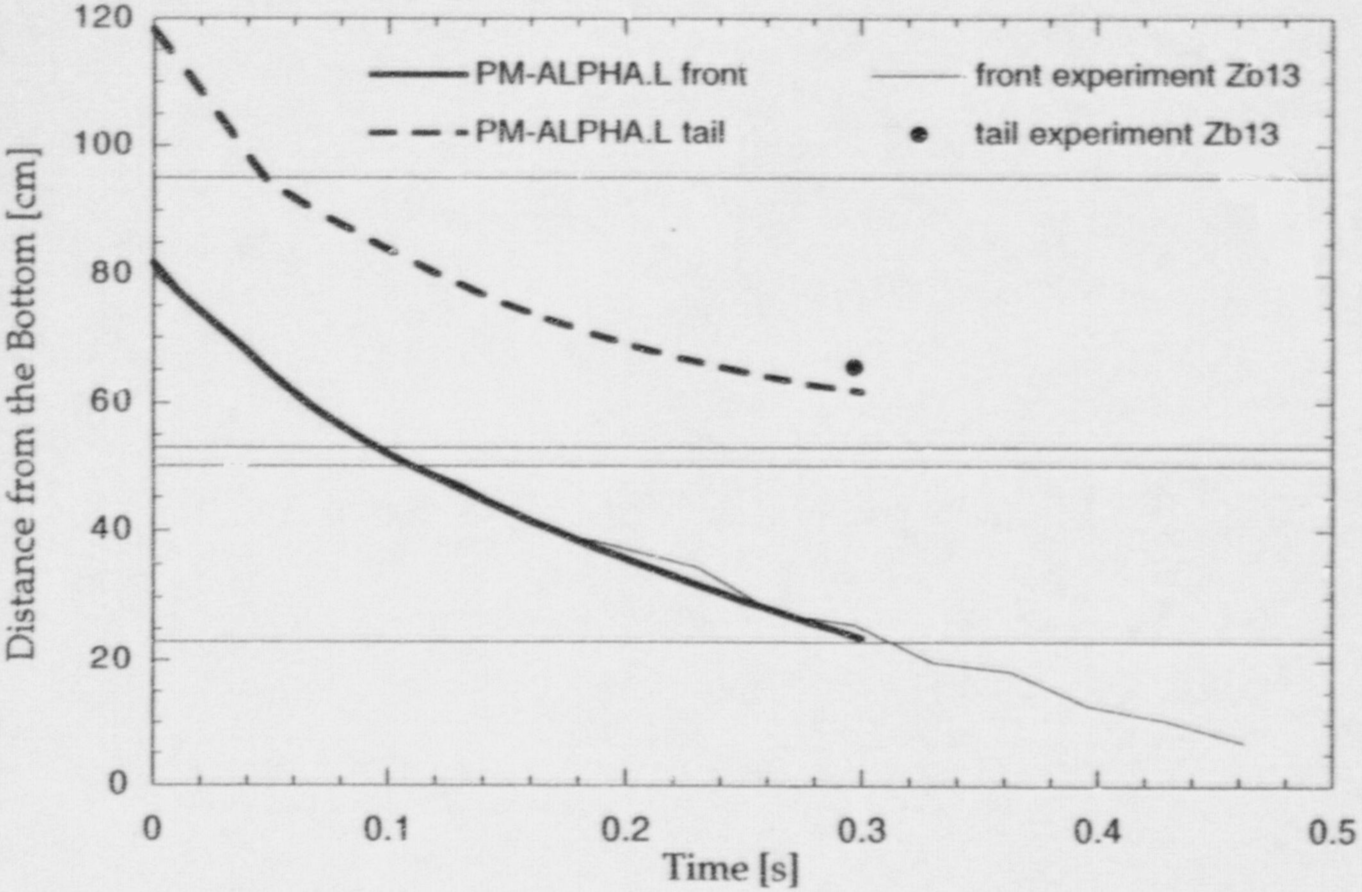

Figure 2(c). PM-ALPHA.L prediction of particle front and tail advancement against the experimental data in experiment Zb13. Also shown for reference to the X-ray shots are the positions of the films.

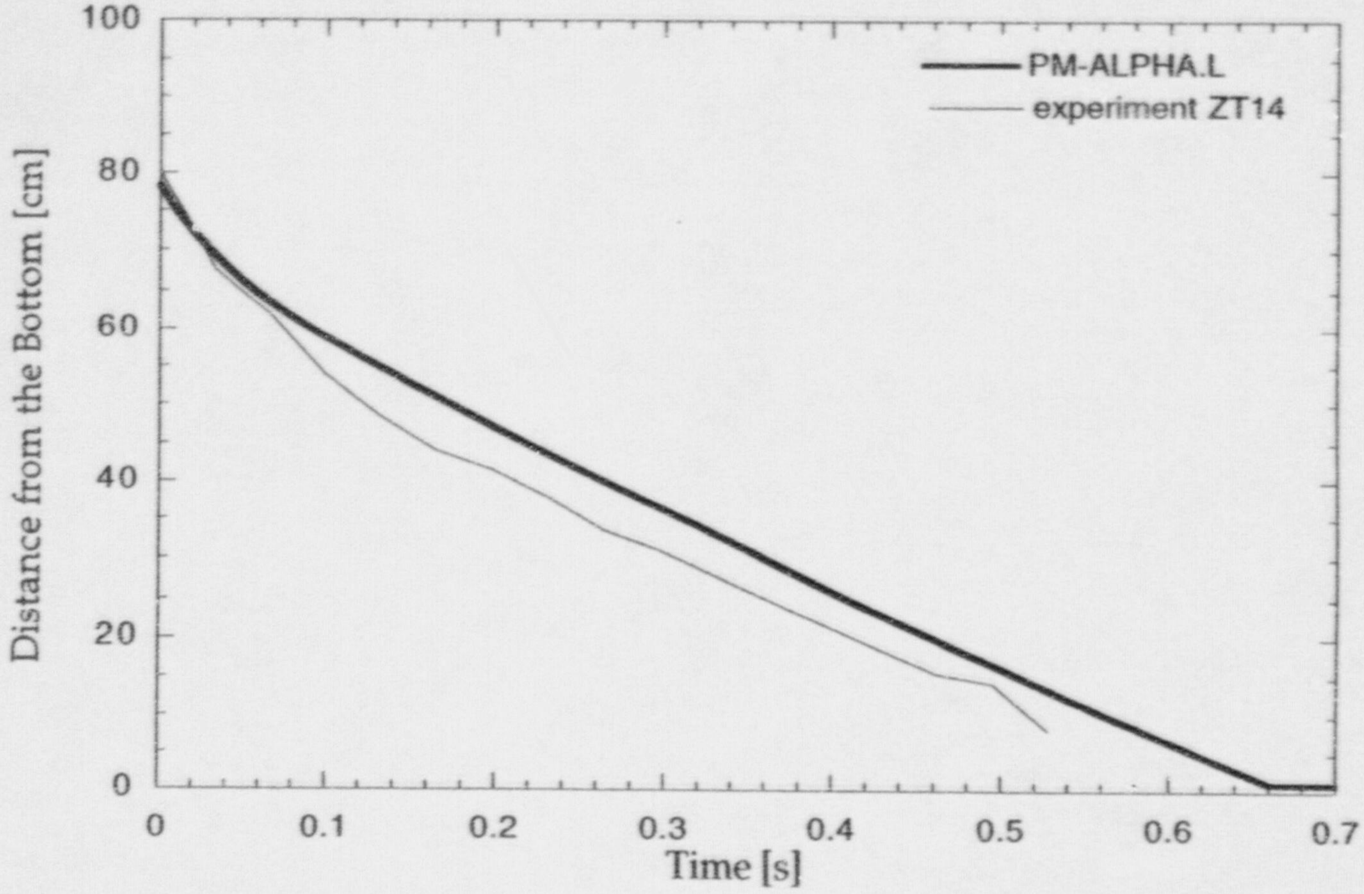

Figure 2(d). PM-ALPHA.L prediction of particle front and tail advancement against the experimental data in experiment ZT14. Also shown for reference to the X-ray shots are the positions of the films.

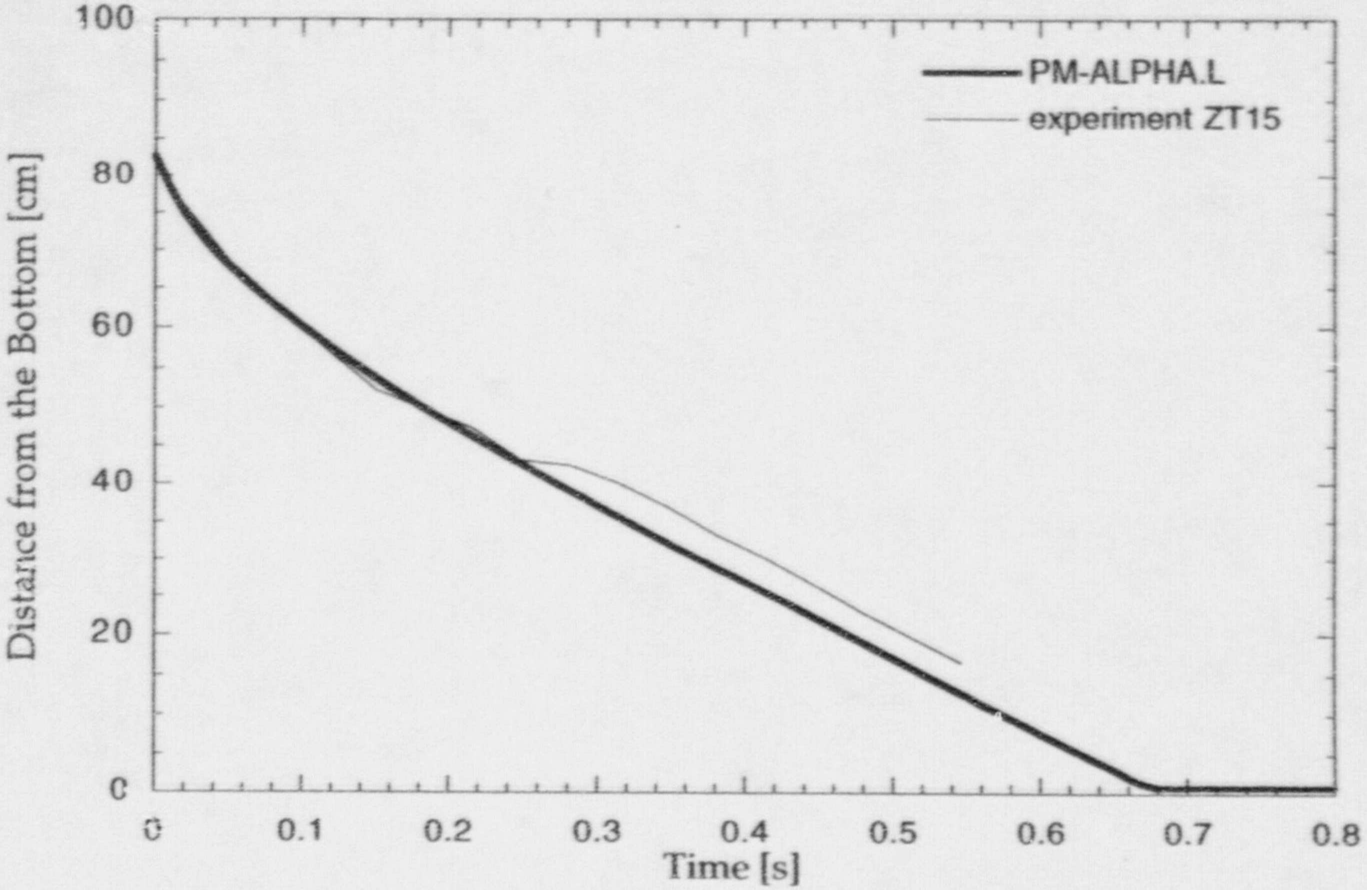

Figure 2(e). PM-ALPHA.L prediction of particle front and tail advancement against the experimental data in experiment ZT15. Also shown for reference to the X-ray shots are the positions of the films.

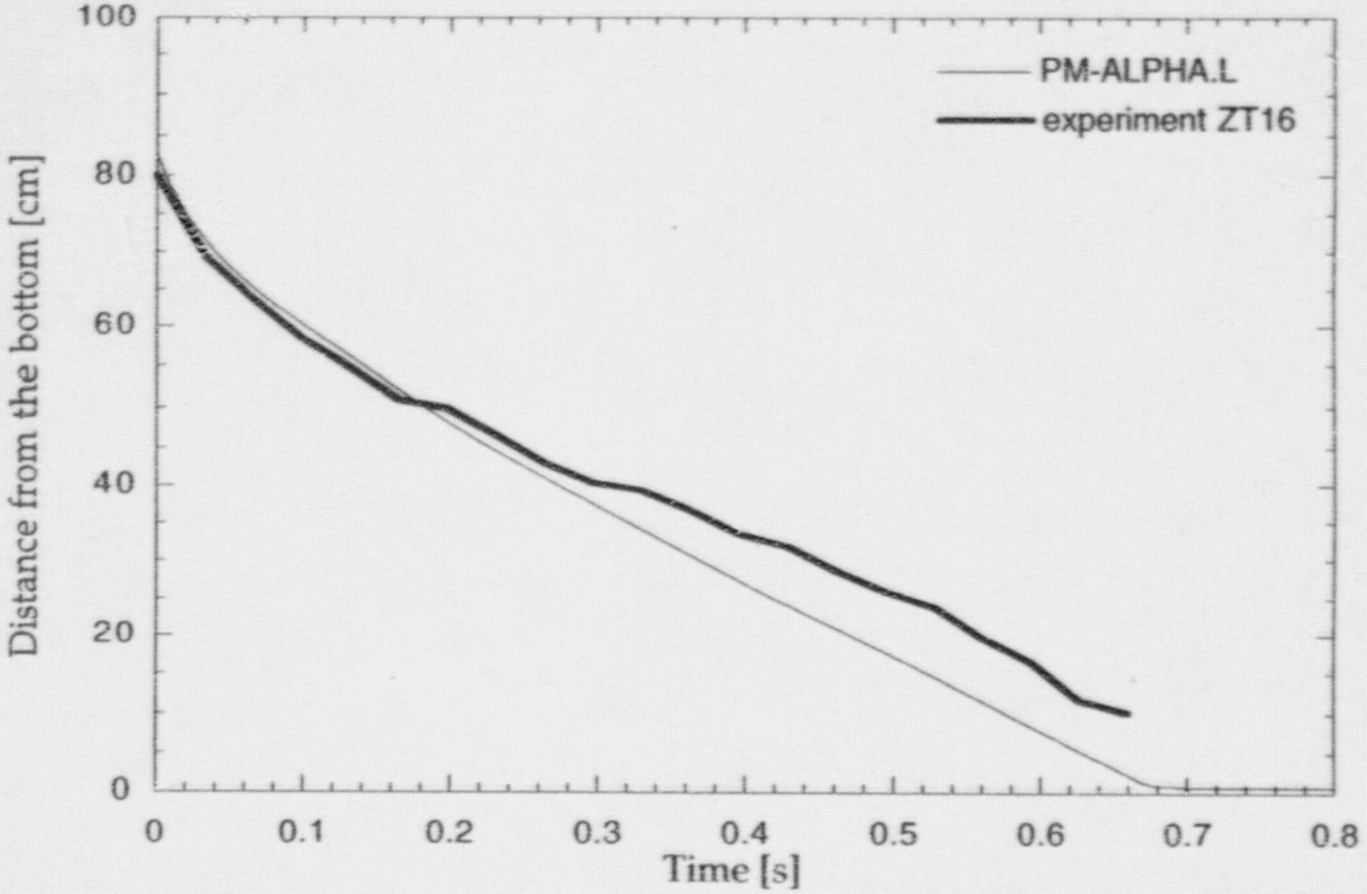

Figure 2(f). PM-ALPHA.L prediction of particle front and tail advancement against the experimental data in experiment ZT16. Also shown for reference to the X-ray shots are the positions of the films.

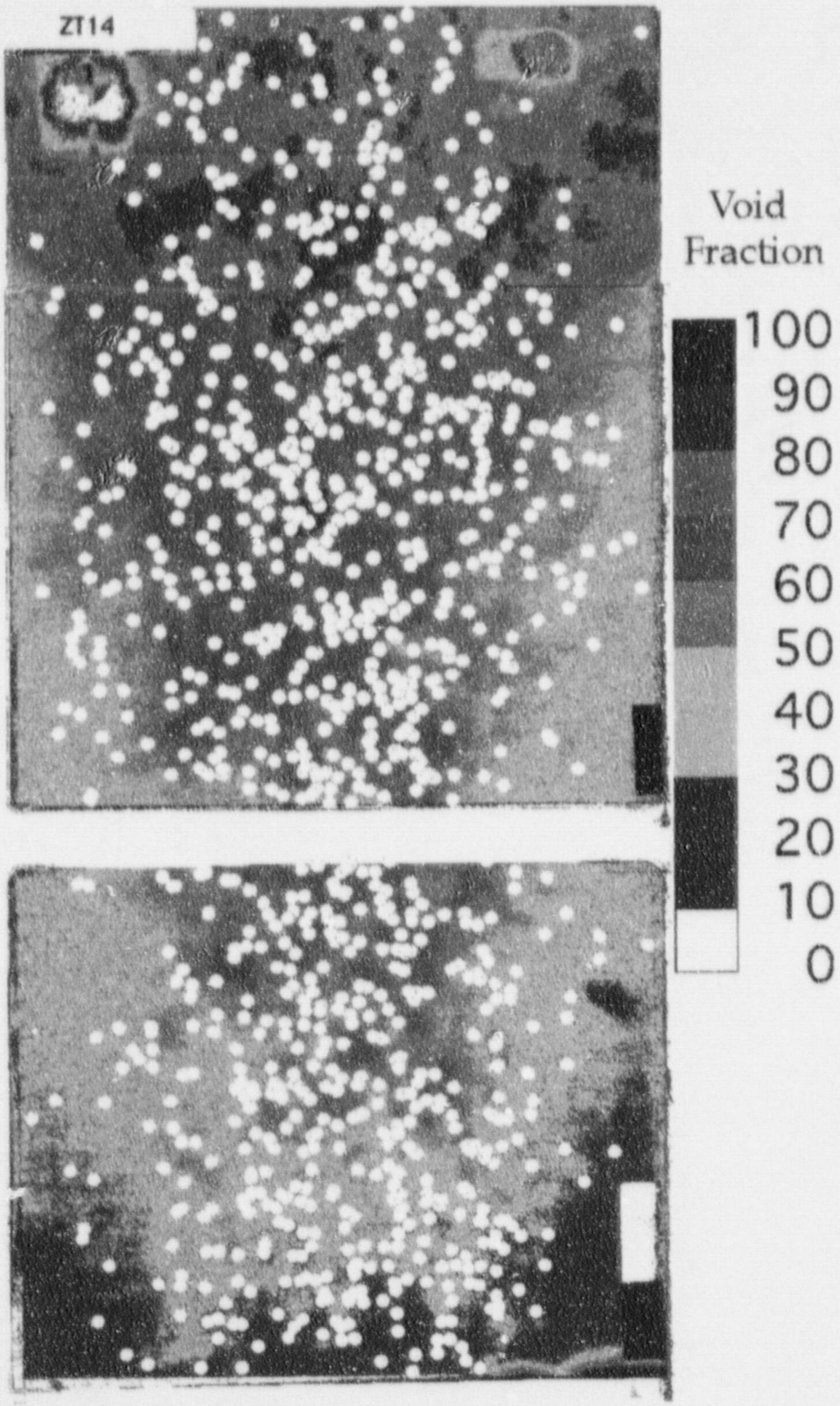

Figure 3(a). Digital reconstruction of the X-ray taken in Run ZT14.

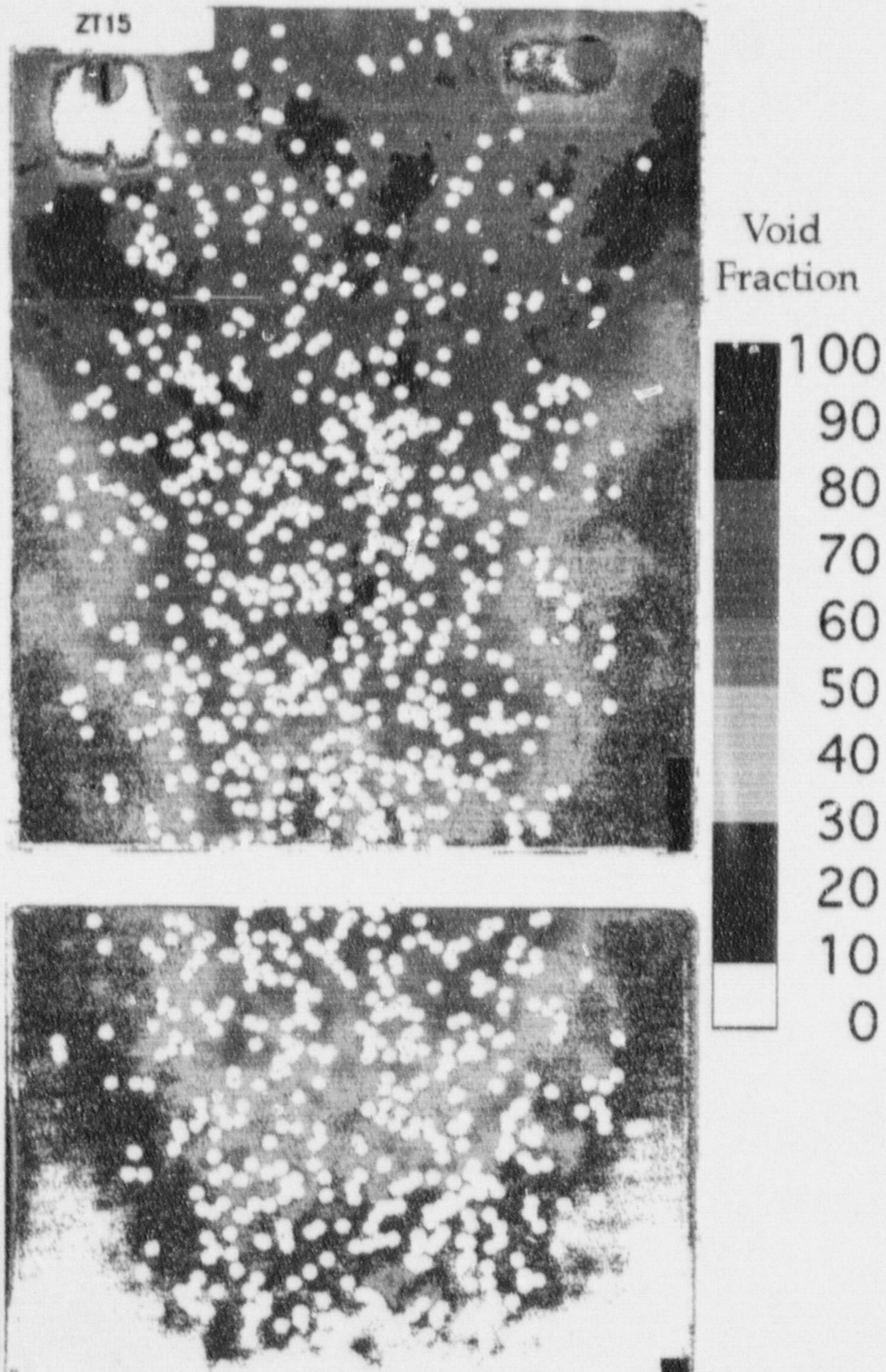

Figure 3(b). Digital reconstruction of the X-ray taken in Run ZT15.

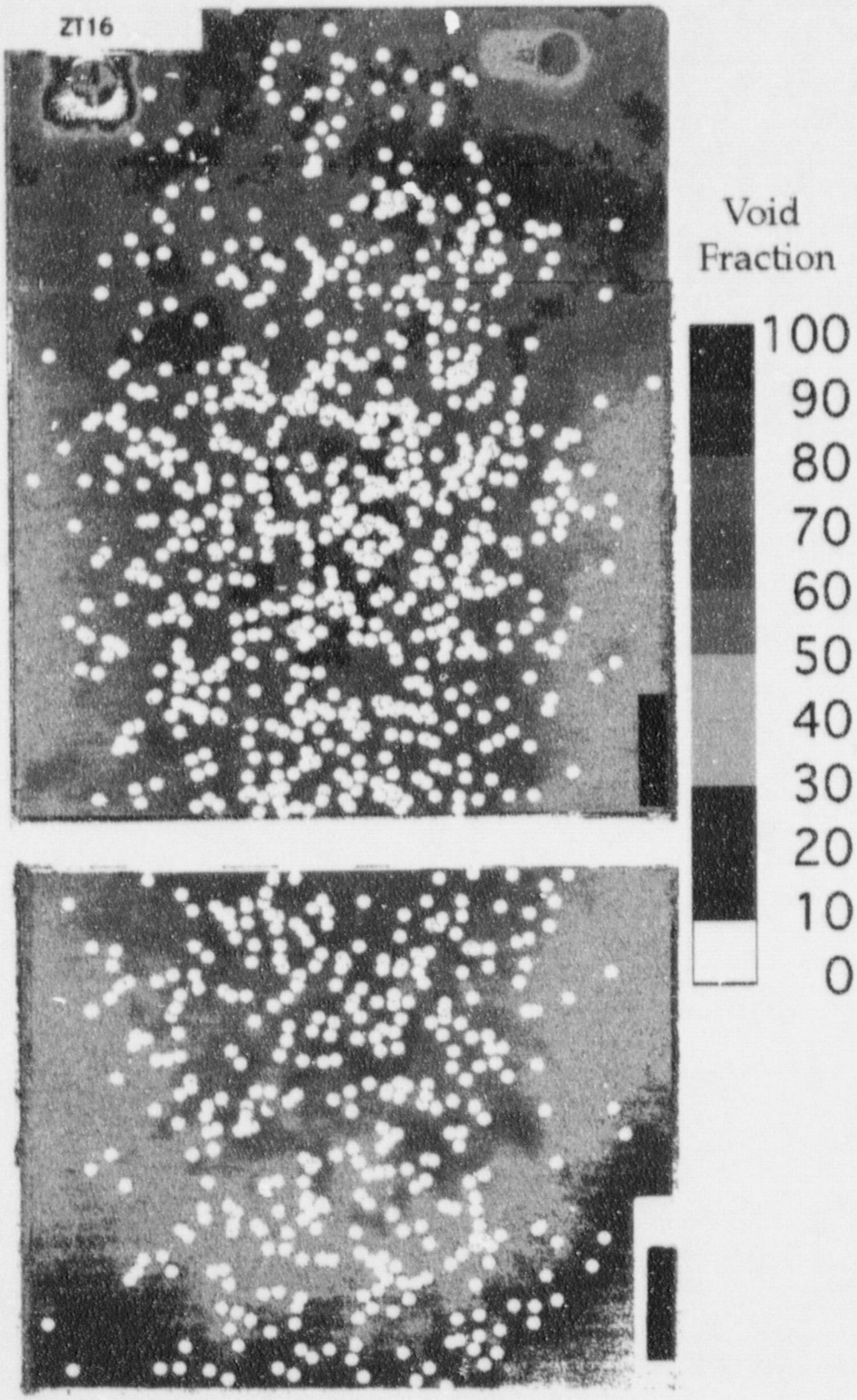

Figure 3(c). Digital reconstruction of the X-ray taken in Run ZT16.

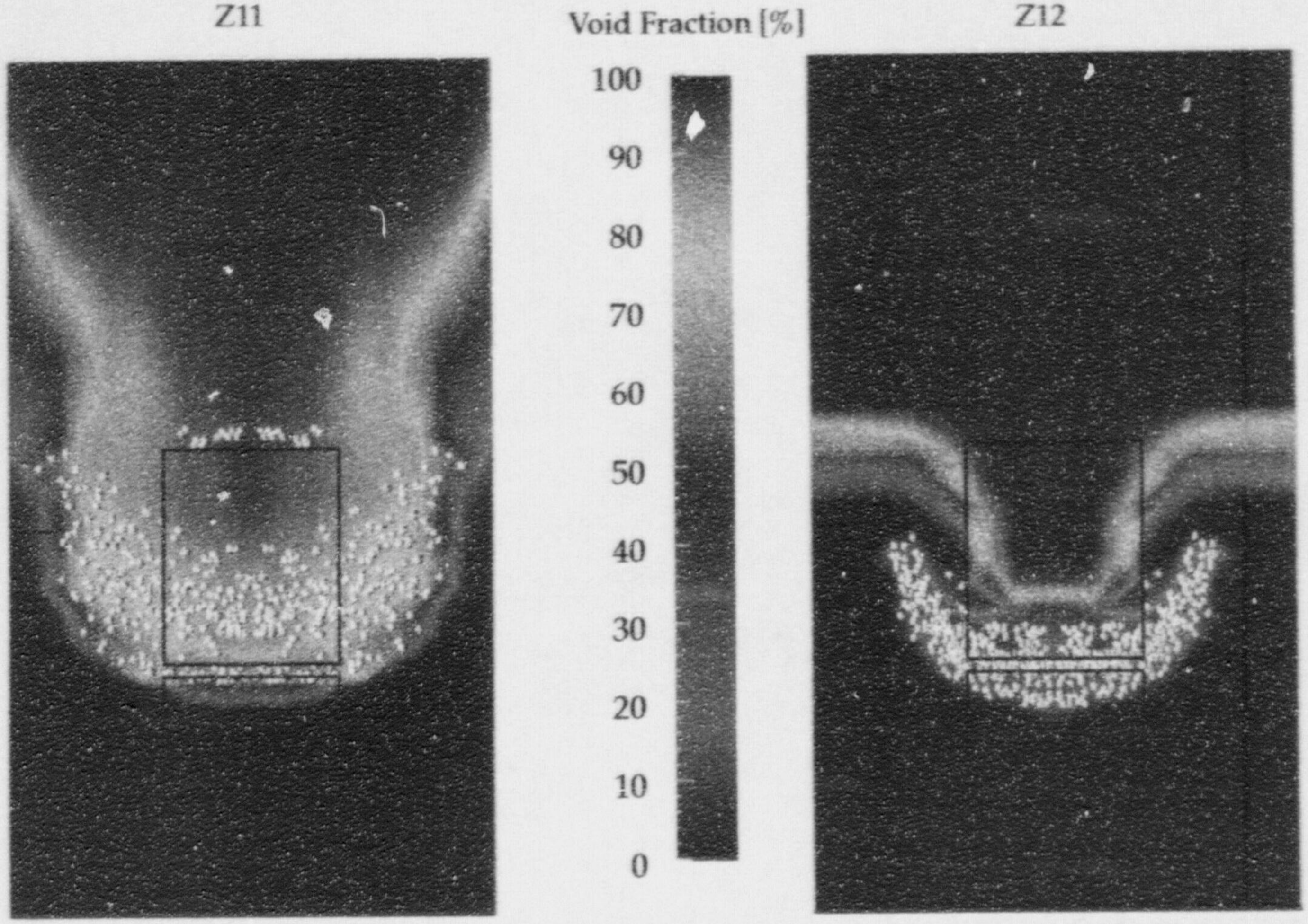

Figure 4. Frames from PM-ALPHA.L simulations of MAGICO-2000 Runs Z11 through ZT16, at the instant the X-ray shots were taken. The position of the X-ray films is also marked. The full simulations are shown in Figure 5.

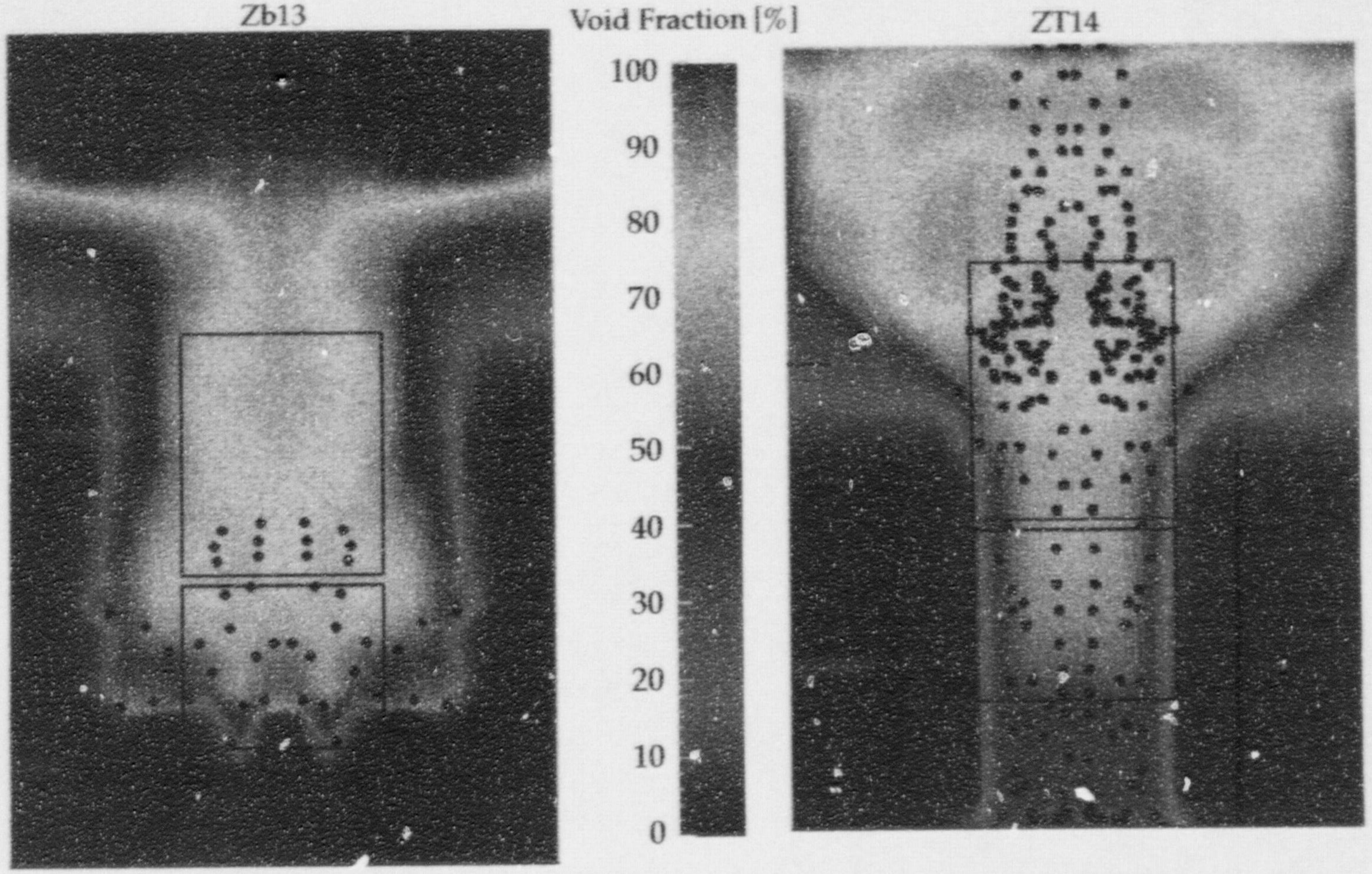

Figure 4. (Continued).

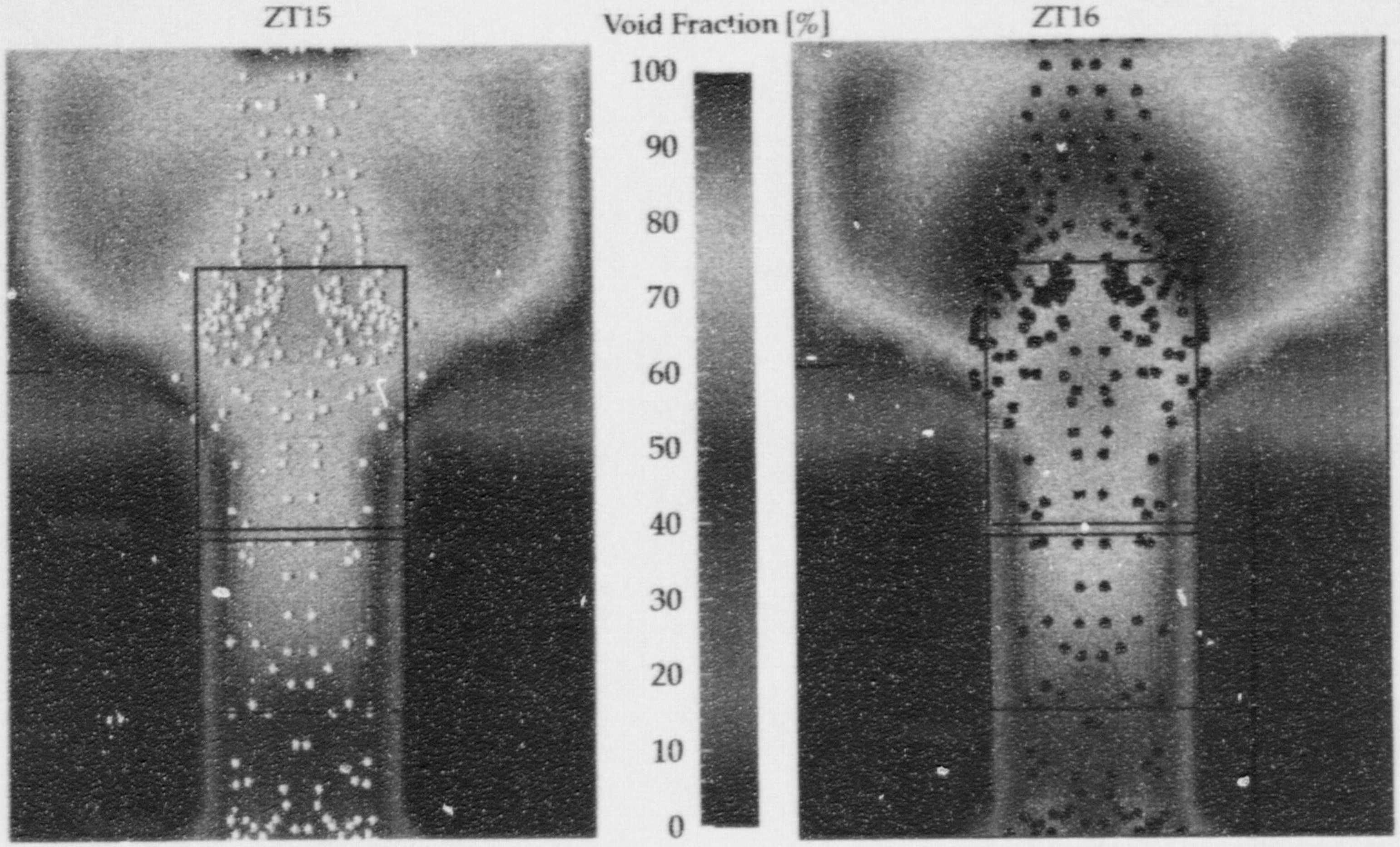

Figure 4. (Continued).

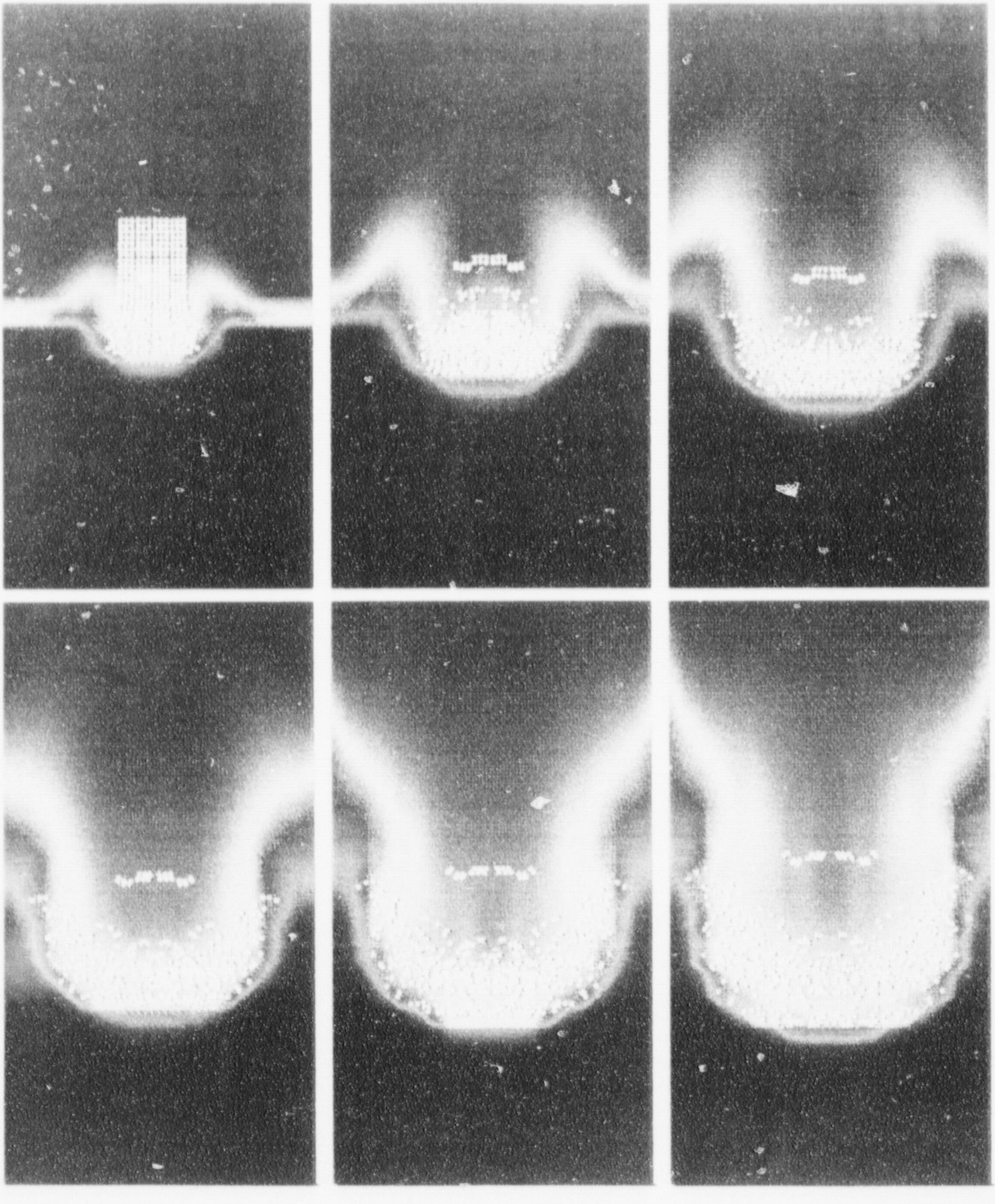

Figure 5(a). PM-ALPHA.L simulation of Run Z11. The frames shown are at 50 ms intervals. The void fraction scale is the same as in Figure 4.

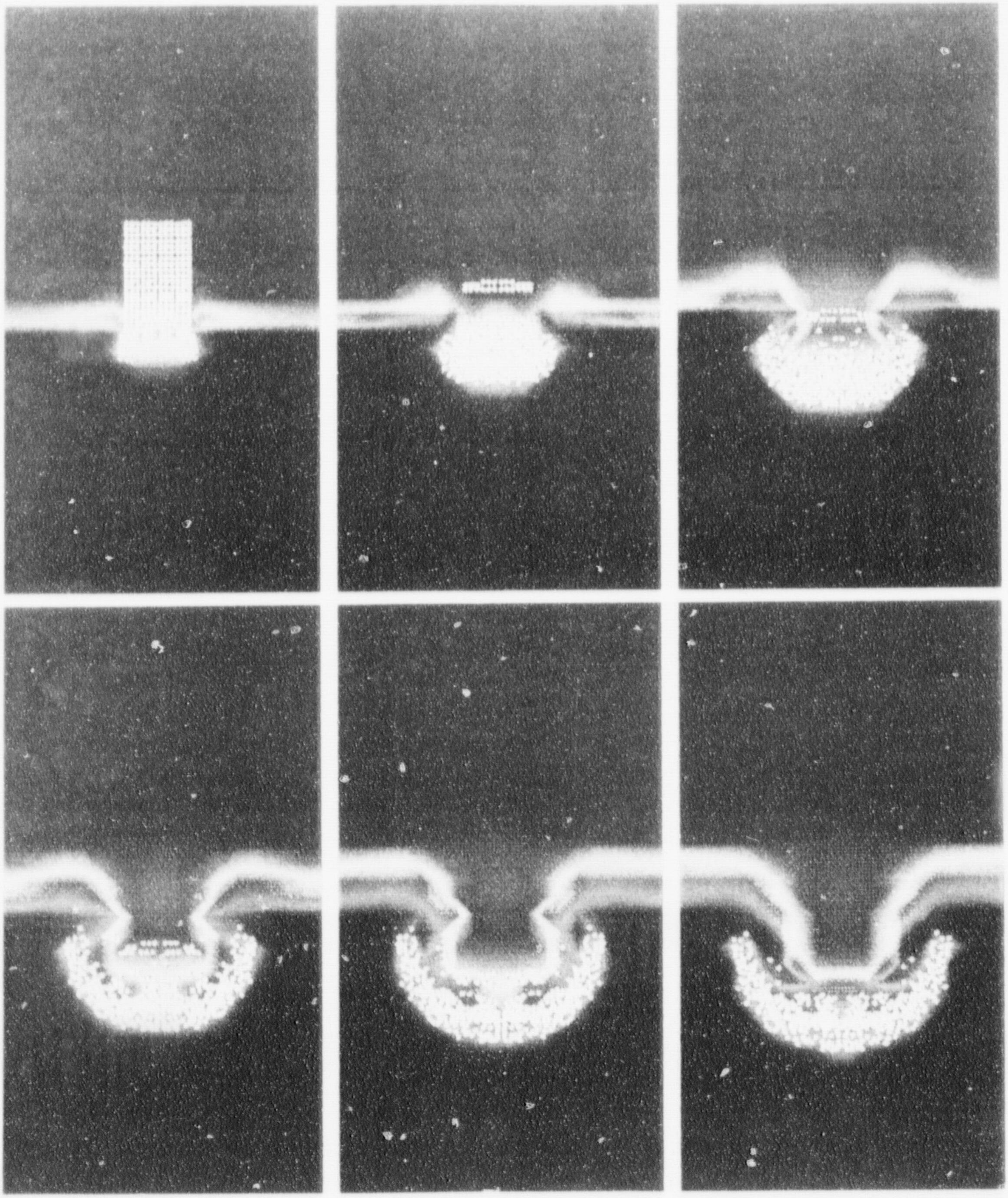

Figure 5(b). PM-ALPHA.L simulation of Run Z12. The frames shown are at 50 ms intervals. The void fraction scale is the same as in Figure 4.

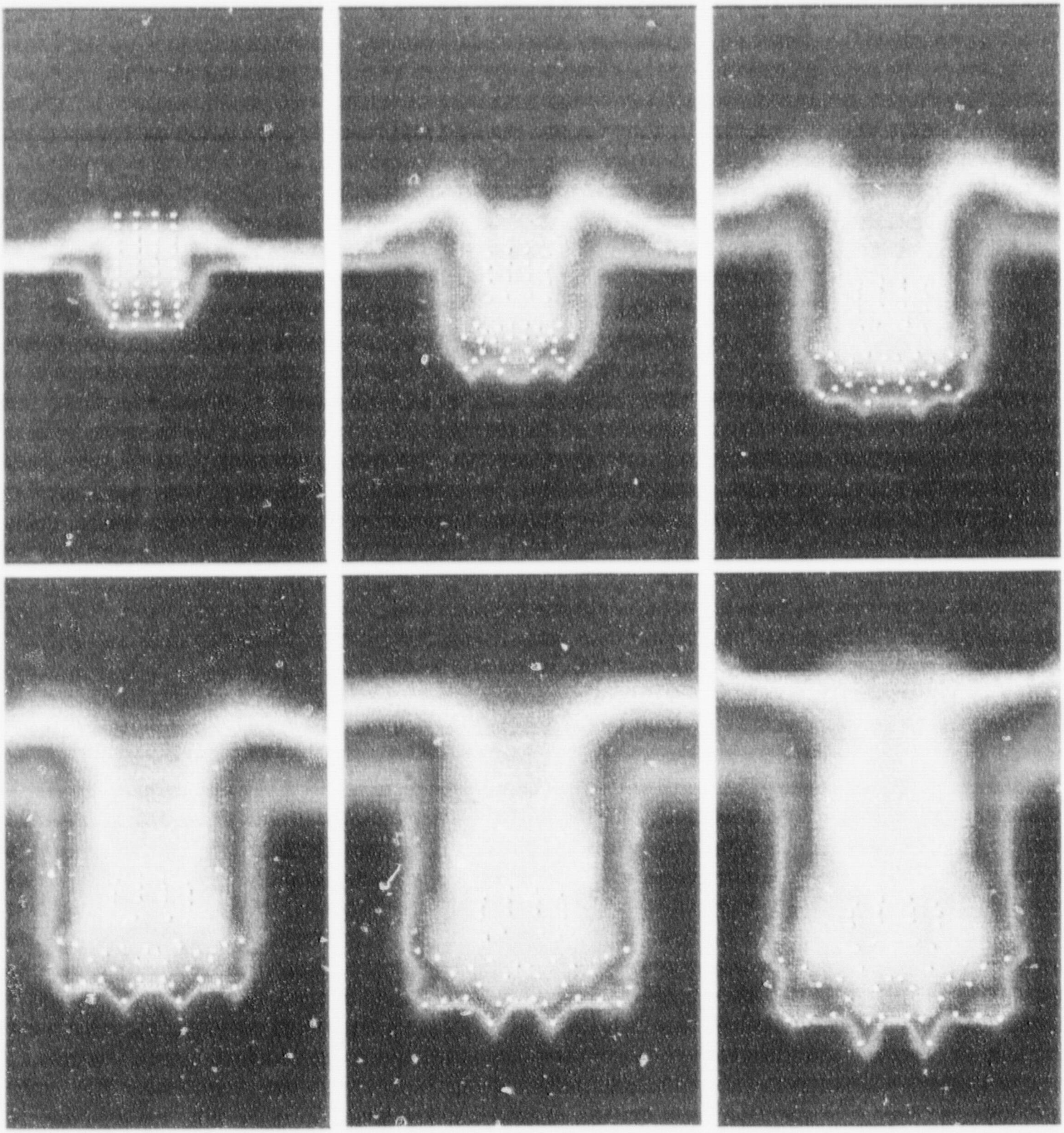

Figure 5(c). PM-ALPHA.L simulation of Run Zb13. The frames shown are at 50 ms intervals. The void fraction scale is the same as in Figure 4.

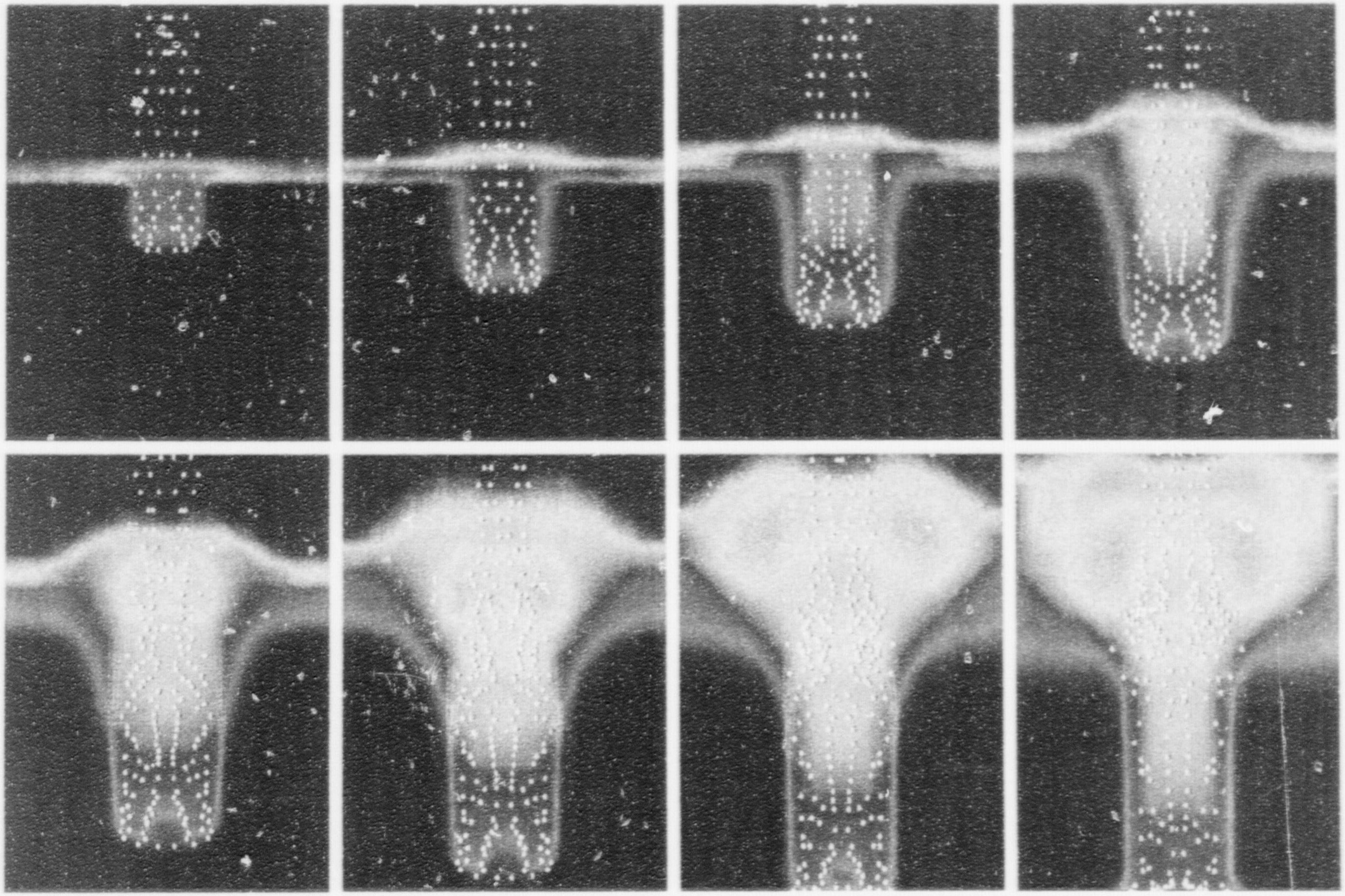

Figure 5(d). PM-ALPHA.L simulation of Run ZT14. The frames shown are at 100 ms intervals. The void fraction scale is the same as in Figure 4.

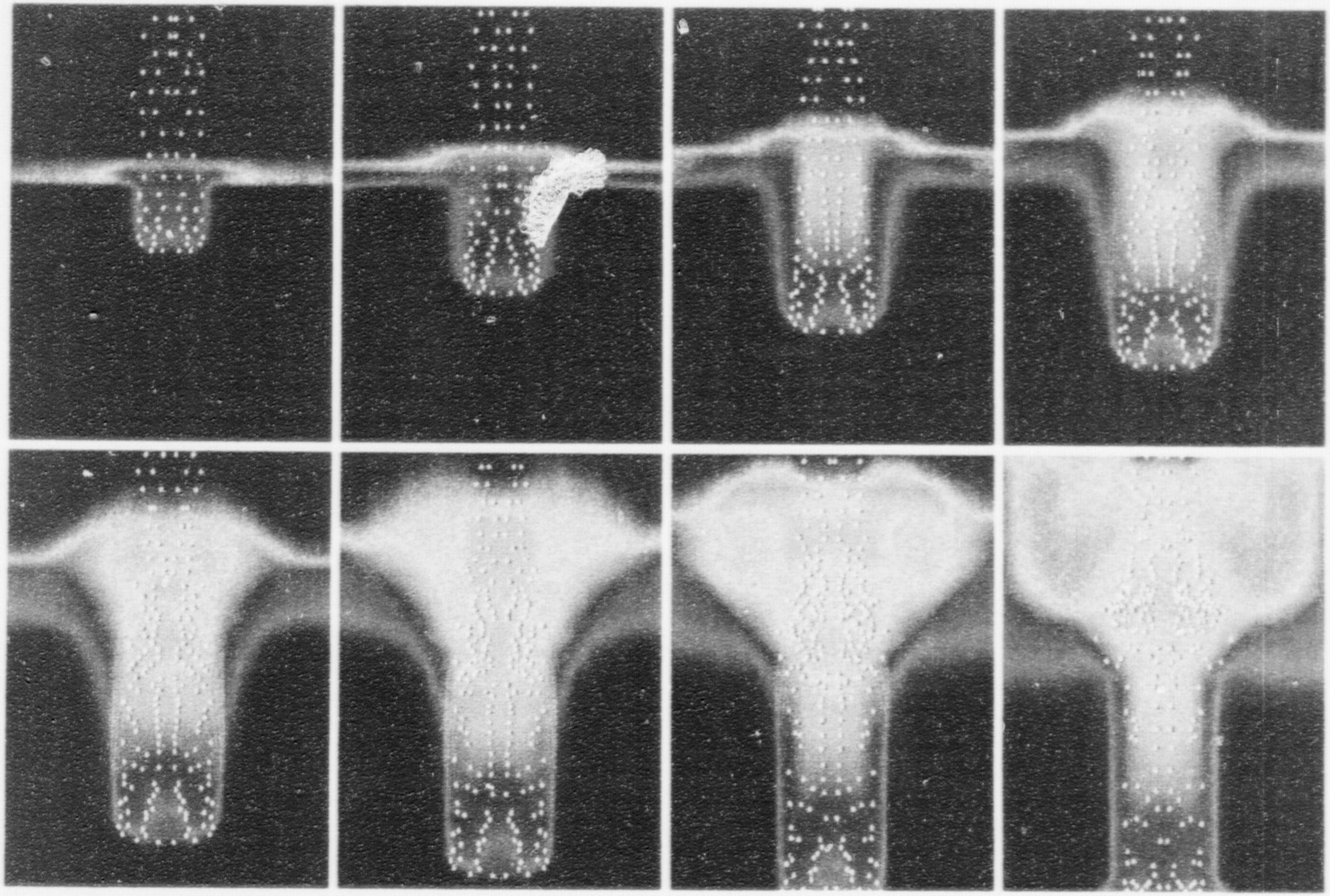

Figure 5(e). PM-ALPHA.L simulation of Run ZT15. The frames shown are at 100 ms intervals. The void fraction scale is the same as in Figure 4.

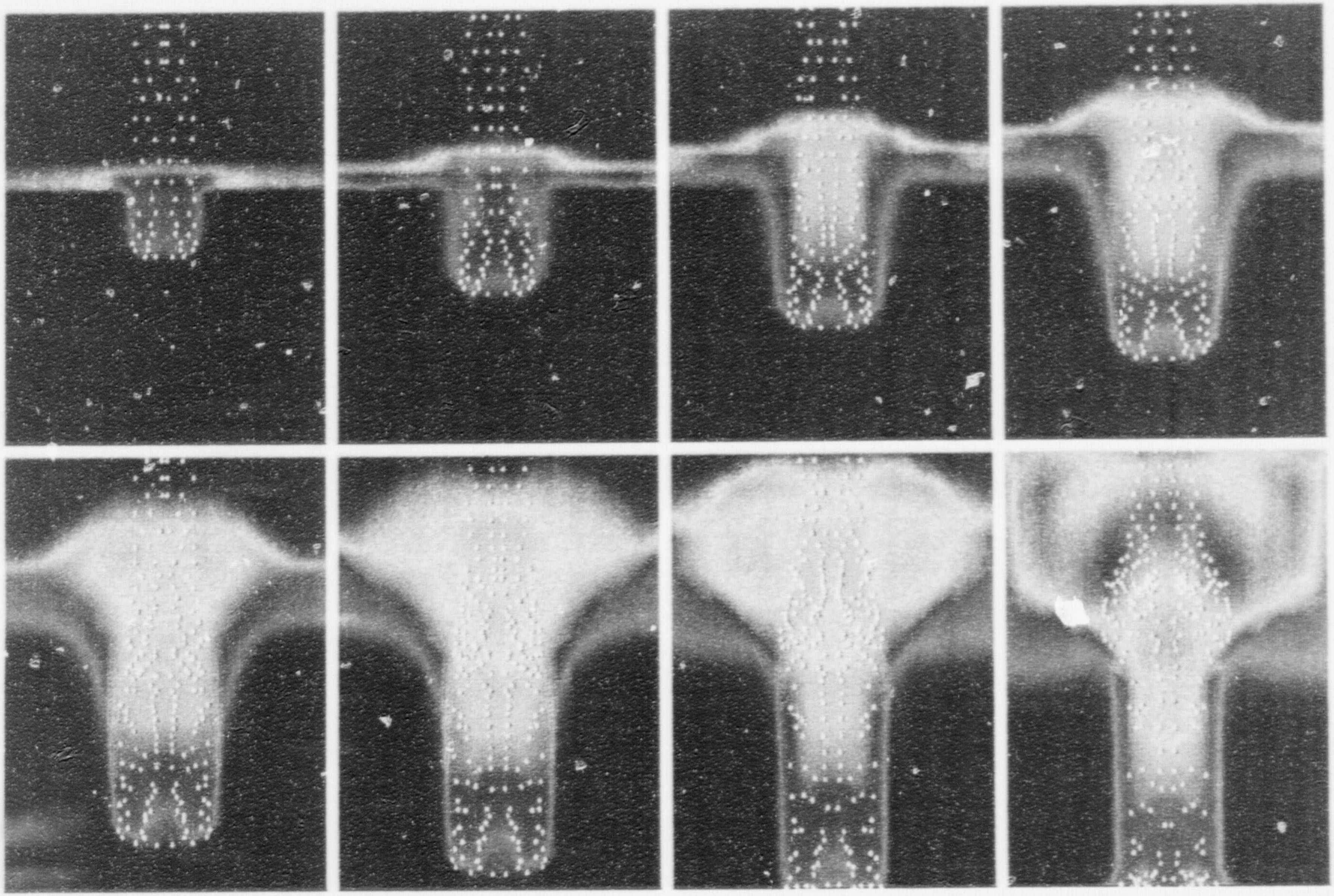

Figure 5(f). PM-ALPHA.L simulation of Run ZT16. The frames shown are at 100 ms intervals. The void fraction scale is the same as in Figure 4.

[[ADDENDUM TO SECTION 4.2.1 OF DOE/ID-10503]]

COMPARISON WITH KROTOS EXPERIMENTS

We reanalyze here the KROTOS test K38 with the premixing obtained from PM-ALPHA.L-3D. The calculation could be done more efficiently in 2D cylindrical symmetry, but we wanted to exercise here ESPROSE.m-3D, for the first time against an experiment. Additionally, the radiation transport model in PM-ALPHA.L-3D is a little better than in the 2D code. This, together with the shell-freezing model, also better treated than previously in the Eulerian code, would allow us to properly address the melt freezing issue that appeared to have arisen in our previous attempt.

It is recalled that in our first analysis the predicted explosions were stronger than measured in the experiment and that to obtain agreement we had to exclude some significant fraction of the fuel assumed to have frozen during premixing. At the time we had used the bulk freezing option in the Eulerian code, and larger-than-calculated freezing appeared plausible, in a more realistic shell-freezing mode.

It turns out that ESPROSE had given us the right hint — the melt volume fraction supplied to it was too high for the observed explosions. Actually, the problem was that we had used (in both premixing and explosion calculations), inadvertently, the test vessel diameter of the original KROTOS facility (like the one in test K28 which we had analyzed still earlier); that is, an area four times smaller than the actual one in test K38. As we will see below, even in a shell model, the quantity of melt frozen is negligible, and using the correct vessel diameter allows a completely consistent interpretation both for premixing (whatever limited information is available on it) and for the explosion. Another key point in this regard is that based on information made available to us during this review*, we corrected the emissivity of $A\ell_2O_3$ from the previously used value of 0.75, to a value of 0.35.

As previously, we have used a melt delivery rate of 1 kg/s, for a total quantity of 1.5 kg. The delivery opening was 3 cm, as in the experiment. The melt was taken to enter with a characteristic length scale of 1 cm, and further breakup was assumed to be negligible. This is consistent with what we found earlier (a breakup parameter of 50). Both results agree with the melt penetration rates, while any significant breakup produces a significantly lower penetration than found experimentally. The full subcooled boiling model (as in the PM-ALPHA.L analyses of MAGICO, FARO and QUEOS experiments) is utilized with a coefficient of 0.25.

---

* H.K. Fauske and R.E. Henry, Letter (concerning this review) to L.W. Deitrich, January 14, 1997.

The discretization chosen for the present calculation is illustrated in Figure 1. The dimensions preserve the cross-sectional area of the test section. The four inner cells make up a "core" region, while the outer 12 cells we call the "peripheral" region. This much coarser (than previously) discretization is quite adequate in the present Lagrangian treatment. Using planar symmetry only one-half of this domain is actually computed. The results are summarized in the following figures, together with available experimental data.

The advancement of the melt penetration front is shown in Figure 2. We can see that significant breakup ($\beta = 10$) would have slowed the melt down to a significant degree from that observed. The thermocouples exhibit a clearly eratic behavior, but this is not unexpected, since with such a high subcooling they must be subject to direct "hits" in order to feel the melt. Given the rather low area-averaged melt volume fraction, it is not at all surprising to have some delayed hits. This is clearly the case for the first thermocouple, so it is shown as an open circle. The remaining show a clear trend, if we also exclude the fourth thermocouple, again assuming a delayed hit. This is also shown as an open circle. That this is the proper trend is also supported by the independent determination of the two extremes (they make the two very reliable anchors in the data). One is the near surface thermocouple ($z \sim 100$ cm), where the melt arrives under free-fall. The other is at a position around the K3 transducer ($z \sim 55$ cm), where the explosion appears to have been triggered (spontaneously) at ~1 s. Further, it should be noted that this aspect of the computation is rather reliable, because it is not complicated by significant phase change effects (the average void fraction at the time of the explosion was only 2.6%).

Selected frames to visualize the PM-ALPHA.L-3D results are collected in Figure 3. Again, for clarity, each particle shown represents a "cluster" of particles. We can see that due to the high subcooling, short times, and relatively low melt plunging velocity (absence of strong breakup), the premixing proceeds rather quietly, with imperseptible void formation. More specific quantative representations of these results are shown in Figures 4 and 5. In particular, in Figure 5 we see that the melt remains mostly confined in the core region, where it reaches local volume fractions of ~4%. In Figure 4, we see that the cross-sectional-average fuel fraction reaches only ~2%. Also in Figure 4, we see that the void fraction remains at nearly zero, except that at around trigger time it reaches locally a peak value of ~5%. It may be that this rather sudden growth and collapse of this void that produced the trigger event (we have seen this kind of behavior in previous calculations also). At the front we also see a small amount of numerical diffusion in the void. This is expected, because the Eulerian treatment of the coolant was not adequately compensated for by the rather coarse nodalization used in this calculation.

The premixing result at 1 s was triggered in ESPROSE.m-3D, by releasing the pressure from the core cells at the elevation of K3 ($z = 55$ cm), assumed to be saturated with 1% vapor, at pressures of 100 or 200 bar (to check the effect of trigger strength). Calculations were carried out for two values of the entrainment parameter, the 7 we normally use, and a somewhat lower value of 5 to test sensitivity. The results are summarized in Figures 6, 7 and 8.

First, we note that the effect of the trigger pressure is negligible (Figure 6). The energetics (i.e., impulses) are reasonably bounded by the calculations using the two entrainment factors (Figures 7 and 8). The pressure pulse shapes and speeds are also reasonable when viewed in relation to the experimental data. While examining such results one should keep in mind that initial void fraction and melt fraction distribution, and length scales, are only estimates (from the premixing calculations), and these can affect the detailed structure of pressure pulses.

Finally, it is interesting to note that although there is no melt in the lower ~1/2 of the tube the impulse obtained therein is significantly larger than in the upper region. The dynamics here involve the explosion propagating upwards (K3 → K4 → K5), while at the same time pressures try to vent downward (K3 → K2 → K1 → K0). Not containing any significant compressible volume, this lower part pressurizes, and even more so as this pressure wave reflects from the bottom, rigid, surface.

Only the trigger area (K3) seems to be underpredicted (in the $f_e = 7$ case) and this may be due to overestimating the local void fraction from the premixing calculation. Note that even in the $f_e = 5$ case the early portion of the calculated transient in this location is weak, and that once the explosion gets going, the pressures are actually overpredicted in this case. On this basis we still think the $f_e \sim 7$ value is appropriate. We see that the KROTOS experiments can go a long way toward providing a verification base. The next step would be for them to provide also the local void fraction distribution at the time of trigger.

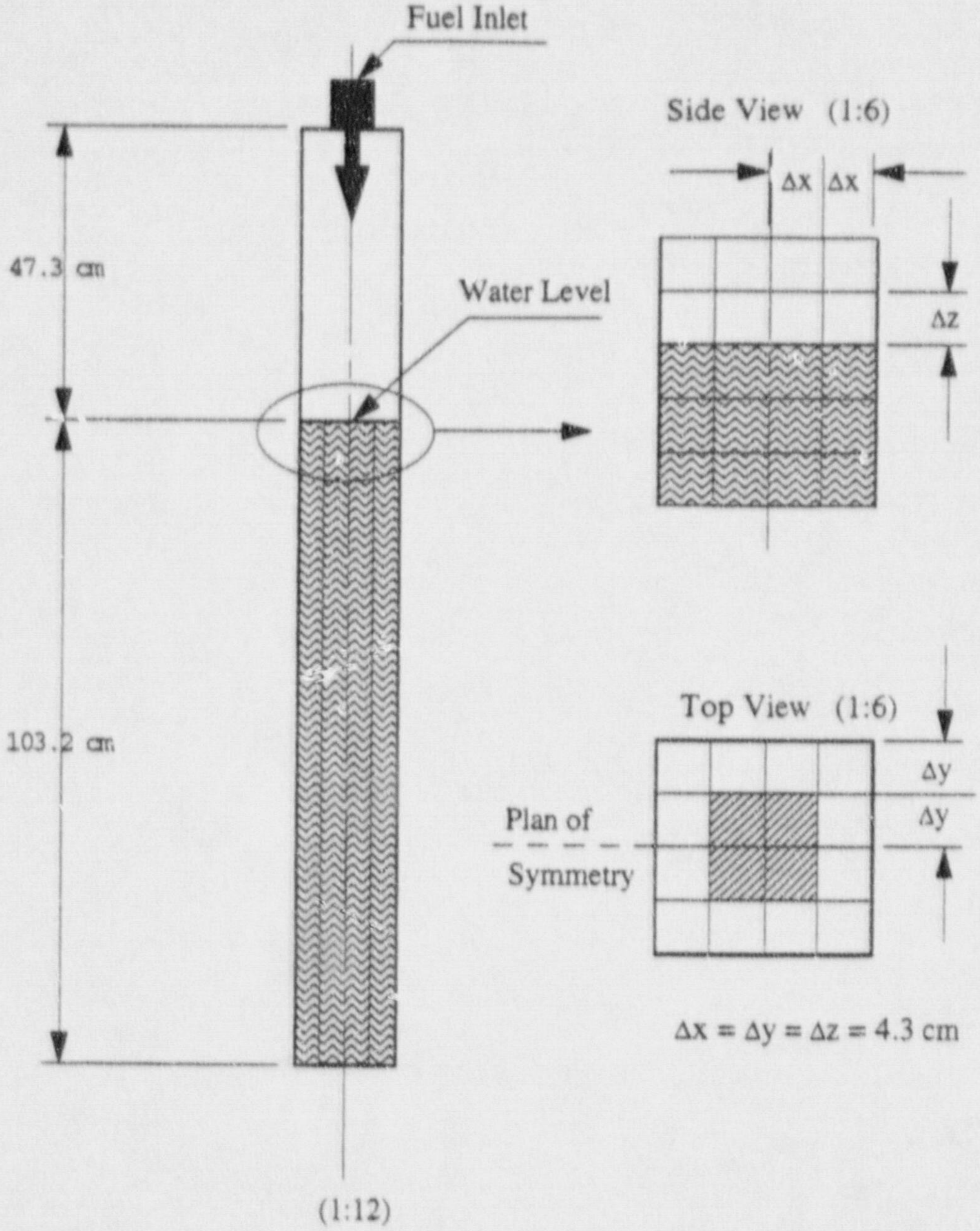

Figure 1. The discretization of the KROTOS vessel used in PM-ALPHA.L-3D, and ESPROSE.m-3D. Tne cross-sectional area is preserved.

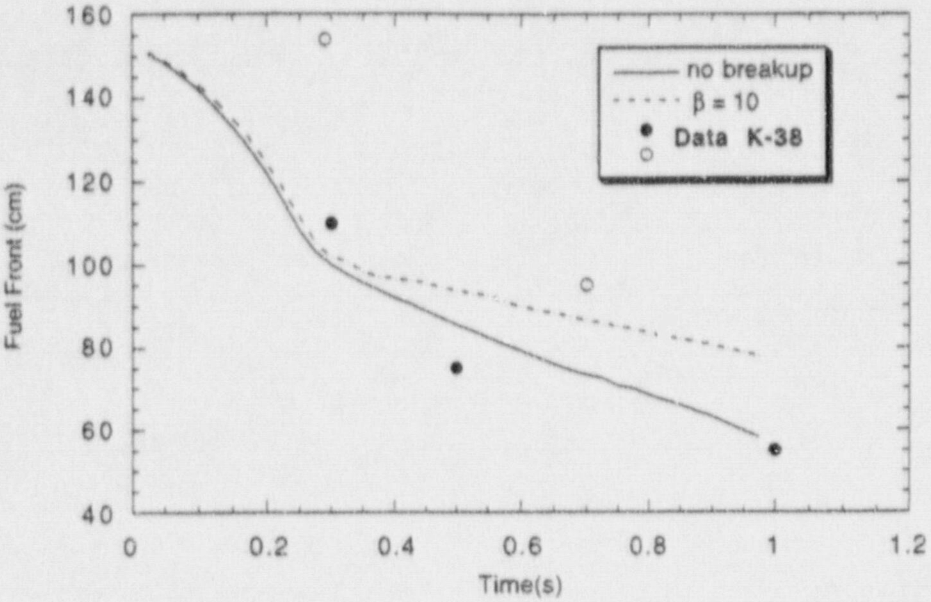

Figure 2. The front advancement predicted by PM-ALPHA against thermocouple "indications" of the front in test K38. Open circles probably indicate delayed "hits".

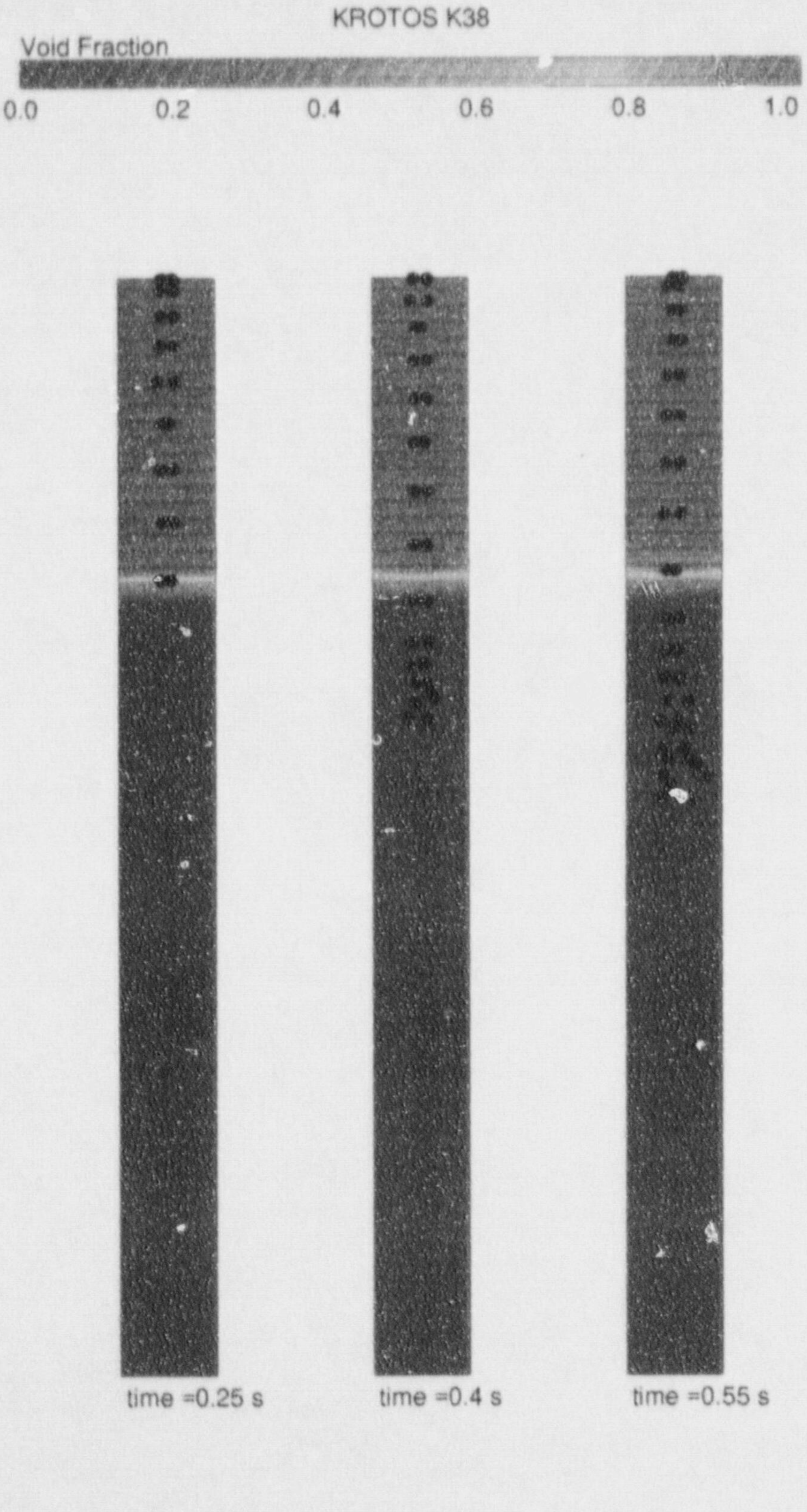

Figure 3. Premixing in KROTOS test K38 as predicted by PM-ALPHA.L-3D. The particles shown are "clusters" each representing about 5 real particles. The figure shows all particles projected on the broad face of the 2 x 4 cross-section of the flow domain (the other half is not shown).

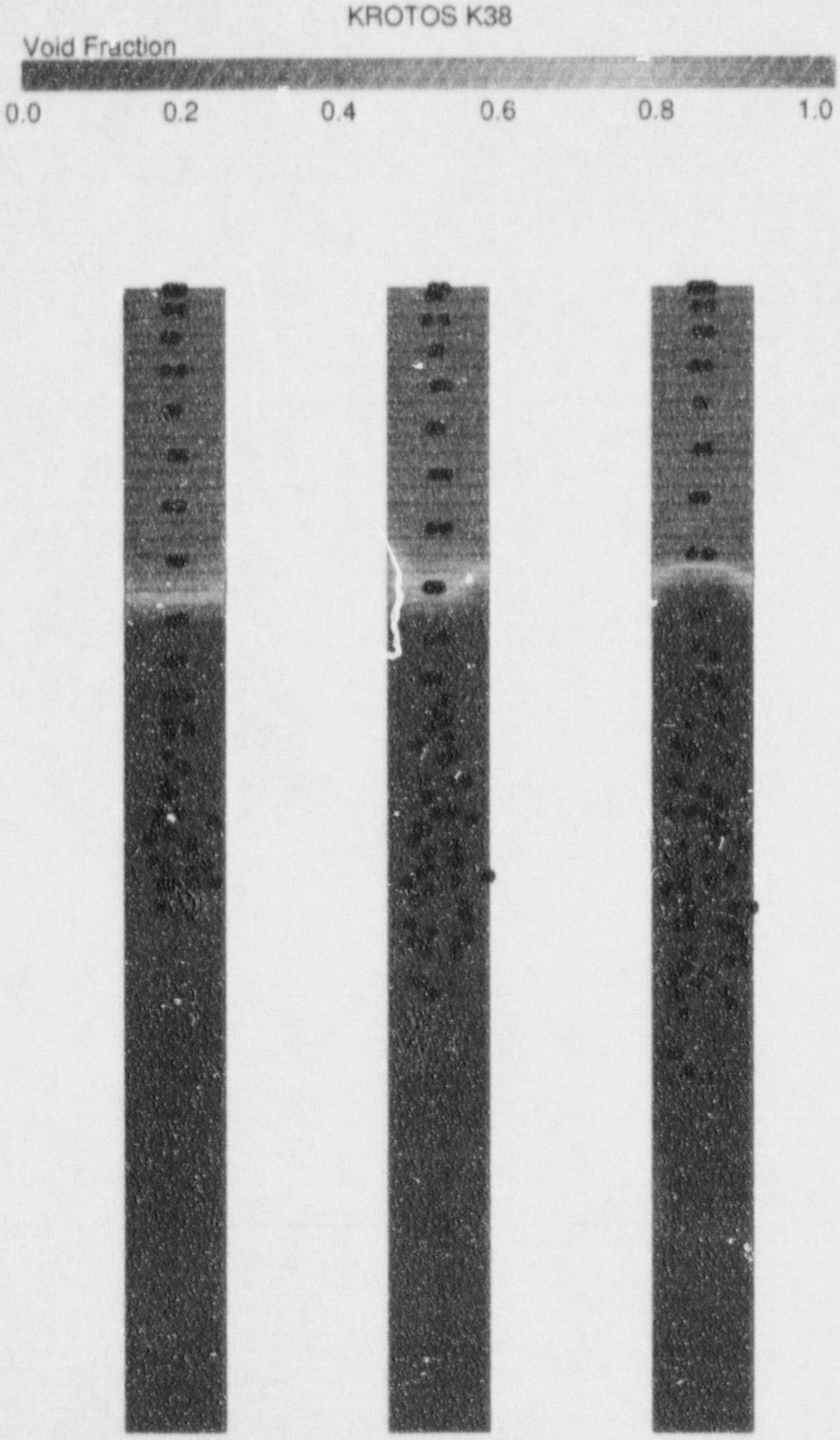

time =0.7 s time =0.85 s time =1 s

Figure 3. (Continued).

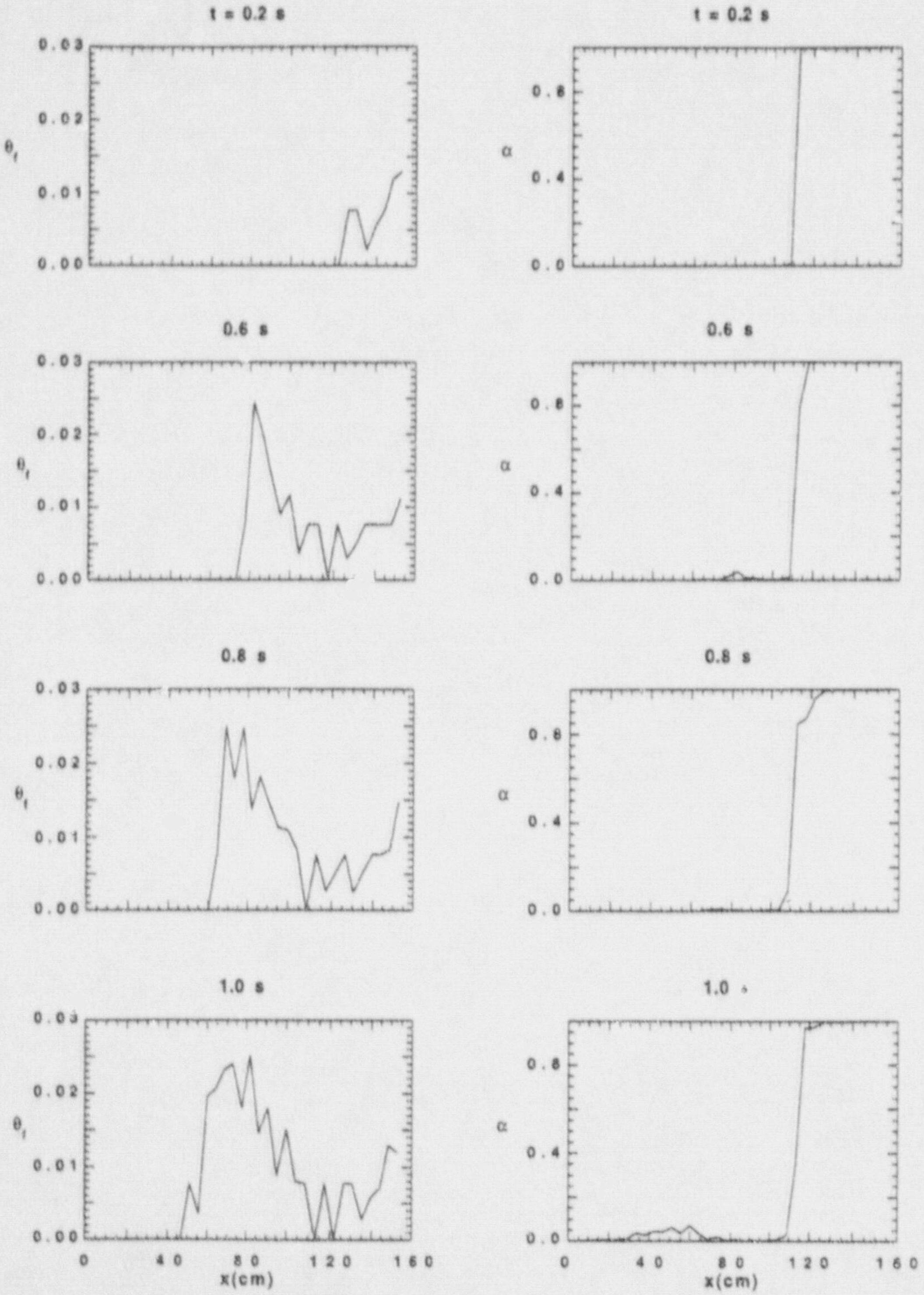

Figure 4. The predicted area-average fuel volume fraction and steam void fraction transients in K38.

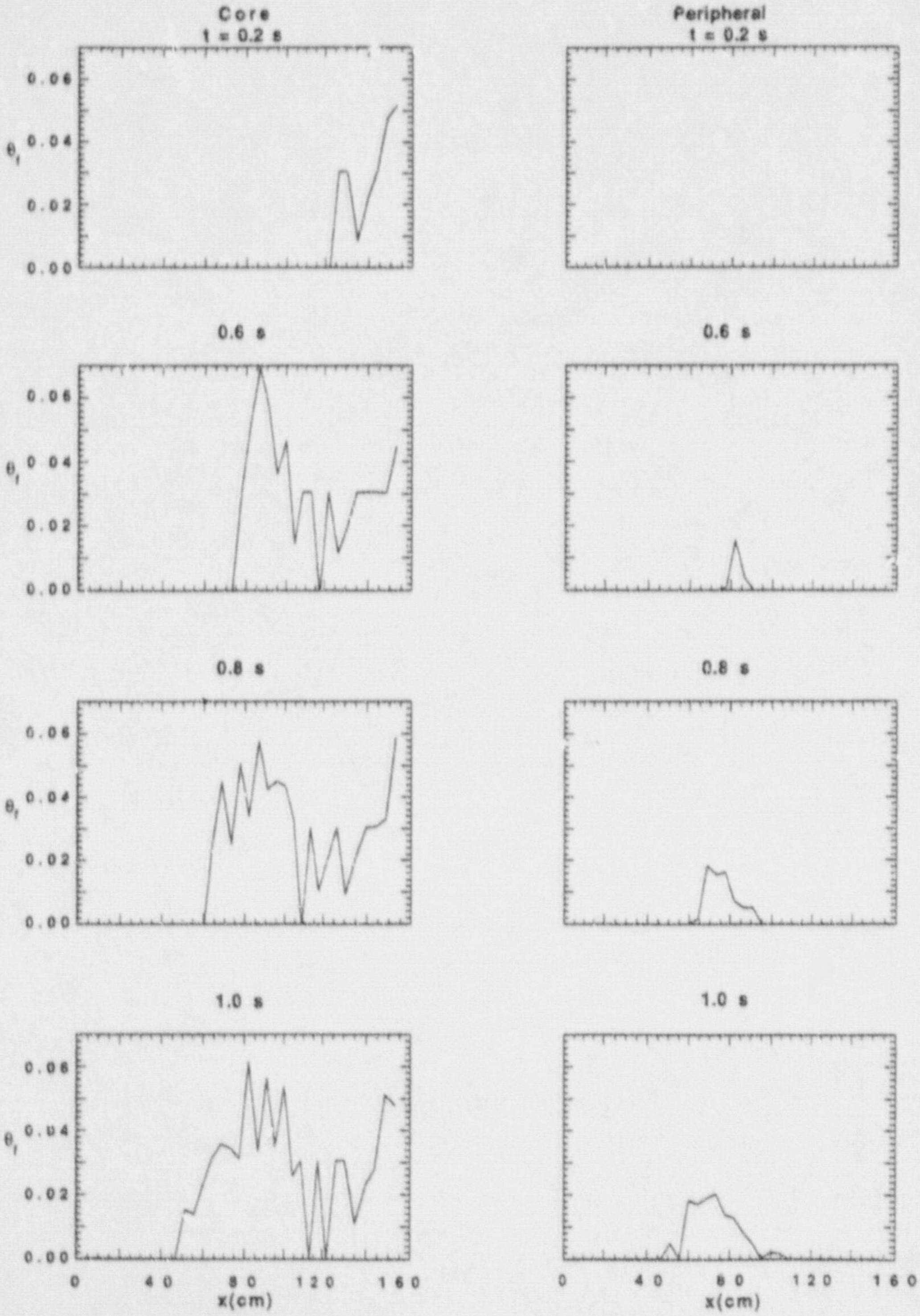

Figure 5. The predicted fuel volume fraction transients in the core (inner 4 cells) and the peripheral (outer 12 cells) areas.

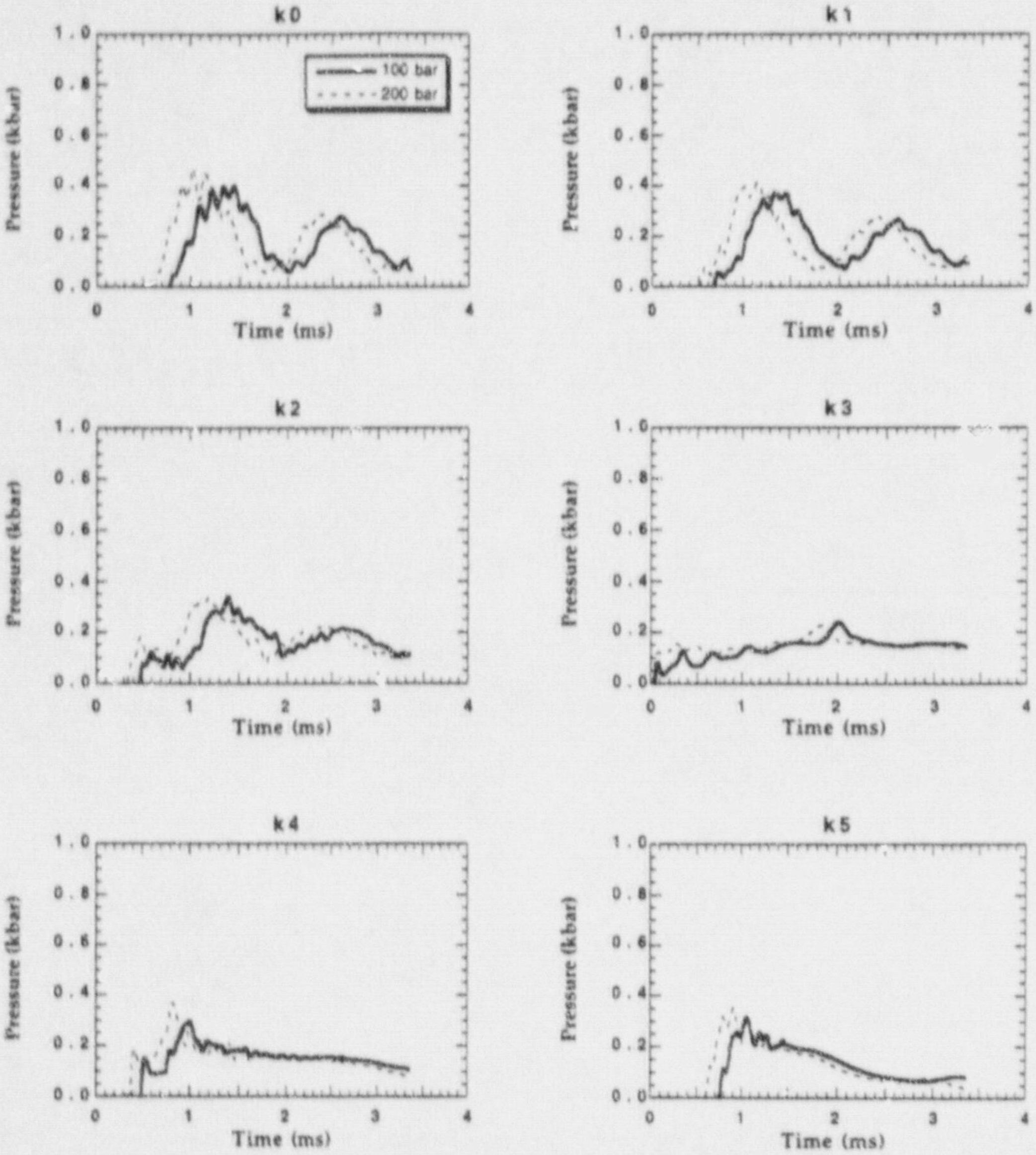

Figure 6. The effect of trigger pressure on the resulting explosion.

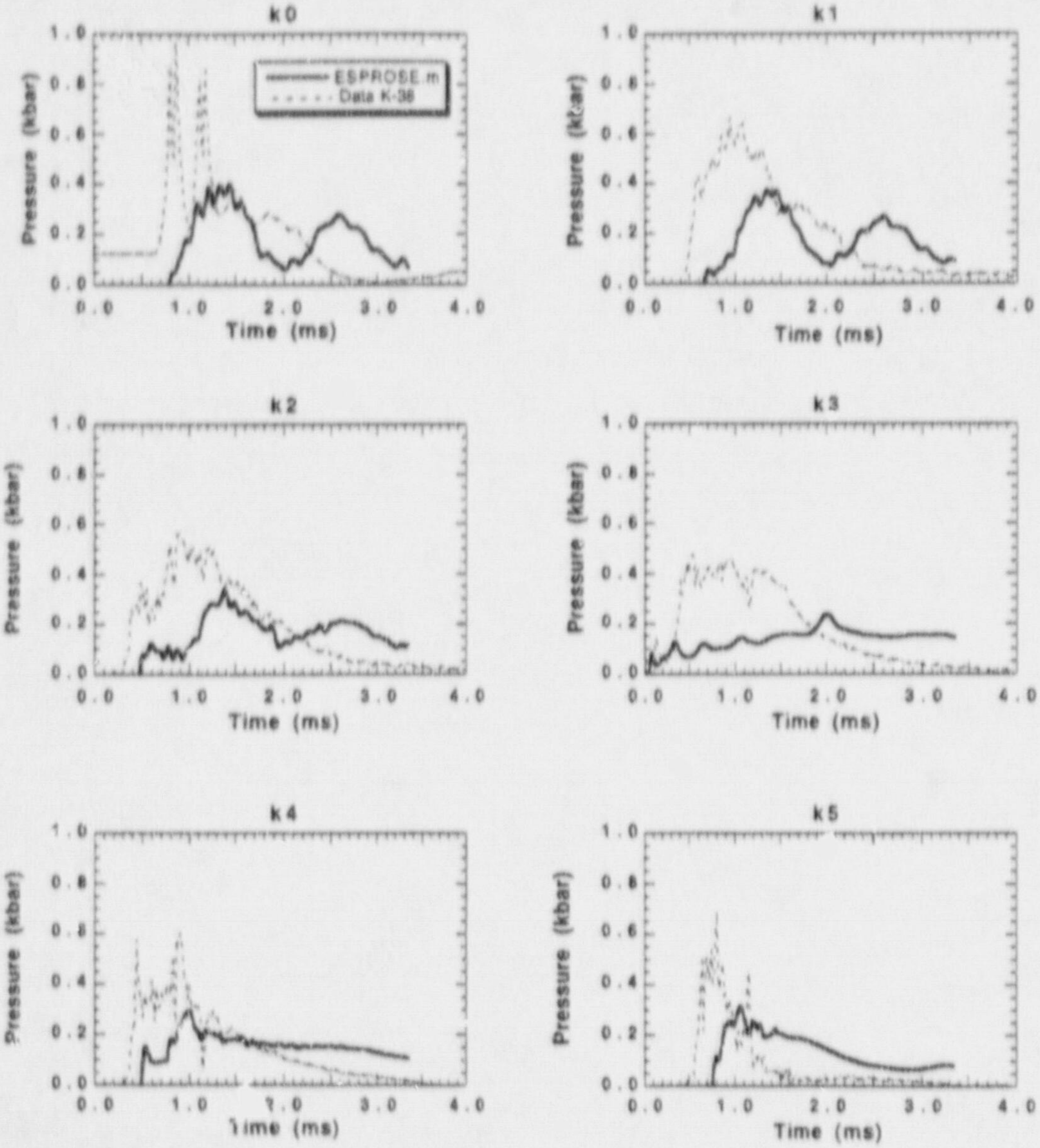

Figure 7. The explosion predicted by ESPROSE.m-3D against the data of K38. The entrainment factor, f_e, is set to 7.

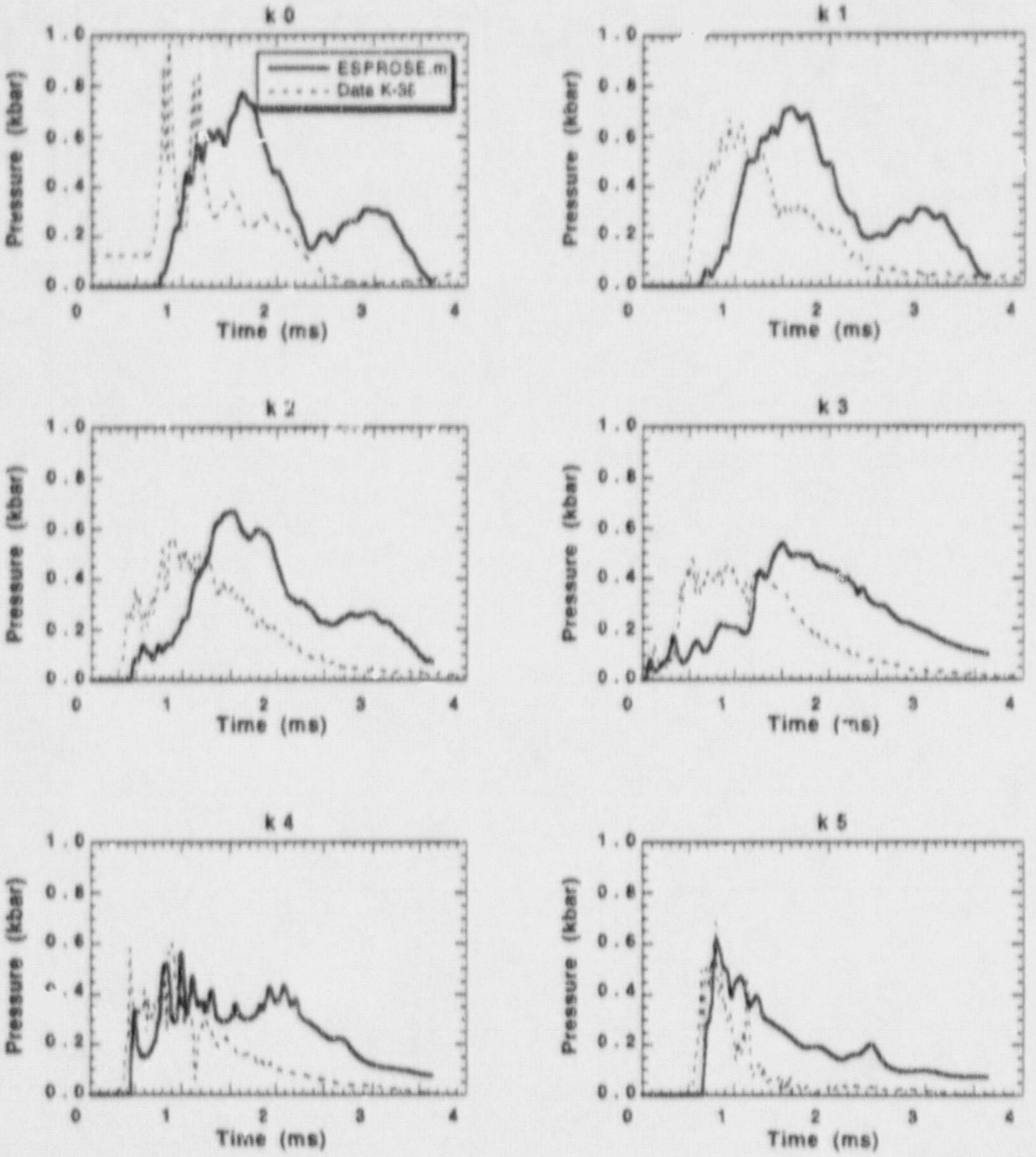

Figure 8. The explosion predicted by ESPROSE.m-3D against the data of K38. The entrainment factor, f_e, is set to 5.